Wissenschaftliche Berichte des Instituts für
Meteorologie und Klimaforschung der
Universität Karlsruhe (TH)

44

Jörg Rings

Monitoring the water content evolution of dikes

universitätsverlag karlsruhe

Jörg Rings

Monitoring the water content evolution of dikes

Wissenschaftliche Berichte des Instituts für Meteorologie und Klimaforschung der Universität Karlsruhe (TH)
Band 44

Herausgeber: Prof. Dr. Ch. Kottmeier

Institut für Meteorologie und Klimaforschung der Universität Karlsruhe (TH) (gemeinsam betrieben mit dem Forschungszentrum Karlsruhe)
Kaiserstr. 12, 76128 Karlsruhe

Monitoring the water content evolution of dikes

by
Jörg Rings

universitätsverlag karlsruhe

Dissertation, Universität Karlsruhe (TH), Fakultät für Physik
Tag der mündlichen Prüfung: 01.02.2008

Impressum

Universitätsverlag Karlsruhe
c/o Universitätsbibliothek
Straße am Forum 2
D-76131 Karlsruhe
www.uvka.de

Universitätsverlag Karlsruhe 2009
Print on Demand

ISSN: 0179-5619
ISBN: 978-3-86644-321-1

Monitoring the water content evolution of dikes

Überwachung der Wassergehaltsentwicklung in Deichen

Zur Erlangung des akademischen Grades eines
DOKTORS DER NATURWISSENSCHAFTEN
der Fakultät für Physik der Universität (TH)
Karlsruhe

genehmigte

DISSERTATION

von

Diplom-Physiker Jörg Rings
aus Prüm

Tag der mündlichen Prüfung 01.02.2008

Referent Prof. Dr. Christoph Kottmeier

Korreferent Prof. Dr. Kurt Roth

Abstract

A new combination of methods is applied to monitor the water content evolution of soils which is of interest in a broad range of applications, including the energy balance over land surfaces and the stability of flood-protection dikes. The water content in model dikes is quantified using electrical resistivity tomography (ERT), and numerical simulations of water flow are used to predict its evolution.

The viability of ERT to quantify water content change is shown in experiments on three model dikes. In conjunction with an initial water content estimate, ERT is shown to be applicable for monitoring soil water content. During a flooding experiment on a full-scale dike model, ERT successfully quantifies the water content of 34%. The inversion process that transfers measured data into models of subsurface resistivity can be disturbed by inversion artifacts if spatial contrasts in resistivity are present. Modeling of synthetic data can help identify artifacts and the modification of inversion regularization can diminish artifacts. Different geophysical methods are compared for data from a dike model and two other sites to account for the variability of bulk soil properties and water content. The homogeneous structure of the dike site allows measurements taken at different locations and with different methods to be directly comparable. Water content measurements taken with ERT show very good agreement with other methods. The second site shows sufficient homogeneity to compare pointlike measurements to one- or two-dimensional profiles. The third site is identified as highly heterogeneous, and measurements taken with point probes are unable to capture the lateral variability in water content.

Numerical simulation of water flow in the subsurface is able to predict water content evolution, but is unlikely to be able to quantify it correctly, as the complex natural processes are not captured by the simulation. The trends in water content evolution are modeled for the dike experiment, and the natural variability in water content is simulated for a 5-year period. Using data from meteorological forecast models, the trends in water content can be predicted, but quantification is highly dependent on the precipitation forecast.

The quality of ERT for quantifying resistivities is analyzed for the complete framework of hydrological modeling and simulated ERT surveys. The influence of varying resistivity contrasts is evaluated. It is shown that strong contrasts often result in large errors in resistivity quantification. To improve interpretation of ERT surveys, an ensemble and clustering approach that represents the possible range of inversion models is introduced. In this approach, 50 different, randomly determined models are compared. The method is successfully applied for two synthetic data sets. The interpretation of the inversion models is improved with respect to the analysis of the influence of spatial resistivity contrast and the identification of inversion artifacts.

Erweiterte Zusammenfassung

In dieser Arbeit werden die Elektrische Widerstandstomographie (Electrical Resistivity Tomography, ERT) und weitere geophysikalischer Methoden, angewandt um den Wassergehalt von Hochwasserschutzdeichen zu überwachen und kombiniert mit numerischen Simulationen der Wasserbewegung im Boden. Um eine räumliche und zeitliche Beschreibung des Wassergehaltes zu erreichen, ist es erforderlich a) die Fähigkeit von ERT zur Quantifizierung von Wassergehalt zu ermitteln, b) die Eignung numerischer Simulationen als Werkzeug zur Vorhersage der zeitlichen Wassergehaltsentwicklung zu zeigen, c) eine Beschreibung der Verlässlichkeit geophysikalischer Messmethoden zur Überwachung von Bodenfeuchte unter Berücksichtigung der vorherrschenden Heterogenitäten in den Bodenparametern vorzunehmen und d) Modellierung und Messmethoden zur Bewertung der einzelnen Methoden zu kombinieren.

Erste Experimente mit ERT werden auf großmaßstäblichen Labordeichen durchgeführt. Die Ergebnisse zeigen die prinzipielle Eignung von ERT zur Überwachung von Wassergehalten, aber die engen Dimensionen des Deiches und weitere Einbauten beeinflussen die Messungen. Auf einem naturmaßstäblichen Deichmodell an der Bundesanstalt für Wasserbau in Karlsruhe werden die Hauptexperimente dieser Arbeit durchgeführt. Dort steht, wie auf den Labordeichen, Time Domain Reflectometry (TDR) als Vergleichs- und Kalibriermethode zur Verfügung. Wassergehaltsänderungen können durch Beregnung und Einstau induziert werden. Es kann gezeigt werden, dass ERT sich als Hauptmethode zur Überwachung eignet, wenn es in Verbindung mit einer anderen Methode angewandt wird, die einen initialen Wassergehalt bestimmt. Eine petrophysikalische Relation legt den Zusammenhang zwischen elektrischem Widerstand und Wassergehaltsänderung fest. Die Ergebnisse zeigen gute Quantifizierungen von Wassergehalten. Bei einem Einstauversuch kann der Wassergehalt von 34% im gesättigten Bereich mit ERT korrekt quantifiziert werden. Die Ergebnisse können allerdings durch Inversionsartefakte gestört werden. Es kann anhand von Modellierungen mit synthetischen Daten gezeigt werden, dass diese Artefakte durch räumliche Widerstandskontraste hervorgerufen werden können. Die guten Ergebnisse vom Deichmodell hängen von der gültigen Annahme einer homogenen Deichstruktur ab.

Ein Vergleich zu weiteren geophysikalischen Methoden in Verbindung mit einem

Übergang zu stärker heterogenen Messorten wird durch die Einbindung von Messdaten, die von anderen Messkampagnen im Schwarzwald und in Burkina-Faso gewonnen worden waren, hergestellt. Die eingesetzten Methoden umfassen ERT, Bodenradar (GPR), TDR und Frequency Domain Reflectometry (FDR). Wenn das untersuchte Gebiet ausreichend homogen ist, können Punktsensoren wie TDR und FDR repräsentative Werte für das Messgebiet bestimmen. Besonders Wassergehaltsänderungen werden gut erfasst. Wenn eine genauere Beschreibung der Wassergehaltsverteilung benötigt wird, wie es z.B. bei Hochwasserschutzdeichen der Fall ist, ist der Einsatz einer zwei- oder dreidimensional auflösenden Methode wie ERT erforderlich. Liegt eine höhere Heterogeneität der Bodenparameter im Messgebiet vor, wie es z.B. in Burkina-Faso der Fall ist, aber der Wassergehalt auf größeren Skalen bestimmt werden soll, wie es z.B. für die Einbindung in meteorologische Vorhersagemodelle notwendig ist, ist eine Verbindung von Punktmessungen mit räumlichen Verteilungen nicht trivial. Ein optimaler Beobachtungsansatz sollte auf wiederholten Messungen basieren, die z.B. mit ERT oder GPR durchgeführt werden.
ERT hat das Potential, als hauptsächliche, permanent installierbare und automatisierbare Methode zur Überwachung von Deichen eingesetzt zu werden. Zur Kontrolle der Sicherheit von Deichen ist neben Messungen eine Vorhersage der Wassergehaltsentwicklung notwendig. Die Vorhersagbarkeit von Wassergehalten wird überprüft, indem die Wasserbewegung im Boden in einem numerischen Modell simuliert wird. So können die zu erwartenden Änderungen im Wassergehalt abgeschätzt werden. Die Quantifizierung der Änderungen ist jedoch nicht ausreichend genau, weil das Modell die Bodenwasserbewegung im sogenannten Richards-Regime simuliert, wo eine zusammenhängende Luftphase vorausgesetzt wird. Diese Bedingung ist für die Einstau- und Beregnungsversuche am Deichmodell nicht erfüllt. Eine komplexere Beschreibung unter Berücksichtigung von Mehrphasenbewegung, die die Bedingungen nahe Sättigung immer noch nicht beschreiben würde, benötigt aber in dieser Studie oder den meisten Anwendungen nicht mögliche Messungen der Luftphase. Eine Langzeitsimulation basierend auf 5 Jahren Niederschlags- und Evapotranspirationsdaten kann die zeitliche Variabilität des Deiches unter natürlichen Bedingungen bestimmen und erlaubt eine Abschätzung der zeitlichen Autokorrelation von Wassergehalten.
Die Vorhersage von Wassergehalten wird weiterhin für prognostizierte Nieder-

schlags- und Verdunstungsreihen vor zwei ausgesuchten Niederschlagsereignissen während der COPS-Messkampagne (Wulfmeyer et al., 2008) untersucht. Die Ergebnisse zeigen, dass Vorhersagemodelle, die unterschiedlich lang vor dem Niederschlagsereignis gestartet werden, zwar das Einsetzen des Niederschlages meist korrekt abschätzen kann, die genaue Menge aber oft stark unterschätzt wird.

Als Konsequenz der Messungen mit ERT und der numerischen Simulation ergibt sich die Notwendigkeit, die Verlässlichkeit von ERT zur Quantifizierung von Widerständen (und somit Wassergehalten) in einem integrierenden Ansatz zu untersuchen. Dieser Ansatz hat den Vorteil, dass er a) synthetische Datensätze modelliert, die aber möglichst nahe an natürlich möglichen liegen und b) dazu nicht jede Methode separat betrachtet wird, sondern vielmehr die Kombination der Methoden. Die vorgeschlagene Methode umfasst zwei Ansätze zur Auswertung und Verbesserung von Widerstandsmessungen, die alle Verarbeitungsschritte des Messens und der Inversion von Widerständen, der Umrechnung in Wassergehalte, aber auch der Simulation der Wasserbewegung umfassen. Diese Methode wurde auf zwei synthetische Datensätze angewendet. Die Ergebnisse zeigen, dass Widerstände oft nur mit großen Fehlern bestimmt werden können, die von der mit der Tiefe abnehmenden Sensitivität und dem Vorhandensein von Widerstandskontrasten beeinflusst werden. Eine Folgerung daraus ist, dass selbst ein bezüglich der jeweiligen Inversion optimales Modell nicht genau genug sein kann um die Wirklichkeit angemessen zu beschreiben. Deshalb wird ein Ensembleansatz vorgeschlagen, in dem zufällig 50 verschiedene Varianten des Inversionsmodell bestimmt werden und mit einer Clustermethode gruppiert werden. Das gemittelte Modell aller Mitglieder eines Cluster kann repräsentativ ausgewertet werden. Der Ensembleansatz erlaubt eine bessere Interpretation von Inversionsmodellen und kann für die synthetischen Datensätzen erfolgreich zur Identifikation von Inversionsartefakten eingesetzt werden.

Contents

1 Introduction

The physical properties of soil, vegetation and air as well as the close coupling between soil physical and meteorological processes define the microclimate and the energy budget over land surfaces. Soil, with its ability to store water, serves as a 'memory' for precipitation, evaporation and energy exchange of previous days. A determination of the water balance of the soil layer and its description with numerical models is key to an understanding of the relevant processes.

The task of determining the water balance is comparably simple for homogeneous, flat surfaces. In this project, the water balance of two-dimensional structures, i.e. flood-protection dikes, will be studied. The rationale behind this approach is based on observational evidence that the protection effect in the event of a flood is particularly influenced by the initial water content and the percolation of water.

The aim of this thesis is to quantitatively describe the water content of a dike body considering flood protection, taking into account the time dependent influences of flooding, precipitation and evapotranspiration. To this end, detailed measurements and numerical simulation are carried out to obtain a physically consistent description of the processes involved.

Results of this study are applicable to flood-protection dikes, but also apply to near-surface soil water content in general. Meteorological conditions, e.g. the ability to forecast small-scale convective precipitation events, hydrological modeling in the saturated and unsaturated zone, e.g. to forecast flood events, agricultural and geological processes all depend on knowledge of the water flow in the shallow subsurface. As such, the use of geophysical methods in hydrological studies has emerged as a new branch commonly called hydrogeophysics. If the near surface of field sites is explored by established or new methods, considerable gain is possible in terms of measurement speed, effort needed and most importantly much larger sample volumes compared to traditional geological and hydrological methods. Additionally, the combination of approaches may improve the quality of each single method. However, the need for further research is also apparent. For example, established methods need to be transferred to near surface applications, for developing new methods and for establishing the link between measured properties and water content.

1.1 Flood-Protection Dikes

Dikes are structures built of soil materials with the aim of preventing a flooding of land behind the dike in the event of a flood on a sea or a river. A stable dike has to reduce the water potential of the dammed water to zero.

Three mechanisms are the most important causes for dike failures during a flood (Scheuermann, 2005):

- If the water level rises above the dike crest, water flowing over the dike will cause erosion, which leads to a breach in the dike crest.
- The rising water level can lead to a rise of the groundwater level under the dike base, ultimately causing a base failure, with increased seepage through the dike base. This leads to deformation processes in the underground that cause a sinking of the dike.
- During each flood, water will infiltrate through the dike. In the case of deep infiltration, water can exit at the land side and gradually take away material, leading to slope failure and ultimately, to dike breaches.

The total length of river dikes in Germany is 10400 km (Müller, 1999). Most of these dikes have already been built around the beginning of the 20th century. Unfortunately, the exact composition of their inner structure is often unknown. It has to be assumed that they have been built up homogeneously or with unplanned zonings.

A dike constructed by modern technical standards will contain constructional elements that will lead to a complete reduction of the flood water potential. For existing old river dikes, especially if they are of homogeneous structure, the water potential will possibly not be completely reduced, and water can exit at the land-side slopes, leading to the third damaging factor described above. In the event of a flood, a water saturated area in the dike will be established which is delimited by the *phreatic line*, a theoretically derived line (see e.g. Uginchus, 1960; Polubarinova-Kochina, 1962).

Scheuermann (2005) described a method to determine the instationary percolation of water in a dike. The water content within the dike body before the flood is a critical parameter determining the speed with which flood water will percolate through the dike. For this reason, the monitoring of dike water content is an important tool in dike safety management.

On dams and dikes, geoelectrical surveys have been established for safety management (Sjoedahl et al., 2004) or for the detection of heterogeneities and possible causes for instabilities such as termite nests (Weller et al., 2006). The effects of dam and dike geometry have been studied and methods to reduce the effects of the topography have been explored (Hennig et al., 2005; Sjoedahl et al., 2006).

Hydrogeophysical methods can be applied for two aspects of monitoring purposes: The water content can be determined, so that in the event of a flood, dike safety can be estimated. To this end, the inclusion of meteorological forecasts to determine the future development of the water content is of great importance. Secondly, in the event of a flood, the hydrological process of water percolation can be monitored by geophysical methods, thus supporting decisions in safety management.

1.2 Importance of Soil Water Content for Meteorological Processes

The availability and distribution of water vapor in the atmosphere is one of the most important factors determining precipitation initiation. Convective precipitation depends on two conditions. If sufficient vertical motion is present to transport moisture upwards, the availability of moisture determines the development of convective precipitation. Moisture can become available by (a) advection through large-scale or mesoscale processes or (b) processes connected to the energy balance of the surface.

The latter processes are influenced by soil moisture and its spatial variability (Sogalla et al., 2005; Ament and Simmer, 2006) through evapotranspiration from soil or vegetation (Desai et al., 2006). In addition, soil moisture influences the energy balance in the planetary boundary layer via albedo and emissivity of the Earth's surface and by limiting the daily temperature range (Dai et al., 1999).

Spatial variability of soil moisture can trigger convection (Schaedler, 1990; Baker et al., 2001), both on the local scale and on the mesoscale (Cheng and Cotton, 2004). Soil moisture is one of the least studied properties in connection with convective system development, so an improved representation of soil moisture fields in weather forecast models is likely to produce better agreement between modeled and measured surface energy fluxes and precipitation (Seuffert et al., 2002). Sensitivity analyses using a combined model for weather forecast and soil atmospheric transfer (VEG3D, Braun and Schaedler, 2005) showed a non-trivial relationship between initial soil water content and the initiation of convection, both concerning timing and area of convection as well as the timing and extent of the corresponding precipitation fields (Meissner et al., 2007).

With very few exceptions, no operational soil moisture observation networks are available. Some exceptions exist on a scale too coarse for mesoscale studies (Robock et al., 2000) or of unknown accuracy (Kerr et al., 2001). Other than remoting sensing (e.g. Kerr, 2007), in-situ soil moisture networks exist only in a few regions (Schneider et al., 2003). On the local scale, operational soil moisture networks are used in agricultural applications and in hydrology for capturing runoff characteristics, for example for improved flood warning. These networks are neither connected nor compiled into a common monitoring data base (Bogena et al., 2005). The recently initiated operational soil moisture network SOMONET (Krauss et al., 2007) will provide regionalized soil moisture profiles in connection with the Convective Preciptation Study (COPS, Wulfmeyer et al., 2008).

The difficulties in assessing soil moisture fields stem from the large heterogeneity of soil concerning type, surface characteristics, land use, vegetation and orography (Teuling and Troch, 2005). The recent developments in the field of hydrogeophysics provide valuable tools concerning the investigation of soil moisture and its variability, which is important e.g. for the upscaling of soil properties. The methods studied in this thesis may not only be applied to the monitoring of dikes, but can generally be used for a variety of applications e.g. for observation of soil moisture for meteorological applications.

1.3 Objectives

The first objective is to evaluate a geophysical method for the quantification of water content. This method has to be able to quickly and mostly non-invasively determine soil water content, but should also be amenable for automatical monitoring purposes. The method of electrical resistivity tomography (ERT) is evaluated for this purpose. The results from a full-scale dike model are presented in chapter 3. The first preliminary experiments on two laboratory dikes and additional measurements from the full-scale dike model are described in appendix A.

Secondly, geophysical methods measuring soil water content are evaluated and compared for more heterogeneous sites. In this study, four different geophysical methods are applied on three sites of different heterogeneity. The spatial and temporal variability of soil properties with respect to the scale of interest is evaluated, and the viability of the measurement techniques to capture spatial water content distributions is discussed with respect to this variability (Chapter 4).

The third objective aims to assess if using data from meteorological forecast models is able to predict water content evolution. Several numerical experiments are conducted that comprise studies of the soil parameters, the initial and boundary conditions, a simulation of the model dike experiment and of long-term precipitation and evapotranspiration data. Two rainfall events are studied within a large experimental operation. The results are evaluated in chapter 5.

Finally, ERT is evaluated as a stand-alone method for quantifying resistivity. As a consequence of the previous studies, this analysis is based on an integrated approach that includes modeling of ERT measurements, the ERT inversion process and hydrological modeling for two synthetic case studies. This approach allows cross-validation of the methods. Based on the results, the realibity of ERT in the presence of changing resistivity contrasts and varying sensitivity is evaluated. An ensemble and clustering approach is introduced to improve the interpretation of ERT surveys. The results are discussed in chapter 6.

2 Theory and Methods

This chapter shortly introduces concepts and methods used in this study. This encompasses the energy balance at the soil-atmosphere interface; the geophysical methods used, especially ERT and time domain reflectometry (TDR), and a synopsis of the relevant soil physical processes that provide the basis for numerical simulation of water movement in soil.

2.1 Energy Balance

Besides rainfall, evapotranspiration influences the change of soil water content at the soil-atmosphere interface. Different methods exist to measure or determine the evapotranspiration (see e.g. Burman and Pochop, 1994). In this study, the potential evapotranspiration is obtained from the balance between incoming and outgoing radiation.

The emission of radiation by electromagnetic waves is a property of any natural body. The perfect radiator or *black body* emits the maximal possible radiation at a given temperature. The maximum flux of radiation R is given by the *Stefan-Boltzmann law*

$$R = \sigma T^4 \tag{2.1}$$

where $\sigma = 5.67\, Wm^{-2}K^{-4}$ is the Stefan-Boltzmann constant and T the absolute temperature of the black body's surface. The wavelength (in μm) corresponding to the maximum spectral radiant energy is given by *Wien's law* as a function of temperature T (in K):

$$\lambda_{max} = \frac{2897}{T} \tag{2.2}$$

The spectrum of solar radiation is well approximated by that of a black body radiator with surface temperature $T_S \approx 6000\ K$. In the absence of absorbing substances like water vapor, the spectrum of radiation emitted by the surface of the Earth can be approximated by black body radiation with $T_E = 287\ K$. In the atmosphere, there is little overlap between the spectra of sun and terrestrial radiation, with $\lambda_{max,S} \approx 0.48\ \mu m$ and $\lambda_{max,E} \approx 10.1\ \mu m$ following (2.2). The range of wavelenghts of the terrestrial radiation is thus referred to as *longwave*, the solar spectrum as *shortwave* radiation.

Under the assumption of an infinitely thin soil-atmosphere interface having no heat capacity, the energy balance at the surface can be characterized as

$$Q_0 = H_0 + E_0 + B_0 \tag{2.3}$$

where H_0 is the sensible heat flux, E_0 is the latent heat flux, B_0 is the ground heat flux from the surface. Q_0 is the net radiation expressed as

$$Q_0 = (S_{in} - S_{out}) + (L_{in} - L_{out}) \tag{2.4}$$

where S and L refer to shortwave and longwave radiation, respectively, and the indices *in* and *out* characterize incoming and outgoing radiation. The sign convention is that fluxes directed towards the interface have a positive sign.

The energy balance equation (2.3) can be reformulated in terms of the Bowen ratio $\beta = H_0/E_0$. Using the theory of eddy correlation (e.g. Arya, 2001), assuming the eddy exchange coefficients K_h and K_w are equal, one can show that

$$\beta = \frac{c_p}{L}\frac{\partial T/\partial z}{\partial q/\partial z} \approx \frac{c_p}{L}\frac{\Delta T}{\Delta q} \tag{2.5}$$

with specific humidity q, the specific heat at constant pressure c_p and the latent heat of evaporation L. By measuring T and q in two different heights, the partial differences can thus be approximated by $\Delta T/\Delta q$. Through measururement of ground heat flux B_0, e.g. with heat flux plates, and net radiation Q_0 following (2.4), the latent heat flux E_0 is obtained as

$$E_0 = \frac{Q_0 - B_0}{1 + \beta} \tag{2.6}$$

and finally the evapotranspiration $V = E_0/L$.

Penman formulation

If no temperature and specific humidity data at different heights are available, potential evapotranspiration rates can also be estimated using e.g. the Penman equation (Batchelor, 1984). Here, a modification of the Penman-equation (Doorenbos and Pruitt, 1977) is applied that is calibrated for grass surfaces.

$$V_i = \frac{g_i}{g_i + \gamma_i}(R_{ni}) + L_i \frac{\gamma_i}{g_i + \gamma_i}(e_{ai} - e_{di})F(u_i) \tag{2.7}$$

with

- V_i: Potential evapotranspiration per hour at time i
- g_i: Slope of saturated vapor pressure vs temperature relationship $[kPa/°C]$
- γ_i: Psychrometer coefficient $[kPa/°C]$
- R_{ni}: Net radiation $[W/m^2]$
- L_i: Latent heat of evaporation for water $[J/kg]$
- e_{di}: Actual vapor pressure $[kPa]$
- $F(u_i)$: Wind-related function $[mm/(kPa\,h)]$

The exact method including the wind-related function is explained e.g. by Burman and Pochop (1994).

2.2 Hydrogeophysical Methods

Hydrogeophysics is a rather new discipline (Rubin and Hubbard, 2005) that has emerged from the use of geophysical methods in hydrological and hydrogeological applications. These applications are threefold: Mapping of hydrogeological features, hydrological parameter estimation and the monitoring of hydrological processes.

The mapping issue includes the detection of geological features, but also finding the water table or the extent of fluid plumes. It has important applications e.g. in aquifer detection (see e.g. Barker and Moore, 1998; Suzuki and Higashi, 2001; Sandberg et al., 2002; Bristow and Jol, 2004; Bridge and Hyndman, 2004; Day-Lewis et al., 2004; Nguyen et al., 2007).

A second field is the retrieval of hydrological properties, namely the water content of the subsurface. Other applications may lead to estimates of hydraulic conductivity or the spatial correlation of hydrogeological parameters (e.g. Roth et al., 1990; Dannowski and Yaramanci, 1999; Hubbard et al., 1999; Binley et al., 2002b,a; Garambois et al., 2002; Huisman et al., 2003; Cassiani et al., 2004; Wollschlaeger and Roth, 2005; Turesson, 2006; Weihermueller et al., 2007; Preko, 2008).

Thirdly, the monitoring of hydrological processes, mainly the movement of water or other fluids in the subsurface over time, is an application where the low-intrusive observation with geophysical methods is of great interest (e.g. Daily and Ramirez, 1992; Binley et al., 1996; Slater et al., 2000; Trinks et al., 2001; French et al., 2002; LaBrecque et al., 2004; Cassiani and Binley, 2005; Vanderborght et al., 2005; Singha et al., 2007).

Hydrogeophysics poses challenges in different directions:

The most important challenge is developing new geophysical methods and assessing the viability of existing methods in a hydrogeophysical context. Many geophysical methods have a long standing tradition in the oil industry for the detection of reservoirs. However, these applications deal with different subsurface properties, with consolidated rock material, with high temperature and pressure environments. Application in near surface geophysics needs to detect much more subtle changes and thus new challenges for established methods emerged (Rubin and Hubbard, 2005). Depending on the application, a different scale can be of interest. While soil properties are usually determined on a laboratory scale or even on a pore scale, hydrogeophysical measurements mostly operate on the field scale of few to several hundred meters. In meteorological applications, a regional scale of several kilometers or even a meso scale of up to several hundred kilometers might be of interest. Soil properties usually are heterogeneous across many scales (Nielsen et al., 1973; Vogel and Roth, 2003), and the transition between the scales is non-trivial and an important research topic (Bloeschl and Sivapalan, 1995; Vereecken et al., 2007).

Geophysical methods have different measurement volumes. Usually, one data point equals an effective mean value of this sensitivity volume. While pointlike methods like time domain reflectometry (TDR) have small sensitivity volumes of a few centimeters around the probe, the model block in an electrical resistivity tomography survey might represent a much larger volume up to depths of tens of meters. So, as high resolution data over large extents are rarely available, one of the main problems in hydrogeophysics is the fusion of data obtained from different methods into one coherent picture of the subsurface. One method is the use of statistical methods, like geostatistics (e.g. Isaaks, 1990; Carle et al., 1999). The data to be fused may not only include geophysical measurements of varying sensitivity, but also constraints like hydrological/meteorological boundary conditions (e.g. water mass balance) or geological input (e.g. depth to bedrock, known lithology or layering from borehole data) (e.g. de la Vega et al., 2003; LaBrecque et al., 2003; Cassiani and Binley, 2005; Kowalsky et al., 2005; Lambot et al., 2006; Linde et al., 2006; Athanasiou et al., 2007).

2.2.1 Petrophysical Relations

Hydrogeophysical surveys for determination of spatial properties are usually applied either from the surface or in (cross-)borehole applications. In-situ installed probes, i.e. in TDR, can provide measurements that are pointlike with respect to a field scale survey. A field scale application may measure a transect of several meters up to a few kilometers. The properties in question, in the following especially the water content, have to be obtained from the measured data.

No method can directly retrieve the water content. Instead, they measure soil properties that change with water saturation. These properties include the dielectrical permittivity and the electrical resistivity. Liquid water has a dielectric permittivity ε of 80 (Davis and Annan, 1989). Electrical conductivity depends on the solute content. Pure water has a low conductivity of $4 \cdot 10^{-6}$ S/m, natural waters have a conductivity ranging from 0.01 S/m for freshwater up to 20 S/m for oil field brines (Rubin and Hubbard, 2005).

The equations transferring the geophysical properties into water content values are called petrophysical relations. These may be deducted for a given site by a calibration function, but there are also widely established calibration functions, like the equation given by Archie (1942) for bulk electrical conductivity.

If the parameters defining these relationships are determined in the laboratory, the transfer to the field-scale is not trivial, as the field scale may be governed by heterogeneities. For the model dikes in this study however, it was possible to assume homogeneity.

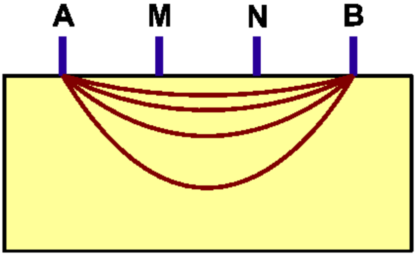

Figure 2.1: *Basic principle of geoelectric surveys: A current is injected on two electrodes AB while the potential difference is measured for MN.*

2.3 Geoelectrical Methods

2.3.1 Principles

While TDR and ground-penetrating radar (GPR) aim to retrieve the relative dielectrical permittivity ε_r of the subsurface, geoelectrical methods focus on the electrical conductivity σ or its inverse, the resistivity ρ.

Geoelectrical methods are based on the idea of injecting a current into the subsurface via two electrodes, and measuring the potential difference between two other electrodes (Fig. 2.1). Given a point source of current I_p at position $\mathbf{x_p}$, an integral over the current density $\mathbf{j}$ evaluated on the surface ∂V of any volume V containing the source must equal the current:

$$\oiint_{\partial V} \mathbf{j} \cdot d\mathbf{f} = I_p \leftrightarrow \nabla \cdot \mathbf{j} = I_p \delta(\mathbf{x_p}) \tag{2.8}$$

where $\delta(\mathbf{x_p})$ is a Dirac Delta function and the Gaussian Theorem has been used to evaluate the surface integral.

In combination with Ohm's law $\mathbf{j} = \sigma \mathbf{E}$ for electrical conductivity σ and electrical field $\mathbf{E}$, a Poisson equation can be obtained from the electrical potential field Ψ that is defined by $\mathbf{E} = -\nabla\Psi$ as

$$\nabla\sigma \cdot \nabla\Psi + \sigma\triangle\Psi = -I_p\delta(\mathbf{x_p}) \tag{2.9}$$

If we assume a homogeneous half-space and a point-size electrode placed on the surface at coordinates (0,0,0), the first term in the above equation will vanish and the electrical potential field will be

$$\Psi = \frac{\rho_a I_p}{2\pi}\frac{1}{x} \tag{2.10}$$

where x is the distance from the source and $\rho = 1/\sigma$ is the resistivity. ρ_a is called the apparent resistivity that is equal to the true resistivity of the subsurface for a homogeneous half-space. The boundary conditions hereby are $\Psi \rightarrow 0$ for $x \rightarrow \infty$ and $\Psi \rightarrow \infty$ for $x \rightarrow 0$. The potential difference $U_{M,N}$ between M and N (see Fig. 2.1) for a current injected through electrodes A and B can be calculated by superimposing the fields for the currents at the potential electrode positions:

$$U_{M,N} = \frac{\rho_a I_p}{2\pi}\left(\frac{1}{\overline{\overline{MN}}} - \frac{1}{\overline{\overline{BM}}} - \frac{1}{\overline{\overline{AN}}} + \frac{1}{\overline{\overline{BN}}}\right) = k\frac{\rho_a I_p}{2\pi}, \tag{2.11}$$

where e.g. $\overline{AN}$ is the distance between electrode A and N, and k is the so-called *geometrical factor* containing the information about the electrode setup.

2.3.2 Electrical Resistivity Tomography

Electrical resistivity tomography became available in the late 1980s and early 1990s with the rise of instruments for fast and automatic measurements of large numbers of electrode combinations (quadrupoles). This way, all possible quadrupoles along a given electrode array can be obtained. In this study, lines of 24 and 48 electrodes were used. Different geometries of the electrodes are possible. The two geometries used in this work are the Wenner-Schlumberger and the Dipole-Dipole array (Fig. 2.2).
The geometry factors for these arrays can be calculated from eq. (2.11) as:

Wenner-Schlumberger:

$$k_{WS} = \frac{2\pi}{1/na - 1/(a+na) - 1/(a+na) + 1/na} = \pi n(n+1)a \tag{2.12}$$

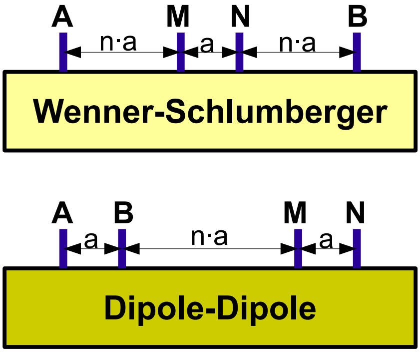

Figure 2.2: *Arrays used in ERT surveys in this study, with a denoting the electrode spacing, while n · a is a multiple of a.*

Dipole-Dipole:

$$k_{DD} = \frac{2\pi}{1/(a+na) - 1/(na) - 1/(2a+na) + 1/(a+na)} = \pi n(n+1)(n+2)a \tag{2.13}$$

where a is the electrode spacing and n is a multiplier ($n = 1,\ 2...$). For the Wenner-Schlumberger array (Fig. 2.2), n modifies the distance between the current and the potential electrodes while the distance between the potential electrodes stays constant. For the Dipole-Dipole array, the distance between both current electrodes and both potential electrodes stays constant, while the separation between these dipoles is modified by n. Compared to the Wenner-Schlumberger array, the Dipole-Dipole array has a better horizontal resolution, but takes a larger number of measurements.

As increasing water content in the pore space leads to decreasing resistivity of the soil, the ERT method is suitable to detect changes and movement of water. It has successfully been applied in borehole surveys of tracer experiments (Slater et al., 2000; Kemna et al., 2002) or in laboratory experiments using soil columns (Binley et al., 1996) or an experiment tank (Slater et al., 2002). It has also been applied in surface-based surveys of the vadose zone (Daily and Ramirez, 1992) or for groundwater flow after heavy rain (Suzuki and Higashi, 2001).

Improving the quality of ERT surveys has been an intense research topic, because choice of measurement configuration may have significant influence on the survey results. Dahlin and Zhou (2004) have compared 10 different electrode arrays for 2D surveys and assessed their quality using synthetic data sets. Stummer et al. (2004) have developed algorithms to calculate optimal electrode arrays that provide as much information on the subsurface as possible. The effects of measurement errors (Zhou and Dahlin, 2003; Oldenborger et al., 2005; Day-Lewis et al., 2005; Singha and Gorelick, 2006) and geometry (Loke, 2000; Hennig et al., 2005; Sjoedahl et al., 2006) on the surveys have been studied.

2.3.3 Inversion Theory

As the above discussion is based on the assumption of a homogeneous subsurface, for an arbitrary soil structure a numerical *inversion* scheme has to be applied. The aim of this inversion is the estimation of a resistivity model of the subsurface yielding a model response as close as possible to the measured *apparent resistivity* data. Historically, the availability of faster computer systems able to perform reliable inversions an additional and important contributing factor to the development of ERT. deGroot Hedlin and Constable (1990) formulated the objective function S to be minimized as

$$S(\Delta \mathbf{m}_i) = \Delta \mathbf{d}_i^T \Delta \mathbf{d}_i + \lambda_i \, \mathbf{m}_i^T \mathbf{W}^T \mathbf{W} \mathbf{m}_i \tag{2.14}$$

where i is the iteration number, $\Delta \mathbf{m}_i$ is the desired change in model parameters for iteration i, $\Delta \mathbf{d}_i$ is the discrepancy vector containing the differences between the logarithms of the measured and calculated data, λ_i is the regularization factor, $\mathbf{W}$ a roughness filter matrix, a first-order finite-difference operator (deGroot Hedlin and Constable, 1990) and $\mathbf{m}_i$ are the model parameters.

A widespread method for solving this smoothness-constrained objective function is the Gauss-Newton method that involves solving of the following system of equations:

$$(\mathbf{J}_i^T \mathbf{J}_i + \lambda_i \mathbf{W}^T \mathbf{W}) \Delta \mathbf{m}_i = \mathbf{J}_i^T \Delta \mathbf{d}_i - \lambda_i \mathbf{W}^T \mathbf{W} \mathbf{m}_{i-1} \tag{2.15}$$

with the Jacobian matrix $\mathbf{J}$ that contains partial derivatives of the data with respect to the model parameters.

The smoothness-constrained approach (2.14) describes a problem where both the data misfit and the roughness of the model are to be minimized. The regularization factor λ controls the influence of model smoothing. In this study, usually a high initial value λ_0 is used, which is decreased after each iteration step (Loke and Dahlin, 2002) until it reaches a minimum value λ_{min}. Both λ_0 and λ_{min} are parameters for the inversion routine that have to be adjusted depending on the amount of random noise in the model.
An inversion usually starts with a homogeneous starting model consisting of a prescribed number of model blocks, and in each iteration step i the following calculations are made:

- Calculation of the model reaction to determine the modeled data vector of apparent resistivities $\rho_{a,i}$
- Calculation of the discrepancy vector $\Delta\mathbf{d}_i = \rho_{a,i}^{obs} - \rho_{a,i}^{mod}$ as the difference between measured and modeled apparent resistivities
- Calculation of the Jacobian matrix $\mathbf{J}_i$ of partial derivatives of modeled data with respect to the model parameters
- Solving of the least-squares equation (2.15) to determine the desired change in the model parameters $\Delta\mathbf{m}_i$
- Update of the model parameters to receive the initial model for the next iteration: $\rho_{i+1} = \rho_i + \Delta\mathbf{m}_i$

A suitable convergence criterion is used to determine the final resistivity model and stop the iteration process.
The process of solving the least-squares equation involves second-order derivatives (Hessian matrices). In order to reduce the computing time, Loke and Barker (1996) introduced a quasi-Newton method to approximate the Hessian matrix values.

Robust Inversion

The smoothness-constrained least-squares method (2.15) uses the squares of the misfit, and gives larger weight to data points with larger misfits. A different approach using a L_1-norm optimization (minimizing the absolute values of the misfit) was implemented by Loke et al. (2003) following an iteratively reweighted least-squares method (Wolke and Schwetlick, 1988):

$$(\mathbf{J}_i^T \mathbf{R}_d \mathbf{J}_i + \lambda_i \mathbf{W}^T \mathbf{R}_m \mathbf{W}) \Delta \mathbf{m}_i = \mathbf{J}_i^T \mathbf{R}_d \Delta \mathbf{d}_i - \lambda_i \mathbf{W}^T \mathbf{R}_m \mathbf{W} \mathbf{m}_{i-1} \tag{2.16}$$

where $\mathbf{R}_d$ and $\mathbf{R}_m$ are weighting matrices that give different elements of the data misfit and model roughness vector approximately equal weights. This robust inversion scheme is more suitable for models where sharp layer boundaries are expected, while the smoothness-constrained approach favors smooth variations of resistivity transitions.

2.3.4 Petrophysical Relation

The empirical equation of Archie (1942) connects water content and resistivity of consolidated or unconsolidated geologic material to obtain an effective resistivity:

$$\rho_{eff} = \rho_w \Phi^{-m} S_w^{-n} \tag{2.17}$$

with the porosity Φ and a *cementation factor* m that Archie determined to lie in the range of 1.3 for unconsolidated sand to 2.0 for consolidated sandstone (Rubin and Hubbard, 2005). Furthermore, ρ_w is the resistivity of the pore water, S_w the volume fraction of the pore space filled with water and n the *saturation exponent*. This exponent is often considered to be equal to 2, which is not correct for sand material (Dannowski and Yaramanci, 1999). Ulrich and Slater (2004) determined saturation exponents of unconsolidated sands in a range from 1.01 to 2.7.

If a setup is assumed where the same soil volume is measured at different times, and it is further assumed that in the interval between two measurements i and j only the water saturation changes, but the soil structure and the resistivity of the pore water stay constant, the quotient form of Archie's equation can be used to eliminate the porosity:

$$\frac{\rho_i}{\rho_j} = \left(\frac{S_i}{S_j}\right)^{-n} \tag{2.18}$$

so that changes in resistivity can directly be attributed to changes in water content if the material parameter n can be determined. If one measurement is taken at full saturation $S_b = 1$, a simple relation is achieved:

$$\frac{\rho}{\rho_0} = S^{-n} \tag{2.19}$$

with ρ_0 being the resistivity at full saturation.

2.4 Time-Domain Reflectometry

2.4.1 Principles

Time-domain reflectometry (TDR) is one of the geophysical methods based on the different dielectrical properties of dry soil and water. This method originated from cable testing, where damaged spots of subsurface telecommunication lines were detected by measuring the two-way travel time of a transmitted signal reflected at the damaged spot. TDR commonly uses metallic rods as transmission lines. At the end of these rods, an electromagnetic signal is reflected. By measuring the two-way travel time, and because the length of the probe is known, the effective dielectric permittivity ε of the soil surrounding the rods can be determined. As ε differs widely with the amount of water in the pore space of the soil (Davis and Annan, 1989), the water content can be obtained.

A typical TDR probe consists of a probe head and two or three metallic rods acting as a waveguide. The rods are inserted into the host medium and are connected to a pulse generator and oscilloscope via the probe head and a coaxial cable. An electromagnetic plane wave travels these rods. The dielectric permittivity ε can be related to soil water content using relations described e.g. by Topp et al. (1980) or Roth et al. (1990). A review of the TDR technique, design and application is given by Robinson et al. (2003).

2.4.2 Spatial TDR

While conventional TDR systems only measure an integrated value of permittivity along the length of the waveguide, several approaches for retrieving profiles of soil water content along probes have been presented in recent studies

(e.g. Leidenberger et al., 2006; Greco, 2006).
Schlaeger (2005) presented a reconstruction algorithm for obtaining the one-dimensional capacitance distribution along TDR probes, which can be transferred into a permittivity profile. Assuming a medium with little loss, the parameter distribution that leads to the voltage $U(x_0,t;C)$ for a fixed point x_0 and a capacity distribution C is found. The method has also been applied for the shunt conductance G instead of C, and can be extended to work in lossy mediums if both C and G are used (Schlaeger, 2002, 2005). To obtain a parameter distribution, an inversion approach is used where the distance between the modeled $U(t)$ and reflected wave transmission line signal $\eta(t)$ is minimized. The distance is described by a L_2-norm

$$S(C) = ||U(x_0,t;C) - \eta(t)||_2^2 = \int_0^\infty [U(x_0,t;C) - \eta(t)]^2 \, dt \tag{2.20}$$

Minimization of the misfit function S is achieved by applying a steepest descent method.

- Starting from an initial parameter distribution α^0, the direction of steepest descent in the misfit function $\nabla S(\alpha^0)$ is seeked.
- The next parameter distribution $\alpha^{i+1} = \alpha^i - \gamma^i \nabla S(\alpha^i)$ is calculated with a step size γ^i
- The algorithm stops if if the absolute change in parameters falls below a prescribed threshold value

Special flat-band cable TDR probes (called Spatial TDR) have been developed for this method. Using an equivalent circuit model, the capacitance and inductance of the soil can be determined. Schlaeger (2005) derived a function that connects the total capacitance C to the relative permittivity ε of the surrounding soil.
Flat-band Spatial TDR cables have been used in numerous applications, like sealings for waste-disposal sites and landfills (Brandelik and Huebner, 2003; Koeniger et al., 2005) or measurements of snow moisture content (Staehli et al., 2004; Stacheder et al., 2005). TDR and Spatial TDR probes, however, have to be installed in-situ, which makes them difficult to use in cases where the soil can not be disturbed.

2.5 Aspects of Soil Physics

The availability of near-surface soil water is related to the flow of water in the vadose zone. Numerical simulations can be used to predict the spatial and temporal evolution of soil water content. A concise overview of the soil physics is given by Bear (1972) and Stephens (1996). The following description follows the notes by Roth (2006).

2.5.1 Regimes of Water Flow

Water flow in the vadose zone is a multiphase process. A change in water content induces a change in the air phase. As long as the air phase is continuous, the water phase decouples from it and can b considered independently. Three water flow regimes can be differentiated, distinguished by the mobility of the air phase compared to the water phase.

Richards Regime

If the air phase is arbitrarily mobile, the pressure of the air phase p_a is equal to atmospheric pressure. Water movement is described by the Buckingham-Darcy Law

$$\mathbf{j}_w = -K_w(\theta_w)\nabla\psi_w = -K_w(\theta_w)\left[\nabla\psi_m - \rho_w\mathbf{g}\right], \tag{2.21}$$

where $\mathbf{j}_w$ is the flow field, K_w the hydraulic conductivity, θ_w the volumetric water content, ρ_w is the density of water, $\mathbf{g}$ is the gravitational acceleration, ψ_w is the water potential and ψ_m is the matric potential that characterizes a soil's ability to hold water in its pore space.
Conservation of water content is described by the conservation law

$$\partial_t\theta_w = -\nabla\cdot\mathbf{j}_w, \tag{2.22}$$

where ∂_t is a short form of $\partial/\partial t$.
Inserting equation 2.21 into equation 2.22 leads to:

$$\partial_t\theta_w - \nabla\cdot\left[K_w(\theta_w)\left[\nabla\psi_m - \rho_w\mathbf{g}\right]\right] = 0, \tag{2.23}$$

which is called the *Richards equation*. The formulation is completed by describing the material properties $\theta(\psi_m)$ and $K_w(\theta_w)$.
For a process that evolves along a single branch of the strongly hysteretic relation $\theta(\psi_m)$, one can write

$$C_w(\psi_w)\partial_t\psi_w - \nabla\cdot[K_w(\theta(\psi_m))\,[\nabla\psi_m - \rho_w\mathbf{g}]] = 0, \tag{2.24}$$

where $C_w(\psi_m) := d\theta/d\psi_m$ is the *soil water capacity function*. Equation 2.24 is referred to as the *ψ-form of the Richards equation*. In this study, the formulation of dynamics in the Richards regime is used for numerical models, even if the soil approaches full water saturation and the assumption of an arbitrarily mobile air phase breaks down.

Continuous Multiphase Regime

In this regime both water and air phase are considered continuous. Considering an incompressible air phase, a uniform medium and one-dimensional horizontal flow, the flux laws are

$$\begin{aligned} j_a &= -K_a(\theta_a)\partial_x\psi_a && (2.25)\\ j_w &= -K_w(\theta_w)[\partial_x\psi_m + \partial_x\psi_a], && (2.26) \end{aligned}$$

where the subscripts a and w refer to the air and water phase, respectively, and $\psi_w = (p_w - p_a) + (p_a - p_0) = \psi_m + \psi_a$. While ψ_m, the matric potential, refers to the pressure in the air phase p_a, ψ_a refers directly to the reference pressure p_0 (see e.g. Ippisch, 2001).

Discontinuous Multiphase Regime

When the continuity of the air phase is lost, air residuals remain, typically in cavities and pores, that are enclosed by the water phase. Air may leave such regions only through processes like bubbling or dissolving. The formulations for the multiphase regime are useless here. A solution for including bubble formation and dissolution processes has not been reached yet.

2.5.2 Material Properties

A soil is characterized by its material properties. Of particular importance are the relations between water saturation, hydraulic head and conductivity.

Soil Water Capacity $C_w(\psi_m)$

The soil water capacity $C_w(\psi_m)$ depends on statistical pore space properties like the distribution of bottle-neck radii and cavities, and on interfacial properties of the fluids and of the solid matrix.

Traditionally, instead of the capacity, the soil water characteristic $\theta_w(\psi_m)$ is parameterized. Based on the *effective water saturation*

$$\Theta := \frac{\theta_w - \theta_r}{\theta_s - \theta_r}, \tag{2.27}$$

where θ_r is the residual and θ_s the saturated water content, and the matric head

$$h_m := \frac{\psi_m}{\rho_w g} = \frac{p_w - p_0}{\rho_w g}, \tag{2.28}$$

the soil water characteristic can be parameterized in different ways. The most common ways were developed by Brooks and Corey (1966) and van Genuchten (1980).

The Brooks and Corey model is defined as

$$\Theta(h_m) = \begin{cases} [h_m/h_0]^{-\xi} & ; h_m < h_0, \\ 1 & ; h_m \geq h_0, \end{cases} \tag{2.29}$$

where the scaling factor h_0 represents the air entry pressure of the largest pore and ξ is a pore size distribution index. The van Genuchten parameterization is given as

$$\Theta(h_m) = [1 + (\alpha h_m)^n]^{-1+1/n} \tag{2.30}$$

The scaling parameter α corresponds to an air entry value $1/\alpha$ and n is a shape factor.

Equation 2.29 can be inverted to obtain $h_m(\Theta)$ for $\Theta < 1$. Equation 2.30 can be inverted for all Θ.

Hydraulic Conductivity

Mualem (1976) obtained a parameterization for the conductivity as

$$K(\Theta) = K_0^l \left[\frac{\int_0^\Theta h_m(\vartheta)^{-1} d\vartheta}{\int_0^1 h_m(\vartheta)^{-1} d\vartheta} \right]^2 , \tag{2.31}$$

where the saturated conductivity K_0 is a parameter, l accounts for the tortuosity of the flow channels and ϑ is a variable of integration.
The Mualem approach can be combined with the Brooks-Corey or van Genuchten parameterization for $h_m(\Theta)$ to obtain parameterizations for $K(\Theta)$ and $K(h_m)$.

2.5.3 Simulation of Flow in the Richards Regime

For the simulation of water flow in the subsurface, the numerical code implemented in the HYDRUS software was used, which also includes e.g. routines to create finite-element meshes.

Numerical solution of the water flow equation

The domain is subdivided into a grid of finite triangular elements. If piecewise linear basic functions $\phi_n(x_m, z_m) = \delta_{nm}$ are assumed, where δ is a Kronecker-Delta, the matric head can be approximated as

$$h'(x,y,z,t) = \sum \phi_(x,y,z,t) h_n(t), \tag{2.32}$$

where for n nodal points $h_n(t)$ is an unknown coefficient representing the solution of (2.23) at these nodal points.
The Galerkin finite-element method (e.g. Pinder and Gray, 1977) is applied, which leads to a system of time-dependent ordinary differential equations of the form

$$\mathbf{F} d_t \theta + \mathbf{A}\mathbf{h} = \mathbf{Q} - \mathbf{B} - \mathbf{D} \tag{2.33}$$

The content of the matrices **F**, **A**, **Q**, **B** and **D**, the time discretization and the way (2.33) is solved can be found in Simunek et al. (2006).

Hysteresis in the Soil Hydraulic Properties

HYDRUS implements hysteresis following Kool and Parker (1987). This approach is based on an empirical model (Scott et al., 1983) with a modification for air entrapment. The model uses separate parameter sets $(\theta_r^i, \theta_S^i, \alpha^i, n^i)$ for wetting $(i = w)$ or drying $(i = d)$. For most applications, the following simplifications are reasonable: $\theta_r^d = \theta_r^w$, $n^d = n^w$ and $\alpha^w = 2\alpha^d$ (Kool and Parker, 1987; Nielsen and Luckner, 1992). This model can suffer from so-called pumping, in which the hysteresis loop can move to physically unrealistic parts of the retention function. Alternative models that keep track of antecedent reversal points have been introduced Lenhard et al. (e.g. 1991).

Boundary Conditions

Various boundary conditions are possible. These can be system-independent boundary conditions, which are pressure head (Dirichlet) conditions $h(x,y,z,t) = \chi(x,y,z,t)$ for the pressure head h and a point (x,y,z) on a Dirichlet boundary, or flux (Neumann) boundary conditions given as $-\partial_x h\hat{n} = \zeta(x,y,z,t)$ for an outward unit vector $\hat{n}$ on a Neumann boundary.

A system-dependent boundary condition that is applied in this study is the *atmospheric boundary condition*. The potential flux across the soil-air interface is controlled by defining a maximum potential rate of infiltration depending on the atmospheric conditions and by limiting the pressure head h to a range of $h_A \leq h \leq h_S$ for the minimum and maximum allowed pressure head h_A and h_S. The value for h_A is determined from the equilibrium conditions between soil water and atmospheric water vapour. h_S is set to zero under the assumption that no surface ponding is possible.

Further system dependent boundary conditions are the *seepage face*, which allows water to leave the modeled domain when saturation occurs. A zero pressure head is assumed at this boundary, and excess water to be removed from the system entirely upon leaving the domain. The *drain* boundary is similar to the seepage face, but in contact to the unsaturated zone it will act as a nodal sink.

3 Soil water content monitoring on a full-scale dike model

The first aim of the thesis is to determine whether ERT is suitable to quantify water content. ERT has been chosen because

- it is a non-intrusive method (in contrast to TDR, see below),
- it can be used to monitor and quantify changes in water content in two or even three dimensions and
- it is fast to install and can be automated for monitoring purposes.

Preliminary studies conducted on laboratory scale dikes (appendix A) already showed that ERT, in combination with other geophysical methods, has the potential not only to identify relative water content changes, but to also quantify them.

In this chapter, the use of ERT for monitoring of the soil water content evolution in a flood-protection dike that is influenced by flooding and rainfall events is explored. It is shown that, in combination with an initial water content estimate, ERT monitoring can be reliably used to retrieve two-dimensional soil water distributions within the dike body and their temporal evolution. In several test studies, both Spatial TDR and GPR were employed to retrieve the initial water content. In this chapter Spatial TDR results are used for initial water content retrieval and for the verification of the results.

3.1 Field Site

The full-scale dike model is located at the Federal Waterways Engineering and Research Institute in Karlsruhe, Germany (Fig. 3.1). It has a height of 3.6 m

Figure 3.1: *View from top on the full-scale dike model at the Federal Waterways Engineering and Research Institute Karlsruhe, Germany, during the flooding experiment.*

and a length of 22.4 m. The dike model is built up homogeneously of uniform sand (with grain sizes between 0.2 and 2 mm) with a thin surficial soil layer covered by grass. It is based on a waterproof sealing of plastic, so that infiltrating water will be stopped at the base. This will cause lateral flow to a drain of gravel material at the foot of the landside slope. Without this drain, the water would seep out of the slope with all the consequences regarding erosion and slope stability. The detailed setup of the dike model and its permanent instrumentation is described in Scheuermann (2005).

For measurements of the spatially distributed water content using Spatial TDR (see section 2.4.2), the dike model is equipped with 12 vertically installed flat band cables with lengths between 1 and 3 *m*. Six of them are installed on the land-side slope of the dike, where ERT measurements were conducted (Fig. 3.2). Data acquisition time for all 12 Spatial TDR cables takes only 5 minutes (Scheuermann, 2005). The measured TDR traces are subsequently processed into spatial distributions of the permittivity and the volumetric water content along the individual cables using the Spatial TDR reconstruction algorithm by Schlaeger (2005). Changes in water content are determined with a spatial accuracy of about 3 cm with an average deviation of ±2 vol-% compared to independent water content measurements (Scheuermann et al., 2001). The 12 individual cables are horizontally interpolated to yield a 2-dimensional cross-section of the dike.

3.2 Data Acquisition

Electrical Resistivity Tomography

ERT measurements were taken along an 8 m line perpendicular to the crest down the land-side slope of the dike using a SYSCAL junior system (Iris Instruments) comprising of 48 electrodes with a spacing of 16 cm (Fig. 3.2). The electrodes were placed along a parallel line at 1 m distance from the positions of the Spatial TDR cables to ensure comparability of ERT and Spatial TDR.
Measurements were taken on a daily basis with additional measurements during the rainfall and flooding experiments (see Table 3.2). For all measurements, the Wenner-Schlumberger electrode array was used as a good compromise between accuracy and measurement duration. One measurement cycle took approximately 40 minutes to complete.
Water conductivity was measured in a storage tank behind the drain as well as in the flooding basin on the water side of the dike. Throughout the experiments, the water conductivity in both reservoirs differed only by about 50 Ωm, compared to 5000 Ωm resistivity of the dike material at field capacity (volumetric water content of $7-8\%$), which validates the assumptions used in Eq. (2.17) and (2.19).

Data Inversion

The observed apparent resistivity is inverted using the software RES2DINV (Loke and Barker, 1995) with the robust inversion (use of L_1-norm for data and model space) scheme (2.16).
Robust inversion is usually prefered over smooth inversion when sharp layer boundaries are expected, as they are reproduced better than with the more smearing least-squares norm. For the two experiments presented in this chapter (a simulated rainfall on the surficial soil layer, and a flooding experiment yielding a stationary phreatic line within the dike body), sharp resistivity con-

trasts directly at the boundary between the top layer and the dike material were expected. Consequently, robust inversion was chosen for all data sets in this contribution. Equation (2.16) is solved iteratively until the root-mean square (RMS) of the discrepancies g does not alter significantly after an inversion step and/or it becomes smaller than the measurement accuracy, which is estimated to be around 3% due to the comparatively homogeneous set-up of the dike model. However, a small RMS error does not necessarily correspond to a realistic inversion result. In particular, when using an inversion code like RES2DINV, which does not rigorously optimize with respect to the chosen model characteristics (e.g. minimization of model roughness) for a pre-selected data error level, a large number of iterations will tend to overfit the data and thus create artifacts (Hauck and Vonder Muehll, 2003). With such an inversion code, especially large resistivity contrasts tend to be increased yielding large resistivity variations from one iteration to the next without a significant change of the RMS error. To avoid this problem, a sort of L-curve criterion is applied here based on the apparent L-shape of the curve obtained by plotting the RMS error against the iteration number. By choosing the inversion result from the iteration at the apparent bend of the L-curve, a compromise between low RMS error and small number of iterations is achieved. This criterion results in inversion models with RMS errors of $2\ldots4\%$ for most of the data sets. With regard to the data measured on a dike slope, topographic modeling is used during data inversion.

Time-lapse inversion techniques have been introduced to jointly invert data sets taken at different times. The initial inversion of the data set is used to constrain the following inversions to ensure that temporal differences between the model resistivities vary in a smooth manner and to minimize artifacts introduced by inverting each data set separately (Loke, 1999; LaBrecque and Yang, 2001). However, from experiences with RES2DINV, problems may arise when inverting data sets with large temporal resistivity changes tend to become unrealistically amplified in time-lapse inversion modes. In this study, both individual and time-lapse inversions of the data sets are performed.

Meteorological conditions

A meteorological station collecting all energy balance variables was set up next to the model dike. The station was equipped with sensors for rainfall, short-

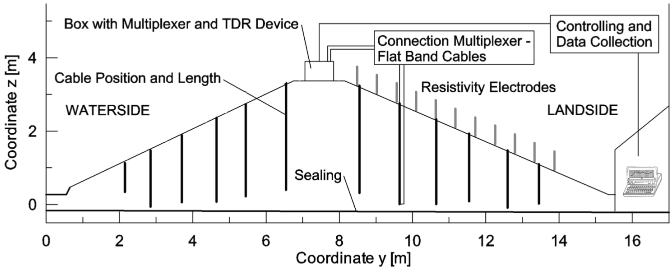

Figure 3.2: *Location of Spatial TDR flat band cables and ERT electrodes in the cross-section of the dike. ERT measurements are only conducted down the land-side slope of the dike.*

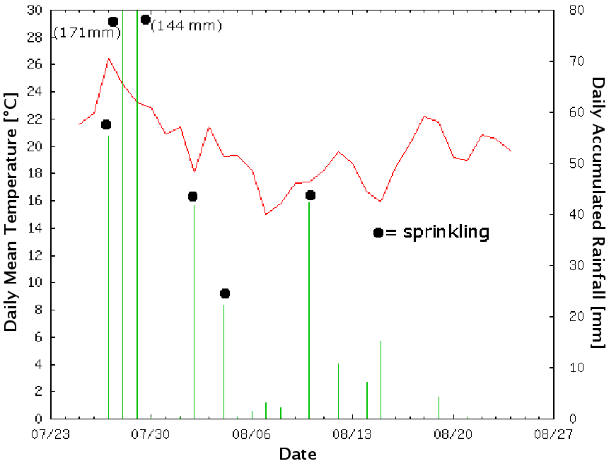

Figure 3.3: *Overview of temperature and rainfall for the duration of the dike experiment. Marked with black dots are days where sprinkling was added to the accumulated rainfall.*

and long-wave radiation, moisture, air pressure, wind speed, air temperature, ground temperature and ground heat flux.

Rain events were simulated by two conventional water sprinklers, with two additional rain gauges on the land-side of the dike measuring the simulated rainfall. To cover the whole dike slopes with the sprinklers, they had to be operated at maximum water output. This led to an output of approximately $10\ldots15\ mm/h$ corresponding to a heavy rain event.

Figure 3.3 shows an overview of the meteorological conditions during the experiment. The rainfall was measured with one of the rain gauges on the dike, and temperature was retrieved from ultrasonic thermometer data. The rainfall data includes both natural precipitation and sprinkling; days with sprinkling are marked by black dots. As can be seen from Fig. 3.3, sprinkling exceeded rainfall by one to two orders of magnitude. During the first two days of the experiment the dike was irrigated during the night, for 8 hours during the first and 10 hours during the second night. On August 2nd, 4th and 10th short rainfall events were simulated, where the sprinkling was running for two hours, and ERT measurements were taken before, during and afterwards (Table 3.2).

The experiments concluded with a flooding event. The water level in the basin was raised to 1 m below the dike crest as can be seen in Fig. 3.1. As no rising of the water level was possible during the night, reaching the final height of 2.43 m took one and a half days. After the following night, a steady state had been established and a final ERT measurement was taken before the water level was lowered again.

3.3 Results and Discussion

From the series of experiments shown in Table 3.2, two case studies are chosen to illustrate the advantages and disadvantages of surface-based ERT for water content estimation within the dike model.

Case Study I: Rainfall Event

A first example is given in Fig. 3.4, showing ERT profiles before and after a short rainfall event (see Table 3.2). In Fig. 3.4b (after the rain), a decrease in resistivity is clearly visible within the top layer, as well as within the dike body

Measured Event	Interval between measurements [h]
Daily routine measurement from 20/07/05 - 23/08/05	24
Long rainfall events overnight from 27/07/05 to 29/07/05	10-12
Short rainfall events for 2 hours on 02/08/05, 04/08/05, 10/08/05	1
Flooding from 17/08/05 - 19/08/05	1-2 (during daytime)

Table 3.1: *Overview of measurements taken on the BAW full-scale model dike.*

towards the drain. To quantify absolute water content evolution, changes in resistivity due to changes in water content must be determined. Figure 3.5 shows the resistivity difference between the separately inverted tomograms from Fig. 3.4. In the top layer, resistivity decreases as expected. But in contrast to expectation, an apparent increase in resistivity is visible in the dike body (red coloured area) which can not be explained in terms of a physical process in the context of the rainfall event. Previous rainfall experiments resolved with the Spatial TDR method (Scheuermann, 2005) showed that for such a short rainfall no water is expected to infiltrate into the dike body. Therefore, an increase in resistivity is not plausible. When inverting the two data sets in time-lapse mode, the increase in resistivity at greater depths is even larger.

To address this problem, two apparent resistivity data sets are constructed from resistivity models (incl. 3% noise) using the forward modeling algorithm RES2DMOD (Loke, 1999). In numerous applications and studies, forward modeling of synthetic data sets has been used to gain additional insight and confidence in the measurements and the inversion process (e.g. Loke and Dahlin, 2002; Godio and Naldi, 2003; Hauck and Vonder Muehll, 2003; Nguyen et al., 2007). The simulated measurements are subsequently inverted using the same inversion parameters as for the observed data sets. The synthetic resistivity model at time t_0 consists of a low resistivity top layer and two nested blocks of higher resistivity representing the dike body (Fig. 3.6a). The two nested blocks differ in resistivity, with a higher resistivity area representing the inner part of

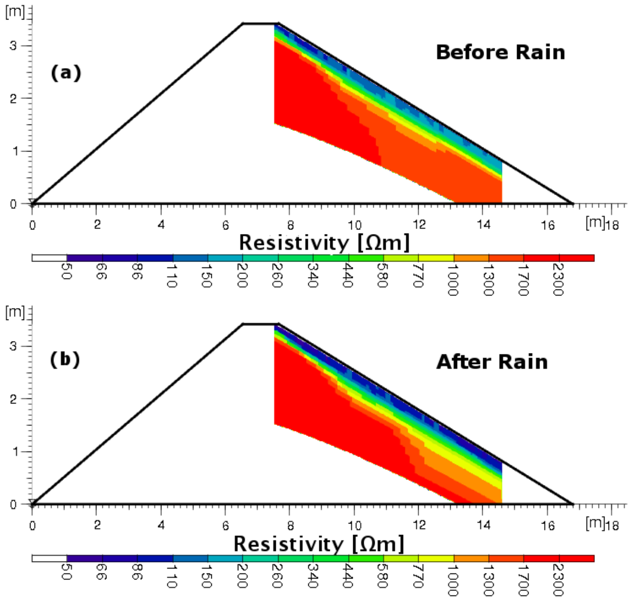

Figure 3.4: *Resistivity distributions (a) before and (b) after a short intense rainfall of 2 hours on August 4th.*

the dike body, and an area with lower resistivity representing the part of the dike towards the drain (right block in the image). For the second resistivity model at time t_1, only the resistivity in the top layer is decreased from 450 Ωm to 200 Ωm (a decrease to 44% of the original resistivity) to simulate the effect of the water input due to rainfall. A comparison of the inverted resistivity models obtained with RES2DINV shows not only a decrease in resistivity in this upper layer, but also an increase in the lower layers (Fig. 3.6b), similar to the inversion models of the rainfall experiment (Fig. 3.4). From this it can be concluded that the observed resistivity increase within the dike body during the rainfall experiment is due to an inherent inversion artifact.

By looking at the change in the sensitivity distribution of the ERT array in the field case before and after the rainfall event (Fig. 3.7), it becomes obvious that

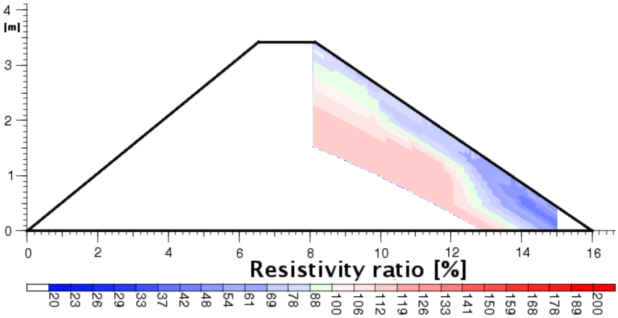

Figure 3.5: *Change in resistivity for the rainfall experiment. An apparent increase in resistivity is visible in the dike body (red area), whereas the resistivity decreases within the top layer and towards the drain on the foot of the dike (blue area).*

the loss in sensitivity below the conductive surface layer is responsible for the development of the artifact. To overcome this deficiency, depth-depending regularization can be used. Figure 3.8 shows the change in resistivity before and after the rainfall similar to the inversion shown in Figure 3.5, but with increasingly stronger regularization at greater depth, where the sensitivity loss through the increased water content within the surface layer is largest. Within the surface layer the resistivity decrease is similar compared to the results shown in Figure 3.5. At greater depths, the anomalous resistivity increase is reduced to less than 10%.

Case Study II: Flooding Experiment

As a second case study, a flooding experiment was conducted. For this experiment, the relative sensitivity distribution is much more favourable than for the rainfall experiment, due to the absence of a strong resistivity decrease at the surface (Figure 3.9). Fig. 3.10 shows the height of the water level during the flooding experiment over time. Marked with letters are the measurement times for which Fig. 3.11 shows the resistivity tomograms. The sections shown were taken before the flooding started (A), at the end of the first day (B) and contin-

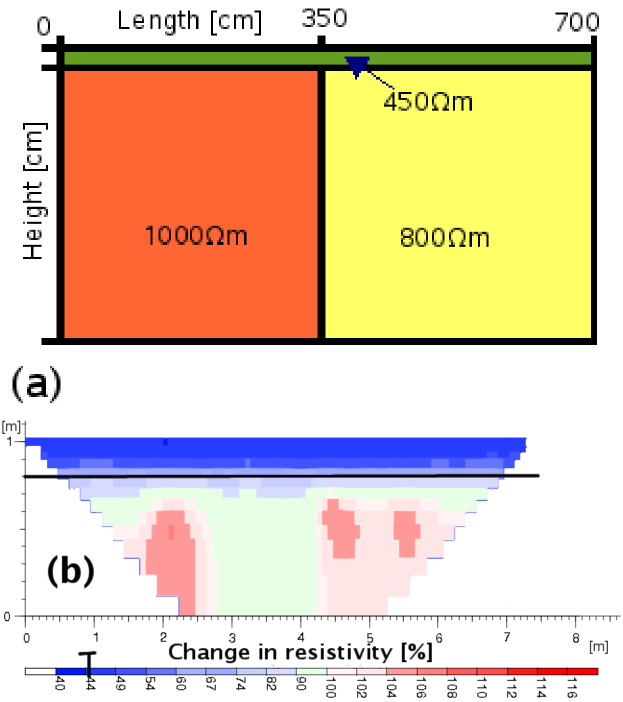

Figure 3.6: *(a) Model block arrangement of the synthetic resistivity model, with low resistivity within the top layer and two blocks representing the dike body, with lower resistivity towards the drain (right block). (b) Inversion results after forward modeling and adding 3% noise on the resulting apparent resistivities. Marked are the layer boundary and the expected decrease in resistivity of 44% on the colour scale.*

ued to be taken twice a day until a steady state was reached (E). In (B), 5 hours after the flooding started, only a slight change in resistivity can be seen as not much water had flown through the dike. Overnight, more water seeped through the dike and a decrease in resistivity at greater depth can be seen, though higher regions of the dike are not reached due to the low water level (C). During the

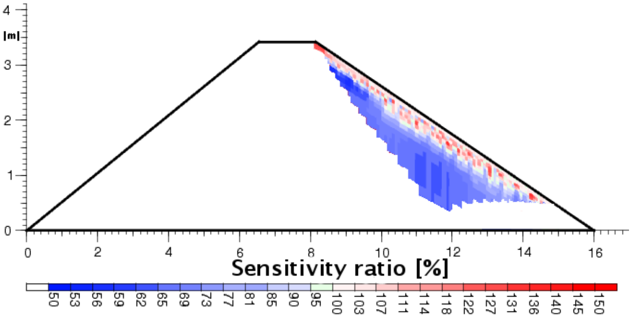

Figure 3.7: *Distribution of relative sensitivity difference before and after the rainfall experiment. The relative sensitivity is the sum over each column of the sensitivity matrix* **J**.

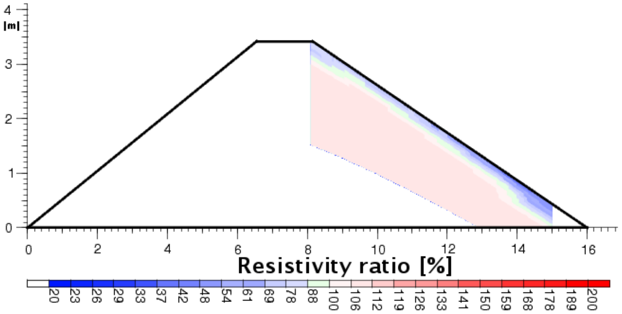

Figure 3.8: *Change in resistivity for the rainfall experiment (as in Figure 3.5) but for an inversion with increasing regularization with depth.*

second day, the water level was raised to a final height of 2.43 m (D). Here, it can be seen that the resistivity is still decreasing, and starts to decrease in higher layers. During the night, steady state was reached as is clearly visible in (E). Resistive anomalies evolve near the model boundaries in (C) to (E). Inversion models are typically less reliable at the boundaries, however, in this case the

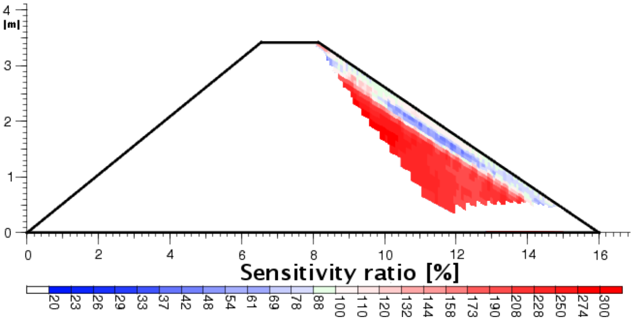

Figure 3.9: *Distribution of relative sensitivity difference between rainfall and flooding experiment. The relative sensitivity is the sum over each column of the sensitivity matrix* $\mathbf{J}$.

presence of the drain (right boundary) and a small stone pavement on top of the dike (left boundary, see Fig. 3.1) may also enhance the tendency for resistive anomalies during inversions. The phreatic line, that is the line delimiting the completely saturated area inside the dike, is indicated in this figure. It was derived from measurements with pore pressure sensors at the base of the dike. The part of the tomogram where the decrease in resistivity is strongest agrees well with the area marked by this line. It is also seen that the area immediately above the phreatic line exhibits an increase in water content which is close to saturation. Small deviations between the shape of the phreatic line and the area of strongest resistivity decrease are due to the size and distribution of the inversion model blocks.

Saturation Exponent

To convert the resistivities obtained from the ERT measurements to water content distributions, the saturation exponent in Eq. (2.19) has to be determined. To estimate this exponent, the resistivities from ERT surveys are plotted against the water contents retrieved from Spatial TDR. Because the investigation volume of the TDR measurements is restricted to the immediate vicinity of the sensor cables and because of the difference in vertical resolution of both methods (ver-

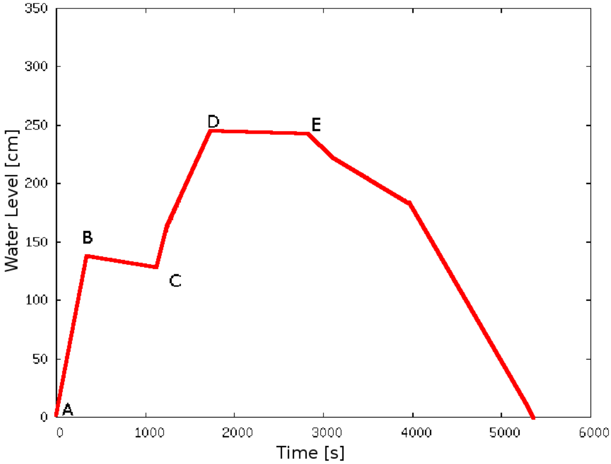

Figure 3.10: *Height of the water level during the flooding experiment, starting August 17th at 13:30. The letters mark the measurement times of the tomograms shown in Fig. 3.11.*

tical TDR cables having a much higher vertical resolution at larger depths), resistivity and saturation values are vertically averaged along the position of each Spatial TDR cable for each measurement. Due to the homogeneity of the dike material with a known porosity of 37%, saturation values can be converted into water contents and vice versa. To obtain a reliable estimate for the saturation exponent, data cables near the drains are omitted as the influence of the drain material resulted in higher resistivities there. Likewise, data from the rainfall experiment are excluded. All daily measurements and the flooding experiment measurements were considered.

Equation (2.19) is then fitted to the data using initial parameters of $n = 2$ and $\rho_0 = 250\,\Omega m$. The least-squares fit (Fig. 3.12) (obtained with the the Levenberg-Marquardt method) resulted in estimates of $\rho_0 = 237 \pm 16\Omega m$ and $n = 1.16 \pm 0.07$. In a laboratory study, Ulrich and Slater (2004) determined $n = 1.29 \pm 0.17$ for a comparable unconsolidated sand. Bieberstein (1999) determined relation-

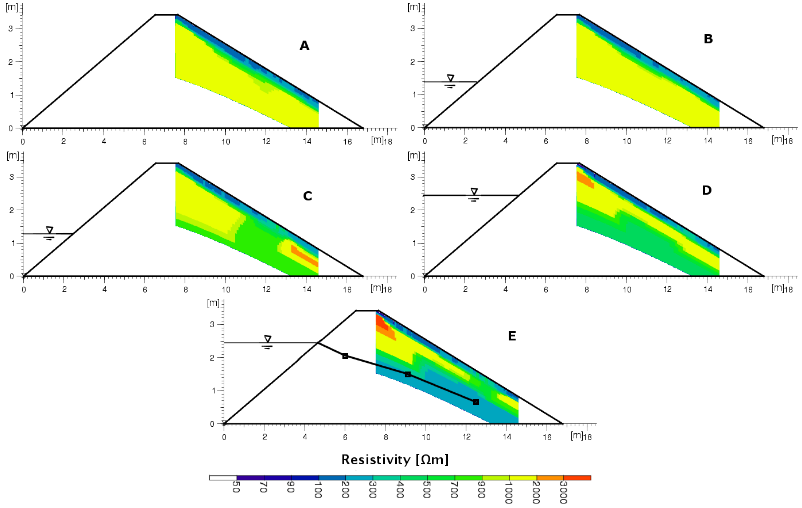

Figure 3.11: *Resistivity distributions during flooding experiment, taken on* **A**: *August 17th, 13:30;* **B**: *August 17th, 18:50;* **C**: *August 18th, 08:50;* **D**: *August 18th, 18:30,* **E**: *August 19th, 09:45, with phreatic line (marking the saturated area).*

ships of saturation and resistivity for a large range of different materials. Using a fit similar to the one described above, a saturation exponent of $n = 1.18 \pm 0.04$ is determined for a similar sand.

Water Content Changes

To quantify the change in water content over the duration of the flooding experiment, and to compare it with water contents retrieved by the Spatial TDR method, Archie's equation (Eq. (2.17)) was applied. The estimated saturation exponent of $n = 1.16 \pm 0.07$ was used. A Spatial TDR cable in the middle of the land-side slope was chosen for comparison. Along this cable, the change in water content is shown in Fig. 3.13 as the ratio of water content between the two measurements after (Fig. 3.11E) and before the flooding (Fig. 3.11A). The

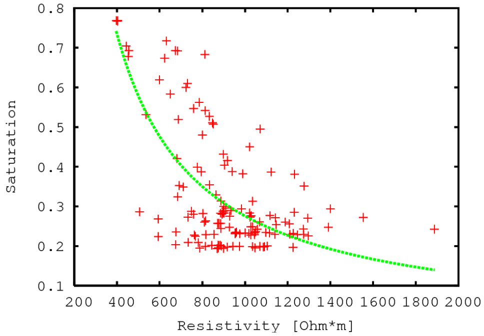

Figure 3.12: *Fit of Archie saturation exponent n and resistivity at saturation* ρ_0 *based on resistivity data (ERT) vs. saturation data (Spatial TDR), averaged along the respective Spatial TDR cable positions.*

red line corresponds to the ERT data with the error estimate from the saturation exponent.

The vertical ERT resolution is much lower due to the employed parametrization of the model in the inversion process, which uses 862 blocks on 11 layers, with a sensitivity decrease of the model with depth. The model discretization leads to the stepwise form of the curve. The overall agreement between both methods is due to the applied relationship between resistivity and saturation, which was calibrated using the TDR data. Differences are seen in the top 20 cm, where almost no change in water content is detected by the Spatial TDR. In contrast, ERT detects an apparent decrease in water content. Strictly speaking, both the Spatial TDR calibration and the estimated saturation exponent are not valid for this surface layer. Potentially, an inversion artifact similar to the one described above may be present, where a strong decrease in resistivity in the dike body causes an increase in the top layer, which is unaffected by the flooding and too strong to have been caused by evapotranspiration.

Using an initial water content distribution from Spatial TDR and adding the change from ERT, the full two-dimensional water content distribution is obtained from the ERT inversion model (Fig. 3.14). The water content in the

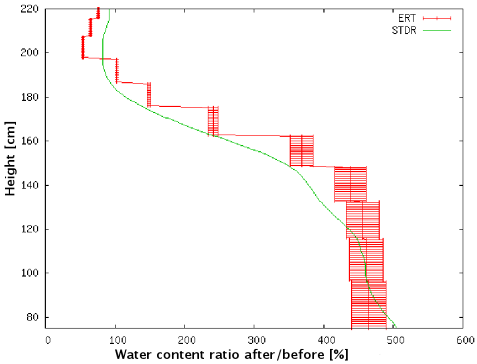

Figure 3.13: *Vertical profile of the water content ratio between measurements after and before the flooding experiment along one Spatial TDR cable positioned at the middle of the land-side slope. ERT measurements were transferred to water contents using the fitted saturation exponent with the estimated error margin from the fitted resistivity-saturation relationship. The green line is the ratio retrieved from Spatial TDR.*

lower part of the plot is close to the expected water content at saturation of about 34% - Scheuermann (2005) showed that at full saturation, the volumetric water content is only at 90% of the porosity (37%) due to air inclusions. In the lower right corner, the water content is unnaturally high. This can be explained by the fact that the water content above the water-proof sealing is higher as some water is dammed and retained here. The resolution of the ERT survey geometry used in this study is too coarse to detect this water, but the Spatial TDR-cables, being installed in-situ, do sense this water. Consequently, the changeover from coarse to fine scale causes an overestimation of calculated changes in ERT in this part. In the upper parts, the water content is slightly underestimated. This may be again due to the inversion artifact described above, which leads to an apparent increase in resistivity in those parts where no or only very small change was present.

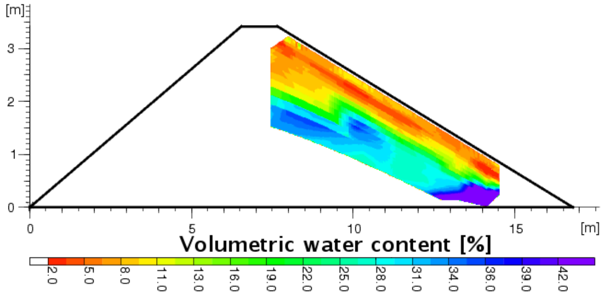

Figure 3.14: *Volumetric water content distribution after the flooding experiment derived from ERT with an initial water content distribution from Spatial TDR measurements.*

3.4 Conclusions

The feasibility of using TDR-calibrated ERT-monitoring to quantify soil water contents was demonstrated in applications to flooding and rainfall experiments on a full-scale dike model. Deviations in the inversion results were interpreted as inversion artifacts after remodeling the effects using synthetic data. By applying depth-depending regularization, this artifact could be significantly reduced. The necessary parameters for Archie's equation were estimated. In combination with initial water content profiles from Spatial TDR (or GPR), two-dimensional water content distributions were obtained. The main results of this study include:

- ERT is a viable method to quantify changes in water content under certain conditions. By applying the equation of Archie (1942), changes in resistivity measured in repeated surveys can be translated to changes in water content, provided that a suitably calibrated resistivity-saturation relationship is available.

- Inversion artifacts, generated for cases with reduced sensitivity due to an increase in conductivity at the surface, could be reduced by applying vertically varying regularization, with increasing damping factors with depth. Forward modeling of synthetic data sets is a useful tool to detect, analyze and reduce the generation of inversion artifacts.

- The water content evolution during a flooding experiment could be reliably determined with ERT. The phreatic line, that is the line marking the saturated area inside the dike, was accurately determined.

The saturation exponent in Archie's equation was estimated for the sand material present within the dike body. This was done without laboratory data, but by combining saturation information from the Spatial TDR method with resistivity data and fitting the equation. A saturation exponent of $n = 1.16 \pm 0.07$ was determined.

4 Measuring water content on sites of varying heterogeneity

In the previous chapter, ERT was demonstrated to be a viable method for retrieving water contents. However, it already became clear that the quantifications presented were possible because of two conditions: The availability of a direct comparison method (Spatial TDR) and the laboratory-like conditions of a homogeneous dike.

On real dikes, unknown layered structures or lateral heterogeneities will occur. If the geophysical methods are applied for measuring the water content on larger scales, e.g. for inclusion in meteorological models, the question of lateral heterogeneity will become the defining problem of the analysis.

Geophysical techniques have different sensitive volumes. Probes with very small measured volume can be considered pointlike from a field scale perspective, and include time domain reflectometry (TDR) and frequency domain reflectometry (FDR) probes among others. The reliability of the individual methods and the choice of methods depend not only on the application, but also on the prevalent variability of soil properties and water content.

In this chapter, the aim is to evaluate what method or combination of methods may provide suitable measurements, what deficencies single methods can exhibit and whether combinations of methods can be employed to overcome these. Results from several geophysical investigations[1] are studied regarding their ability to determine water content and its variability on sites of different heterogeneity. Factors influencing the applicability of a method include the measurement volume of the method, the depth and resolution of water content needed and the heterogeneity in soil properties.

---

[1] Data has kindly been provided by K. Preko (Geophysical Institute, University of Karlsruhe) and M. Bach, M. Kohler, F. Königer and L. Krauß (IMK, Forschungszentrum Karlsruhe).

4.1 Additional Methods

The additional methods explored in this chapter included TRIME-TDR, FDR and GPR methods.

4.1.1 TRIME-TDR

TDR probes usually are built as three-rod probes that have to be installed in situ. Besides the conventional TDR probes, time domain reflectometry with intelligent microelements (TRIME-TDR) allows measurements of vertical soil water content profiles when brought into indirect contact with the soil through an access tube. The TRIME-TDR system uses an algorithm that records the arrival times of specific voltage levels (Stacheder et al., 2001) which records the entire voltage trace, and determines the two way travel time of the reflected pulse based on the trace shape.
The TRIME T3 Tube Access Probe from IMKO, which was used in this study, comprises of a 18 cm long probe that can be stepwise inserted vertically within insulating tecanat plastic tubes. The device generates a high-frequency pulse (up to 1 GHz) which propagates along metal shells, generating an electromagnetic field around the probe. At the end of the shells, the pulse is reflected back to its source. The soil water content can be determined by measuring the resulting transit time (10 ps…2 ns). The volumetric water content is then automatically calculated from the transit time using a general calibration. The TRIME system can also be equipped with a conventional three-rod probe.

4.1.2 FDR

Frequency domain reflectometry (FDR) is based on the principle of using soil as a dielectric medium for a capacitor and determining the electrical capacitance, which is influenced by soil water content (e.g. Charlesworth, 2005).
The Simplified Soil Moisture Probe (SISOMOP), based on the FDR principle, consists of a ring oscillator based on a digital inverter driving a transmission line where the end feeds the input. The oscillation frequency is lower for higher effective dielectric permittivity, and thus depends on the soil water content. The relation between relative dielectric permittivity ε_r and the oscillation frequency

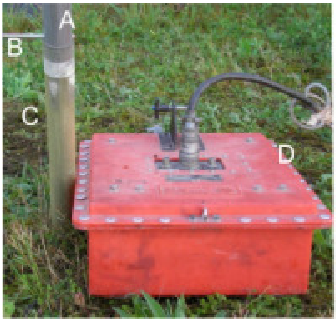

Figure 4.1: *Application of GWS in the field. A: Metallic cylinder, B: Stepwise adjustable fixation, C: Vertical access tube, D: GPR antenna.*

(or moisture counts, MC) has been verified using laboratory test series yielding a accuracy of $\pm 0.04 m^3/m^3$ (Schlaeger et al., 2005).

4.1.3 Ground-Penetrating Radar

The ground penetrating radar system used was a surface interface radar (SIR-3) system from Geophysical Survey Systems Inc. (GSSI). Two monostatic 300 MHz antennas and a bistatic 900 MHz antenna were used in the ground wave and reflection experiments, respectively. A thorough discussion of the methods and measurements is given by Preko (2008).

Guided Wave Sounding

GWS is an invasive application of the GPR technique in an operational mode similar to that of conventional TDR (Igel et al., 2001). A metal cylinder is lowered in steps into an access tube vertically installed in the soil (Fig. 4.1). Electromagnetic waves guided along the metal cylinder are reflected from its base back to the receiver antenna. In this study, the raw data was processed using the software package REFLEXW (Sandmeier, 2007) and the determined internal velocities of the guided wave were related to ε_r. Figure 4.2 shows a

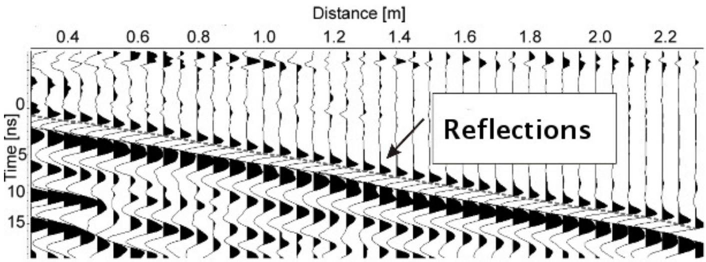

Figure 4.2: *Processed radargram of a GWS survey. The reflection from the metallic rod is clearly identifiable.*

processed radargram, where the reflection from the gradually lowered reflector is clearly visible.

Ground Wave

Initially, the receiver position is fixed and the transmitter is gradually moved along the transect until an optimal transmitter-receiver separation is found with regard to the identification of the ground wave (WARR method). Using this optimal antenna separation and a supporting wood frame, the system is moved along the transect (CO method).
Data processing comprises the determination of the air wave arrival time, which acts as a reference in calculating the zero time. Subtracting this zero time from the arrival time of the apparent ground wave gives the time taken for the ground wave to travel from the transmitter to the receiver. From this travel time, ε_r of the top soil can be computed and consequently, the soil water content can be calculated using e.g. the empirical relationship by Topp et al. (1980):

$$\theta_w = -5.3 \cdot 10^{-2} + 2.9 \cdot 10^{-2}\, \varepsilon_r - 5.5 \cdot 10^{-4}\, \varepsilon_r^2 + 4.3 \cdot 10^{-6}\, \varepsilon_r^3 \qquad (4.1)$$

Table 4.1: *Overview of the different geophysical methods and the combination of methods applied on the three sites.*

Field Site	TDR	FDR	GWS	CO	ERT
Dike	x		x		x
Heselbach	x	x			x
Africa	x	x		x	

4.2 Field Sites

4.2.1 Full Scale Dike Model

In a second experimental phase on the full-scale dike model (see section 3.1) in April 2007, two events were monitored using geophysical methods: 1) a long precipitation and 2) a flooding experiment. Measurements were taken with three methods: TRIME-TDR using an access tube probe, GWS and ERT (Table 4.1).

For the simulated long precipitation period of 56 hours over the course of 4 days, measurements were taken before (naturally dry condition) and afterwards (wet conditions). TDR and GWS measurements used a tube installed vertically into the dike on the waterside slope 30 cm below the dike crest. The ERT measurement line with 48 electrodes was installed parallel to the crest on the waterside.
For flooding, the water level in the basin was raised to 2.4 m. Stationary flow conditions were allowed to establish before measurements were taken. For GWS, a tube on the landside slope was used. Unfortunately, this tube did not allow the application of TRIME-TDR. Finally, a 24-electrode ERT array was installed perpendicular to the crest down the landside slope.

4.2.2 Heselbach, Black Forest, Germany

The field site at Heselbach, Germany, was initiated as a so-called supersite during the international field experiment COPS (Convectively and Orographically Induced Precipitation Study), which was a 3-month international field campaign in SW-Germany with the objective to identify the physical and chemical processes responsible for the deficiencies in quantitative precipitation forecast over low-mountain regions with the goal to improve their model representation (Wulfmeyer et al., 2008). The site was maintained as ARM Mobile Facility (AMF) by the Atmospheric Radiation Measurement (ARM) Program, which was created by the U.S. Department of Energy. The site was employed as a natural laboratory with standard meteorological and remote sensing instruments and radiometer suites. On the Heselbach site, water content was measured in a soil classified as sandy loam with a vegetational cover of grass.

Measurements were taken with (a) FDR probes (SISOMOP) installed at depths of 5 cm, 20 cm and 50 cm, (b) access tube TRIME-TDR for vertical profiling, (c) surface-based TDR with a conventional three-rod probe and (d) surface-based ERT, the latter two along a 20 m lateral transect (Table 4.1). The FDR probes provide automated continuous measurements since June 2007, while the other methods were applied on several days during Intensive Operation Periods (IOP) in June 2007, from which selected data will be presented here.

4.2.3 Dano, Burkina-Faso, West Africa

A site in the neighbourhood of the Bontioli Faunal Reserve near Bontioli (11°10' N, 03°05'W) close to Dano in Burkina Faso, West Africa was instrumented within the integrated European project African Monsoon Multidisciplinary Analyses (AMMA, www.amma-eu.org). The project was motivated by the need to develop strategies of improving forecasts of the weather and climate in the West African region (Redelsperger et al., 2006).

As a part of this experiment, measurements with TDR, FDR and GPR ground wave were conducted on a loamy sand soil according to the Soil Taxonomy (USDA, 1975). The topography of the area was mainly flat, with a vegetation cover of savannah grass with open shrubs of acacia trees. The GPR ground wave method was applied to determine the spatial variation of soil water content in the upper 0.1 m of the soil (following Sperl, 1999) along a transect of 1000 m length. An odometer wheel connected to the GPR system triggered data collection every 0.1 m. As reference measurement techniques, FDR probes were installed at 0.2 m depth, and Spatial TDR cables (see section 2.4.2) were installed vertically every 200 m along the transect. In this study, only means of the upper 0.1 m of these cables are considered.

4.3 Results

4.3.1 Full-Scale Dike Model

The homogeneity of the dike allows direct comparison between soil water content values obtained from (1) GPR and TDR within the access tube on the landside and on the waterside; or (2) the tube on the landside and the ERT measurement line perpendicular to the crest about 10 m away from the tube. From the two-dimensional resistivity tomograms, vertical profiles can be extracted for comparison.

Precipitation Event

Both TDR and GWS succeeded in retrieving soil water content before and after the precipitation (Fig. 4.3). The profiles show very good agreement with a low RMS error of 0.018 m^3/m^3. Discrepancies near the layer boundary between overburden and dike material are probably due to the different sampling volume of the two probes - while TDR samples over 18 cm (probe length), GWS reaches a much higher depth resolution of about 2.5 cm.

The two-dimensional distribution of rainfall-induced change in soil water content from ERT is shown in Fig. 4.4. The values in the organic overburden have been omitted as no saturation exponent was calibrated for this material. In the dike material, the soil water content has increased homogeneously by a factor of 2.

For the position of the access tube along the ERT line (black line in Fig. 4.4), a vertical profile of soil water content change was extracted and combined with an initial soil water content profile from TRIME-TDR. Figure 4.5 compares the resulting profile with the corresponding TRIME-TDR measurement. Both profiles agree well with an RMSE below 0.04 m^3/m^3. At greater depth the decreasing sensitivity of the surface-based ERT causes larger disagreement.

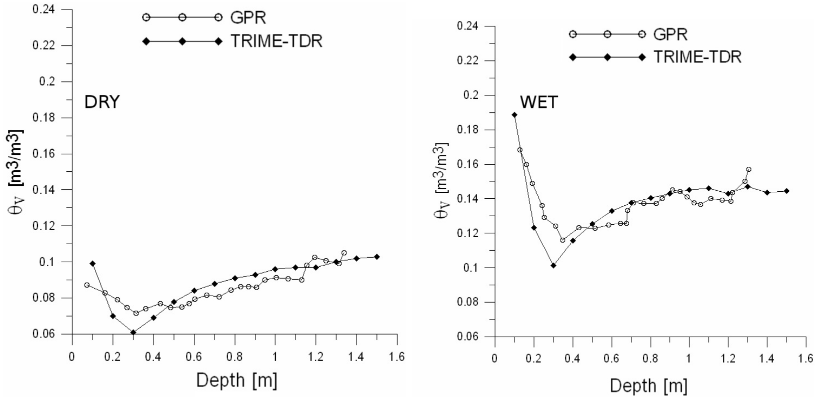

Figure 4.3: *TRIME-TDR and GWS data compared in a vertical profile before and after the rain experiment.*

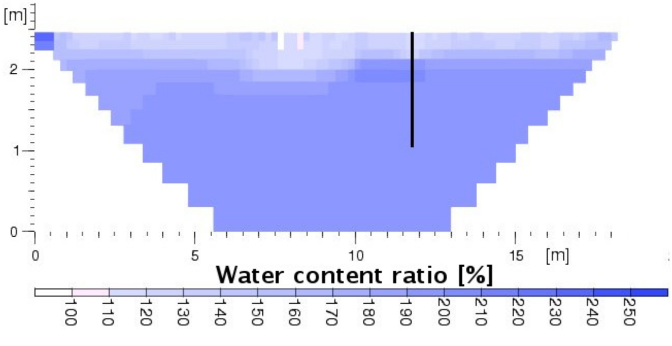

Figure 4.4: *Two-dimensional distribution of soil water content change measured for a long precipitation on the dike model, measured with ERT. The black line marks the position of the access tube.*

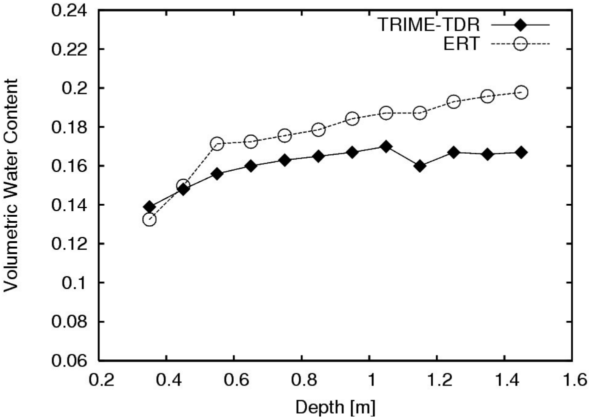

Figure 4.5: *Soil water content transect after the precipitation measured with TRIME and ERT. RMS error: 0.04* m^3/m^3.

Flooding Event

After steady state was established in the flooding experiment, ERT and GWS measurements were taken on the landside (Fig. 4.6). Near the organic overburden, ERT underestimates soil water content, but at greater depth both methods agree well. Scheuermann (2005) concluded that the maximum water content in the dike during a flood would be near 90% porosity, corresponding to 33-34% volumetric water content because of air inclusions. This agrees well with the soil water content GWS detected at greater depths and with results from the 2005 experiment (section 3.3). Within the margin of error set by the decreasing sensitivity, ERT also agrees with these results.

4.3.2 Heselbach, Black Forest, Germany

Automatically recorded time series of FDR measurements at two depths are shown in Fig. 4.7. Direct response of the sensor to precipitation is visible at shallow depth, but also at 20 cm with decreased amplitude.

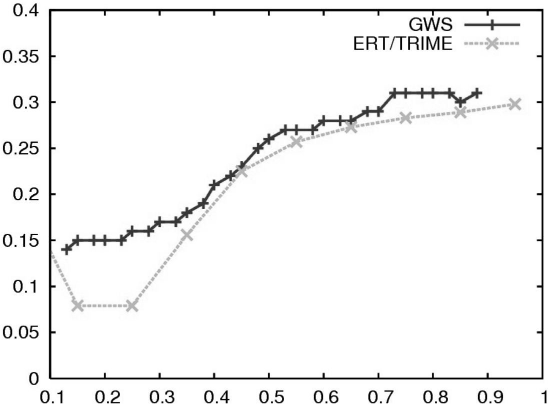

Figure 4.6: *ERT initialized with TRIME compared to GWS measurements of the soil water content during flooding on the BAW dike.*

It should be noted that the FDR data used here is not yet calibrated to water content. While preliminary calibration functions are currently being tested, they are not applied here because the arguments regarding comparability of profiles and variability of soil parameters are unaffected.

Figure 4.8a shows the FDR measurements at three depths on three different days. A lower moisture count corresponds to higher water content. From the time series (Fig. 4.7), June 13th and 20th can be expected to have approximately the same water content, and June 15th to have a higher water content as it was immediately preceded by two precipitation events. On this date, an increase in soil water content is visible for the probe at shallow depth, and the probe at 20 cm depth shows a small increase in soil water content as well. The precipitation has not affected the probe at 50 cm depth, as only the top soil layer is expected to react to rain and no major changes should occur at greater depth in the absence of preferential flow.

A second vertical profile measured with the TDR access tube probe (Fig. 4.8b) is used for comparison. The three sampling points of the FDR show qualitatively equivalent behavior compared to the TDR. As the TDR tube is at 20 m

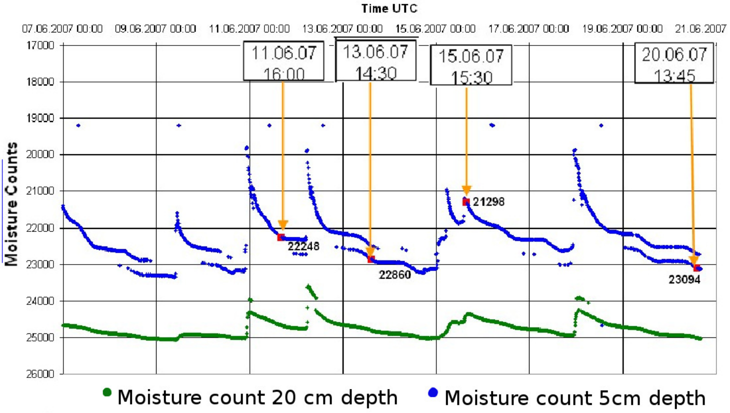

Figure 4.7: Time series of FDR measurements taken at the Heselbach site. A higher moisture count corresponds to lower soil water content. Marked are four dates where additional measurements with TDR and ERT were taken.

distance from the FDR position, it seems that the lateral variability of soil water content is small. This is further confirmed by analyzing lateral soil water content profiles obtained with surface-based TDR using a three-rod probe. Figure 4.9 shows a vertical transect extending over 20 m with a sampling width of 0.25 m. Some small-scale variability in the order of 5-10 % vol is visible. To infer whether field scale variability is present, linear profiles have been fitted. These show no trend in soil water content. Measurements taken at one position, such as the installed FDR probes, could be treated as representative for the site and could be employed for monitoring of field scale mean soil water content change.

2-dimensional ERT measurements have been taken along a measurement line coinciding with the TDR transect. For comparison of ERT to surface TDR, the resistivities of the first layer of the inverted ERT model were extracted (Fig. 4.10). Bulk resistivity shows a clear trend that could be due to different compaction or a slight change in the soil material that does not impact water content variability on the field scale. The relative changes in resistivity due to soil wa-

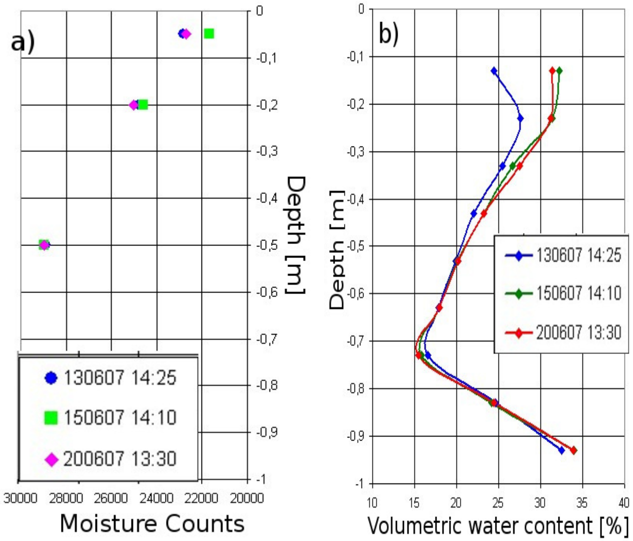

Figure 4.8: *(a) left: FDR probes at three depths for three days in June 2007 and (b) right: corresponding TDR profiles.*

ter content change stay approximately the same over the transect, representing a homogeneous change in water content, by this confirming the results from the lateral TDR transect.

Resistivity tomograms also give information at greater depth. Figure 4.11 shows measurements taken at seven time instances over the course of 8 days, and for time instances 2 through 7 the relative change in model resistivity compared to the first measurement. A two-layered structure is clearly visible in the initial model. In the deeper layer, the decreased resistivity due to infiltrating water is clearly visible, but for some patches the models show a slight increase in resistivity. The apparent increase might be caused by an inversion artifact (compare section 3.3).

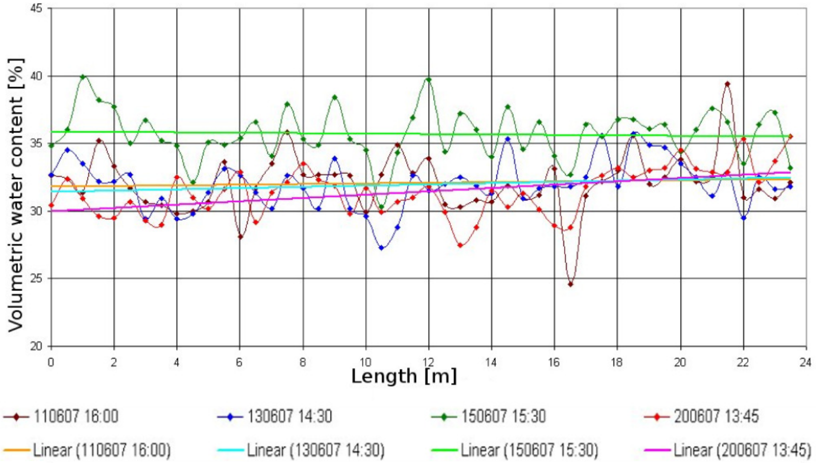

Figure 4.9: *Lateral water content measurement sampled in 0.25 m steps by TDR.*

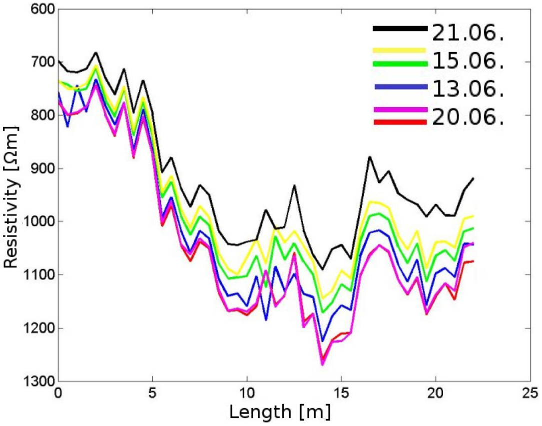

Figure 4.10: *Inverted resistivities for the top layer on different days.*

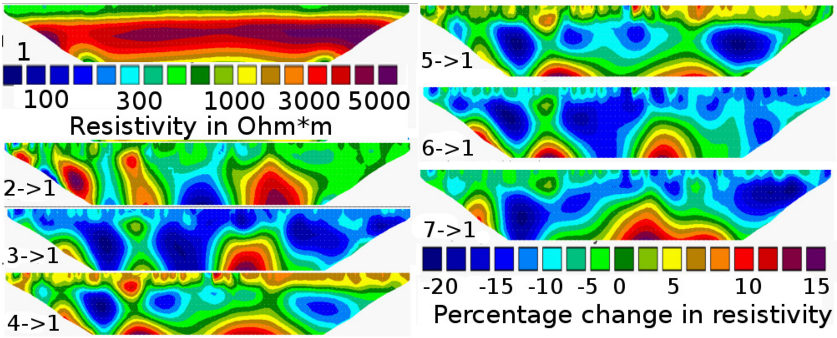

Figure 4.11: *Time steps of a timelapse inverted series of ERT tomograms at the Heselbach site. Model 1 shows the first tomogram, the further models show the percentage change of later models compared to the initial model.*

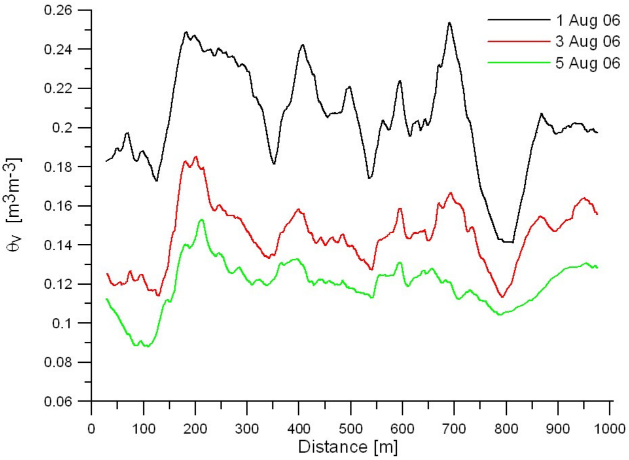

Figure 4.12: *Running means of 500 values between August 1st-5th, 2006 after antecedent precipitation on July 31st, 2006.*

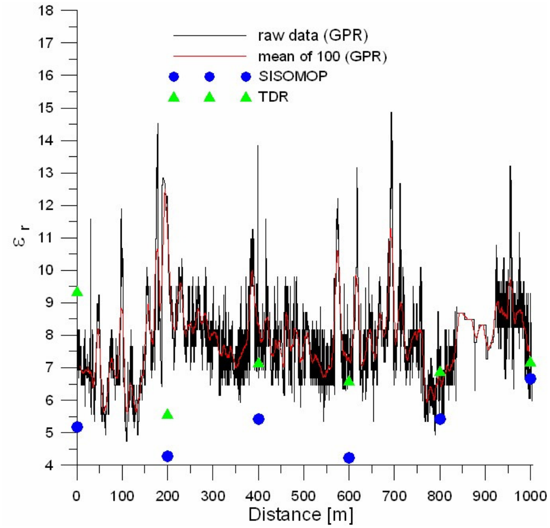

Figure 4.13: ε_r, *GPR compared to point probes for Aug. 3rd.*

4.3.3 Burkina-Faso

Figure 4.12 shows the lateral soil water content from GPR ground wave sampling. To focus on field-scale variability, the data was filtered using a running mean of 500. This way, small-scale variability connected to surface heterogeneities and varying water-holding capabilities is filtered out, but it can be seen that field-scale soil properties and soil water content show a variability structure that cannot be neglected on the field scale. Due to the flat topography of the field site, these changes can mostly be attributed to spatial variation of soil hydraulic properties. Regarding this strong variability, the information content of the pointlike probe data is questionable.

A comparison of ε_r as retrieved along the GPR profile compared to the FDR and TDR probes is shown in Figure 4.13. While the TDR probes mostly retrieve values comparable to those from GPR, the FDR probes measure much lower permittivities. A possible explanation is the larger installation depth of

FDR, where changes due to rain are much smaller because the predominant moisture change happens in the uppermost 0.1 m.

To quantify the lateral variability of water content, geostatistical methods have been applied. Preko (2008) calculated a semivariogram and fitted a spherical model (Carr, 1995), which is characterized by an increase in semivariance along a slope until a point is reached where the variance is maximum. The semivariograms (e.g. Fig. 4.14) show that the correlation length is always below 200 m (the separation of the TDR and FDR probes), so the variability along the transect can not be captured by considering only the TDR or FDR probes. The point probes would have to be installed at much closer distance to capture the soil water content variability relevant on this large field scale, an optimal separation distance would be as small as 50 m.

4.4 Discussion and Conclusions

Soil water content and its variability were evaluated on three field sites of different heterogeneity with TDR, FDR, GPR and ERT. While the first site, a full-scale dike model, was completely homogeneous, the second site in Heselbach, Germany had a heterogeneity which was low enough for discrete point measurements to be used as representative for the site. A third case study from a highly heterogeneous site in Dano, Burkina-Faso showed that projecting local discrete point measurements to field scale was not sufficient to adequately describe the lateral water content variability.

The dike site provided controllable boundary conditions and a homogeneous two-layered subsurface. Vertical profiles of water content were measured with TDR and GPR (using Guided Wave Sounding, GWS) using a tube installed vertically into the dike to retrieve the relative dielectric permittivity ε_r of the subsurface and relate it to soil water content. TDR and GWS agreed very well. Additionally, ERT was applied from the surface to measure resistivity changes related to soil water content by applying the equation by Archie (1942). All methods showed good agreement concerning absolute values and relative changes.

Under these conditions, both TRIME-TDR and GWS provided fast and adequate measurements of the soil water content along a vertical transect. Both

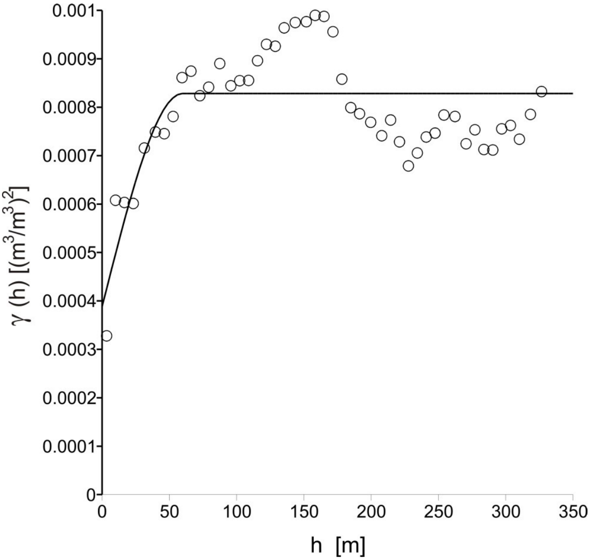

Figure 4.14: *Semivariogram for soil water content content. Solid lines represent spherical models fitted to experimental data; both for Aug. 3rd.*, reproduced from (Preko, 2008).

methods are invasive and require prior installation of a vertical access tube on the dike. ERT was calibrated (i.e. with the material parameter n, the saturation exponent) to suit the specific material properties of the site. If this material parameter, the initial soil water content profile and the necessary inversion routines are available, ERT has the advantage of being surface-based and providing two-dimensional distributions of resistivity. It would also be possible to permanently install an ERT array and automate the measurements.

For the second site, Heselbach, measurement techniques operating on different scales were compared to help define the site as homogeneous concerning soil water content changes in the upper soil. FDR probes were suitable to sample vertical water content profiles consistent with TDR profiles taken at another location. Hereby, the newly developed FDR probes (SISOMOP) are less costly than the TDR and operate autonomously. The ERT survey showed a mostly homogeneous increase in soil water content with some patterns of lower soil water content change at greater depth. In the top soil, even though the bulk resistivity showed a clear trend, the change in soil water content showed no lateral variability. The point probes would be appropriate for measuring a representative water content for the site, especially if only the water content in the top soil is of interest. To classify the variability of soil properties, a method like ERT or GPR is indispensable.

The third case study in Burkina Faso showed a field site of much larger extent, where a GPR ground wave technique was applied to estimate the lateral soil water content variability. The strong heterogeneity in soil properties could not be neglected for upscaling of soil water content. Geostatistical analysis with semivariograms showed that the correlation length of soil water content was well below the lateral separation of the employed TDR and FDR probes. The point data did not contain the lateral variability and would not be suitable for scaling the soil water content. FDR probes installed at 0.2 m depth measured considerably lower water content compared to the TDR that measured water content for the uppermost 0.1 m.

Generally, it can be concluded that the choice of methods depends on

- the application for which the data is needed: If only relative changes in surface soil water content are of interest, e.g. for 1D modeling, point probes like a FDR probe may be well sufficient. If lateral change needs to be considered, e.g. in the modeling of regional soil water content fields, methods like ERT or GPR have to be considered. In cases with low lateral variability, an investigation with ERT or GPR may identify suitable positions for point probes.

- the expected resolution: If two-dimensional distributions are needed, ERT seems the preferrable method. Vertical profiles can be obtained e.g. by access tube methods using TDR or GPR; or can be approached by multiple point probes if vertical variability is low. Lateral information of near-surface soil water content can be obtained by various methods, including TDR, ERT and GPR ground wave techniques.

- the accuracy needed: In-situ installed probes can provide better estimates, but as they have a low measurement volume, a combination of methods has to be employed and combined to get sufficiently accurate data.

- the scale of interest: Because the variability on the Heselbach site only had to be considered by a transect of 20 m length, the heterogeneity was neglectable. On the African site, a much longer transect was considered, so the scale of interest was proven to be of considerable heterogeneity. As the variability has to be included when moving through scales of soil properties (Vogel and Roth, 2003), the point probes in this study were employed not close enough to capture the variability.

5 Simulation of Water Flow

While the previous chapters have discussed a method for 2-dimensional measurements of water content, the focus will now be on the prediction of water content evolution. First, the simulation method will be introduced in a sensitivity study of the material parameters. Simulation of long-term meteorological data and a comparison of measured and simulated water content for the dike experiment (see chapter 3) is used to assess the ability to predict water content changes. Finally, two sets of weather forecasts preceding rain events on the Heselbach site during the COPS experiment (see section 4.2.2) are used to show how the prediction of water content change depends on the variability of precipitation and evapotranspiration forecasts.

5.1 Dike Model in the Simulation

A model of the full-scale dike model (section 3.1) has been created for use in a simulation of water percolation using the finite element code HYDRUS (section 2.5.3). The mesh consists of triangular elements. The grid nodes are assigned to one of three sets of material parameters: organic overburden, dike material or drain on the foot of the landside slope. Section 5.2 describes how the parameters were obtained, while the sensitivity of simulations with respect to the material parameters will be studied in section 5.3. As intial condition, a starting model with water content or pressure head values is assigned to the grid nodes. Section 5.4.2 describes different approaches how initial distributions of either type may be obtained. A simulation is driven by boundary conditions. Here, data from meteorological monitoring stations were used, namely precipitation and evapotranspiration rates (section 5.4).

5.2 Material Parameters

A description of the soil for a simulation following the van Genuchten/Mualem model requires a number of parameters:

- K_s: Hydraulic conductivity at saturation
- θ_s: Volumetric water content for fully saturated pore space
- θ_r: Residual water content for suction pressure $\rightarrow -\infty$
- α: Parameter connected with average pore size, inverse of air entry suction, $\alpha > 0$
- n: Parameter describing the width of the pore size distribution, $n > 1$
- l: Tortuosity of the flow pathways

Usually, these parameters have to be determined in laboratory measurements for each material. If laboratory data is unavailable, a numerical inversion routine, offered by the HYDRUS software (e.g. Simunek and van Genuchten, 1996) can use measured state variables or fluxes (e.g. water content or precipitation data) to estimate material parameters in an iterative approach.
For the dike model in this study, the drain was simply modeled as a very coarse material with very high hydraulic conductivity, as this part of the model has to ensure that draining of water is possible within the numerical model.
The parameters for the sand were available from laboratory data from Scheuermann (2005). As a test for cases where no laboratory data is available, a numerical inversion of the soil material parameters was carried out. A simplified model of the dike neglecting the organic overburden was created, and the flooding experiment introduced in section 3.3 was simulated by assigning a variable head condition on the waterside and raising the water level as measured in the experiment (Fig. 3.10). Along the position of a vertical Spatial TDR cable on the landside (Fig. 5.1, vertical pink line), the measured water content evolution for five representative points was prescribed. A parameter set from literature was assigned as starting parameters for the sand material. The inversion process iteratively refined the values of the material parameters so that the difference between simulated and prescribed water content was minimized. The parameters

Date	θ_r	θ_s	α	n	$K_s[m/min]$
Sand (Inversion)	0.045	0.348	3.31	4.11	0.00714
Sand (Laboratory)	0.045	0.361	4	2.2	0.0124
Organic Overburden	0.067	0.45	5.23	2.67	$1.572 \cdot 10^{-4}$
Drain	0.045	0.43	15	2.68	0.495

Table 5.1: *Material parameters for the BAW dike model*

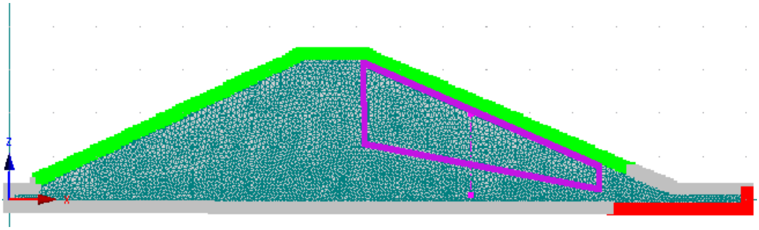

Figure 5.1: *Finite element model for the simulation. Marked are the atmospheric boundary (green), the draining boundary (red), the no-flow boundary (grey) and the position of a Spatial TDR cable (vertical pink line). The averaging area for the comparison of measured and simulated data is marked with a thick violet border.*

obtained this way are shown in table 5.2. Both parameter sets for the sand agree well, so in cases where no laboratory data are available, the inversion method can provide estimates of the material parameters.

For the overburden material parameters, no laboratory data and no direct water content measurements were available. Therefore, water content measurements within the sand layer, but at a position directly below the organic overburden, were used in an inversion. A flat two layer model was used to simulate a rainfall event presented by Scheuermann (2005). The sand parameters were kept constant and the parameters of the organic overburden were successfully inverted. The resulting parameters of the overburden and of the drain are also shown in table 5.2.

5.3 Influence of material parameters on the simulation

This section discusses a series of test simulations performed as sensitivity studies regarding the van Genuchten-parameters (see 2.5.2). Again, the flooding experiment at the BAW dike was simulated (see section 3.3 and Fig. 3.10). In each simulation, all but one soil parameter in the sand were kept constant, the variable parameter was changed in logarithmic steps. The corresponding diagrams will show the evolution of volumetric water content during the flooding, averaged along a vertical transect at the position of a Spatial TDR-cable near the center of the landside of the actual dike model (Fig. 5.1, vertical pink line). The initial water content within the dike was set to 0.08 at the top and 0.11 near the bottom of the dike with a linear interpolation in between. The initial water content within the organic overburden was set to 0.18.

The sensitivity to the hydraulic conductivity K_s is shown in figure 5.2. The parameter was varied in logarithmic steps between 0.1 m/min and 0.0001 m/min. The maximum of water content at first increases with decreasing K_s, but ultimately decreases again. For low conductivities, water cannot infiltrate fast enough into the dike compared to the duration of the flooding. Maximum water contents are reached for an intermediate hydraulic conductivity of $K_s = 0.001$ m/min. The influence of K_s is also visible in the phase of drying: The water content decreases more slowly for low hydraulic conductivity, while a high conductivity will lead to fast draining.

Next, the parameter α was varied in powers of 2 between 2 and 32. For the sand of the real dike model, values of $\alpha \approx 4$ are realistic. Figure 5.3 shows the resulting water content variation. A slight shift of the maximum towards later times is visible for decreasing α. More importantly, the volumetric water content is higher for lower α.

The effect of hysteresis (see 2.5.3) is shown in fig. 5.4 using the assumption $\alpha_d = 2 \cdot \alpha_w$, where the subscripts d and w indicate the draining or wetting branch of the hysteresis curve, respectively. Simulation results are compared for two values of α with and without hysteresis. The influence of a higher α_d becomes apparent during the draining phase. To understand why a larger α_d causes slower draining, assume a system in which a large pore is only accessible via small capillaries. Before the large pore can be drained, the small capillaries

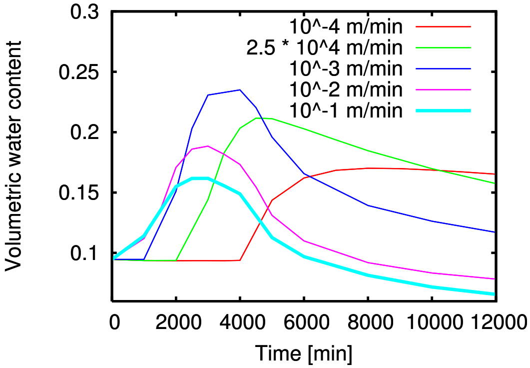

Figure 5.2: *Volumetric water content averaged along a vertical transection for a flooding simulation and variations in saturated hydraulic conductivity K_s.*

have to be drained first, which requires a larger hydraulic head.

Figure 5.5 shows the results of variations in n. For smaller n, a higher maximum water content is reached, and the drainage is much slower. The width of the pore size distribution is parameterized by $1/n$, so for smaller n, pores much smaller and much bigger than the average exist. During draining, the smaller capillaries effectively block pores behind them until they become drained, causing slower draining compared to simulations with larger n. During wetting, there will be larger pores available that will fill fast and allow a higher water content maximum.

Finally, Figure 5.6 shows that variations in tortuosity l have no significant influence on the wetting or draining process. Only during draining, a smaller tortuosity will allow a slightly faster draining, because the flow paths are less tortuous.

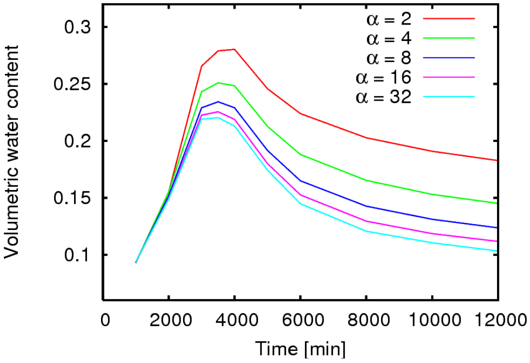

Figure 5.3: *Volumetric water content averaged along a vertical transection for a flooding simulation and variations in* α*.*

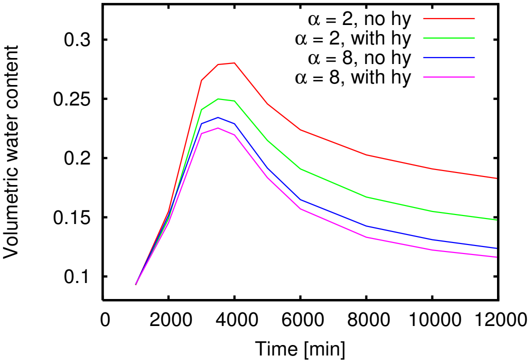

Figure 5.4: *Volumetric water content averaged along a vertical transection for a flooding simulation and variations in* α*, with or without hysteresis.*

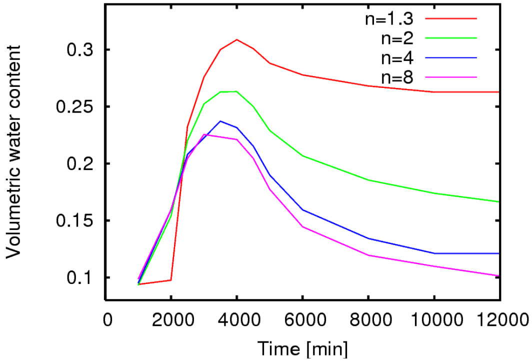

Figure 5.5: *Volumetric water content averaged along a vertical transection for a flooding simulation and variations in n.*

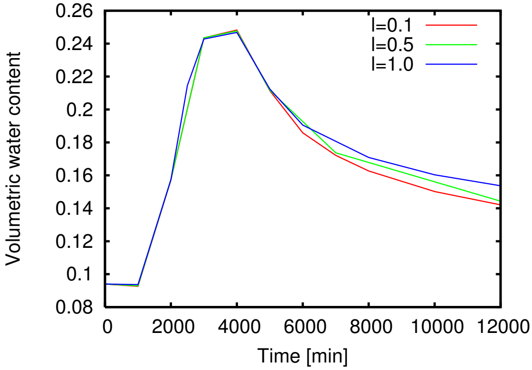

Figure 5.6: *Volumetric water content averaged along a vertical transection for a flooding simulation and variations in tortuosity l.*

5.4 Meteorological Scenarios

Besides the special case of a boundary condition representing a flood, the boundary conditions forcing the water content movement in the simulation are precipitation and evapotranspiration. Evapotranspiration and precipitation rates are assumed to be constant over a certain time interval, here intervals of hours or days are used. For the model spin-up which aims at determining an appropriate initial distribution of water content (or pressure head) for the simulation, daily values are sufficient, while for simulations of meteorological scenarios hourly values are used.

5.4.1 Evapotranspiration Time Series

While precipitation data can be directly recorded, evapotranspiration has to be calculated from measured meteorological quantities. During the experiments on the BAW dike, an energy balance station was set up next to the dike. The components measured by this station were:

- Precipitation rate
- Shortwave and longwave radiation balance
- Soil temperature in 2, 4, 8, 16, 32 and 64 cm depth
- Relative humidity, air pressure and temperature (in two heights)
- Wind speed and direction
- Soil heat flux

The local evapotranspiration was calculated using the Bowen ratio formulation (Eq. 2.6) as hourly rates.

For comparison and for simulations of longer time periods where energy balance data were not available, data from the meteorological station Karlsruhe-Nordwest [2] were used and daily rates of evapotranspiration were computed using the Penman formulation as described in section 2.1.

For the BAW experiment in 2005, daily evapotranspiration rates obtained from both methods are compared in Fig. 5.7. Both methods agree very well for all days except August 3rd, where the values differ significantly. To understand this, it was analyzed whether a building in immediate vicinity northwest of the BAW station might be the cause of this discrepancy by decreasing the observed

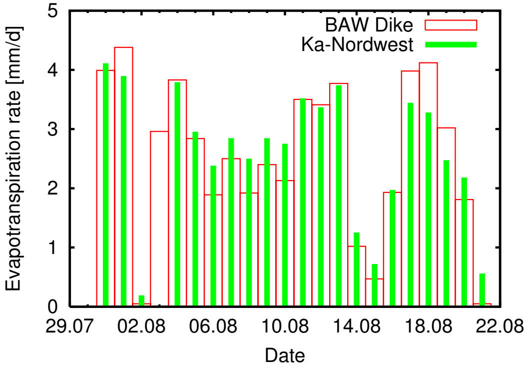

Figure 5.7: *Comparison of daily evapotranspiration rates obtained from the meteorological station Karlsruhe-Nordwest (green lines) and the energy balance station near the dike (red blocks).*

wind velocity values for northwesterly flow directions. Figure 5.8 shows a comparison of the wind directions for both stations. Disregarding the fact that wind velocities are generally higher at the Karlsruhe-Nordwest station (the wind is measured at a height of 5 m, compared to 2 m at the BAW station), both diagrams show a similar distribution of flow except for virtually absent wind directions from the northwest for the BAW station. This can only be explained by shadowing effects from the building northwest of the station. To determine on which dates wind from NW was shadowed, the wind direction was plotted over time (Fig. 5.9). Dates with NW wind are few, but include August 3rd, where the calculated evapotranspiration values differed widely between the stations.

5.4.2 Initial conditions

There are different ways to generate an initial water content distributions for the model simulations (see e.g. Rodell et al., 2005). In this study, three meth-

---

[2] Data provided by the Landesanstalt für Umwelt, Messungen und Naturschutz Baden-Württemberg

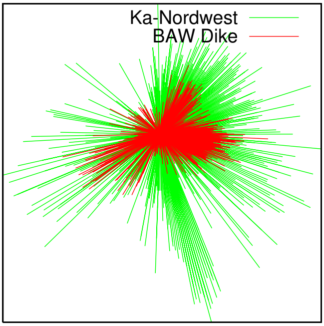

Figure 5.8: *Comparison of wind directions for the energy balance station near the dike (green) and the meteorological station (red). Each line represents an hourly average of wind direction with the line length corresponding to the average wind velocity.*

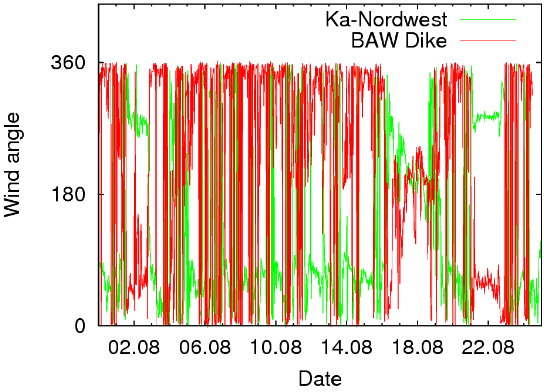

Figure 5.9: *Comparison of wind directions over time for the energy balance station near the dike (green) and the meteorological station (red)*

ods have been tested: The first one is to simply start with a completely dry/wet model (or one at field capacity). This has the disadvantage of a long period with erroneous water contents until the current water content is no longer correlated to the starting value. The second method is to prescribe a measured water content distribution. This should be the best approach, but of course demands a measured water content distribution at the time the simulation starts. The third and most commonly used way is to use meteorological forcing data to run a model spin-up with coarser time resolution (daily rates). The final distribution of water content or pressure head of this spin-up is used as an initial distribution for the simulation. The model spin-up starts with a completely dry model, and its duration must be chosen in a way that the final water content distribution is no longer correlated to the starting distribution. For the 5 year simulated period described in the next section, the autocovariance of the averaged water content in the model was analyzed. Figure 5.10 shows how two water content averages taken Δt days apart are correlated. Disregarding the seasonal variations, a spin-up time of 6 months should ensure that the water content distribution is no longer correlated to the (dry) starting state. Three months length should already provide an acceptable estimate. These correlation lengths are specific to the dike modeled in this study and could be different for different models and different materials, although it seems reasonable that 6 months provide a sufficiently long period in most cases.

5.5 Simulation of 5 years

A complete data set from the meteorological station Karlsruhe-Nordwest was available[2] for the years 2001-2005. Figure 5.1 shows the general setup of the finite-element model used for the simulation. The atmospheric boundary (green) ensures the interaction of soil with the atmosphere, and the drainage boundary (red) simulates the drain where water can leave the dike model. Because the water-proof sealing underneath the dike allows no water to leave, a no-flow boundary condition (grey) was used.

The result of the simulation is displayed in Figure 5.11 as evolution of the average water content in the sand material. The organic overburden was omitted for this figure as the different soil water characteristics lead to different satu-

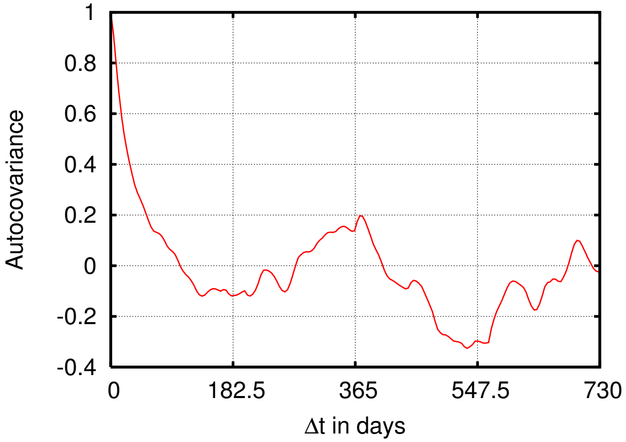

Figure 5.10: *Autocovariance of the averaged water content for the 5 year simulation (section 5.5).*

ration compared to the sand. The figure also shows the boundary conditions, precipitation rate in green and evapotranspiration in blue. The annual variation in evapotranspiration with daily rates of up to 5 mm/d in summer and very little evapotranspiration during the winter months are clearly visible.

The simulation started in completely dry state, so the first three months of the simulation must be regarded as the phase during which the water content initially increases. After that, the average saturation within the dike shows immediate responses to precipitation events, and desaturation through evaporation and drainage after these events proceeds in a matter of weeks or even days. For time periods with a larger number of precipitation events in short intervals, the saturation stays at a higher value for a longer time. The saturation falls below 9 % after longer dry periods, can reach above 13 % immediately after rain events, and varies around 11 % for periods of multiple precipitation events. Overall, the simulation results in comparatively low variability of saturation, due to the high hydraulic conductivity of the sand material causing fast draining after precipitation events, and a low water retention capability that makes it unlikely

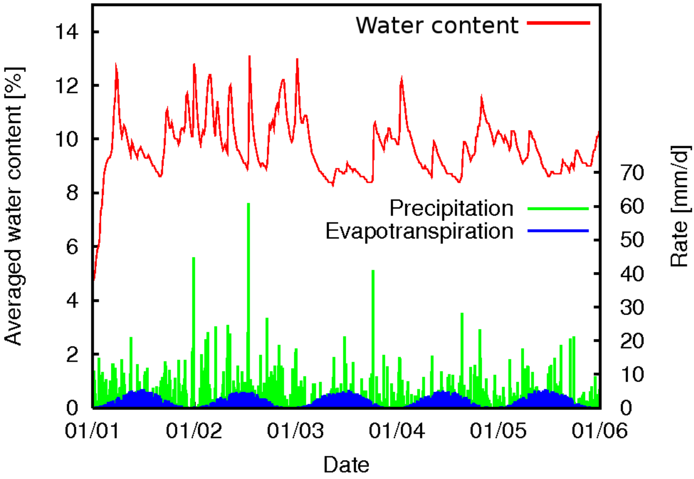

Figure 5.11: *Simulated water content for 5 years, averaged for the dike material.*

that higher water contents over the course of multiple precipitation events are reached. This agreese well with measurement results (see Fig. 4.3, where an extensive rainfall induced a change in water content from approximately 8-10 % to 13-14 %. A previous short rainfall experiment induced no water content increase in the dike body (section 3.3).

The middle year in the simulation, 2003, is notorious for being one of the hottest and dryest summers in history in Germany and Central Europe (Schaer and Jendritzky, 2004). This is clearly visible in Figure 5.11. The water content stayed below 9 % all summer.

5.6 Simulation of 2005 experiment

A simulation of the experimental phase at the BAW dike in 2005 allows answers to the question whether a simulation of water content movement can be used to predict the water content evolution, e.g. by using precipitation and evap-

otranspiration data from numerical predicition models to estimate future water content.
The determination of boundary and inital conditions was already described in previous sections. As measurements of the water content for the whole simulation period are available (see chapter 3), both observation and model results can be compared if an area for averaging is defined that takes into account the different volumes. As ERT has the smallest investigation volume with a penetration depth of roughly 1/6 of the length of the measurement line and is restricted to the landside, a volume was chosen equal to the part of the sand covered by ERT surveys. This area is marked with a violet border in Figure 5.1.
Modeled and observed volumetric water content are compared in Fig. 5.12. As ERT has been calibrated by an initial water content from Spatial TDR (marked in the figure), the lines agree very well, but ERT shows stronger reactions to changes in water content, which is connected to the influence of artifacts (see chapter 3) and the sensitivity to small errors in the saturation exponent. This leads to a good agreement near the calibration point, but to unphysically low water content at the beginning of the experiment, before the strong rainfall. Both the simulated and ERT-measured curve agree well in their shape and the reaction to the strong precipitation event. The simulated water contents, however, are much higher, which may be connected to the fact that the simulation operates in the Richards regime, which neglects effects like e.g. air inclusions that appear near saturation.

5.7 Predicting Water Content Evolution

In previous sections, it was shown that numerical simulations of water content movement in soils can be used to estimate the water content evolution. In this chapter, we will further assess the potential for their application to forecast data. Forecast data has been taken from the COSMO-EM (formerly LME) model of the German Weather Service (DWD) for selected sites during the COPS experiment phase (see section 4.2.2). COPS was linked to other research programs, among them DPHASE (Demonstration of Probabilistic Hydrological and Atmospheric Simulation of flood Events in the Alpine region), which includes model runs of various numerical weather prediction models, including the operational forecast model COSMO-EM.

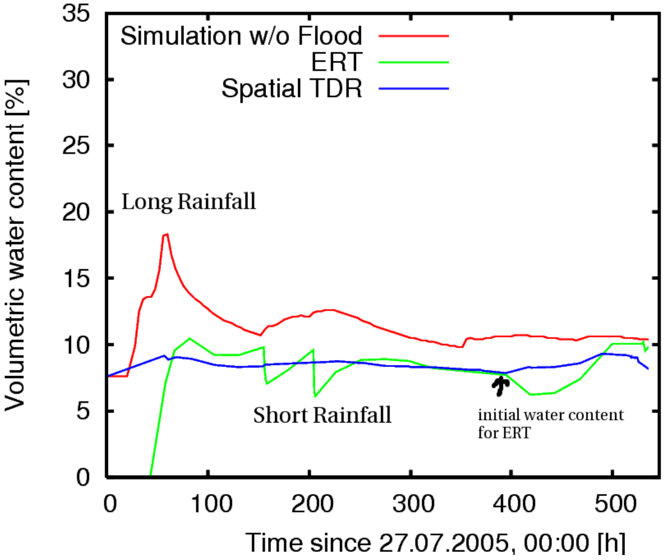

Figure 5.12: *Volumetric water content averaged in the area marked in Fig. 5.1 for simulated water content, ERT and Spatial TDR.*

COSMO-EM (Steppeler et al., 2003; Schulz, 2005) was developed by the German Weather Service (DWD). It runs with a horizontal resolution of 7 km and has 40 vertical layers. The model runs used here operate on a domain covering latitudes from 43°N to 50°N and longitudes from 2°E to 18°E. The soil model TERRA comprises of 8 layers with depths from 0-1 cm, 1-3 cm, 3-9 cm, 9-27 cm, 27-81 cm for the topmost layers. For the duration of the COPS experiment, COSMO-EM model runs were started every 6 hours.

Here, forecasts for two distinct precipitation events in June 2007 were used. From the forecast data provided by the DWD, the grid point nearest to the Heselbach site (Fig. 5.13) was chosen and time series of precipitation and evapotranspiration were determined. The evapotranspiration was computed from the latent heat flux data available from COSMO-EM.

A simplified model of the soil structure at the Heselbach site was created and

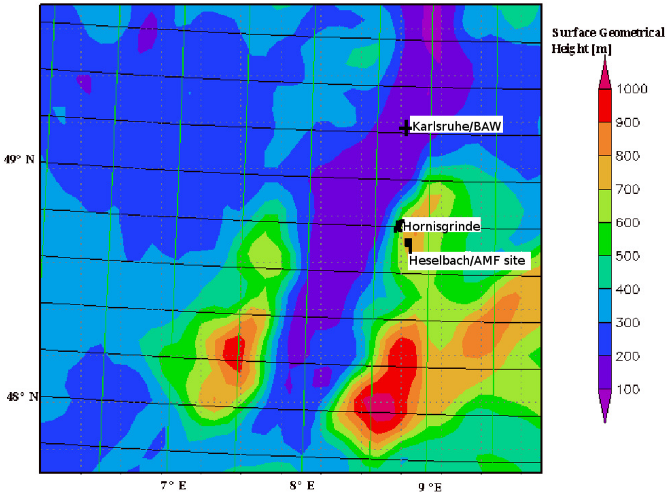

Figure 5.13: *Domain of the COPS experiment, surface geometrical height and the three sites BAW, Heselbach and Hornisgrinde*

the time series simulated for forecast runs started approximately 48, 36, 24 and 12 hours before the precipitation event. The observed precipitation data at the Heselbach site can be seen in Fig. 5.14.[3]

In HYDRUS, precipitation and evapotranspiration data from the forecast model runs was used to simulate the soil water content evolution. Averaged for shallow depths between 3 cm and 9 cm (corresponding to the third soil layer in COSMO-EM), the predicted water content is shown in Fig. 5.15 compared to a simulation forced by measured precipitation data. For the forecasts of the precipitation event on June 16th, the simulation started on the 14th, 00:00 and predicted a change in water content close to the control simulation predictions that simulated the observed precipitation data, but the timing of the precipita-

---

[3] Data were obtained from the Atmospheric Radiation Measurement (ARM) Program sponsored by the U.S. Department of Energy, Office of Science, Office of Biological and Environmental Research, Environmental Sciences Division.

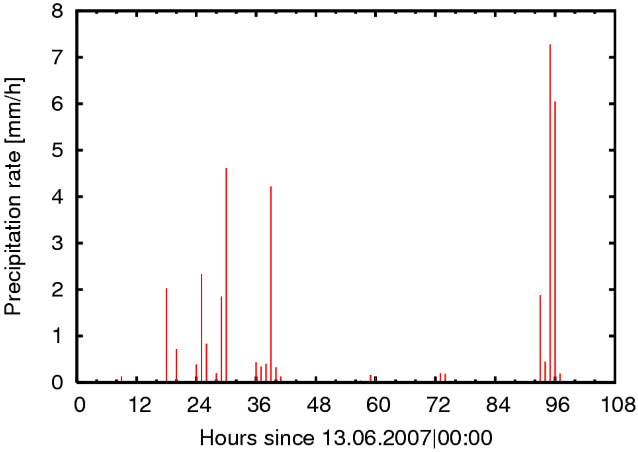

Figure 5.14: *Measured precipitation data for the Heselbach site between 13.06.2007 and 18.06.2007*[3].

tion is delayed by 5 hours. The run started 12 hours later predicts an increase in water content at the correct time, but with much lower amplitude than the control run. The other runs hardly predicted an increase in water content at all. However, looking at shallow depths (1 cm to 3 cm; Fig. 5.16), a small increase in water content was modeled at approximately the right time. From this figure, it also becomes apparent that the measured precipitation data showed two peaks (cf. Figure 5.14), while the best prediction from June 14th, 00:00, shows only one peak, approximately in the middle between the observed maxima.

The second example, predicting a precipitation event on June 18th, shows a similar result. One forecast correctly predicted the amount of change, with good timing. All other runs largely underestimated the amount of precipitation, but got the timing correct as well. Overall, the forecasts seem to be able to predict the trend, but not the amount of rain. There are, however, some model runs that also manage to predict the correct amount of precipitation and thereby the amplitude of the soil water response.

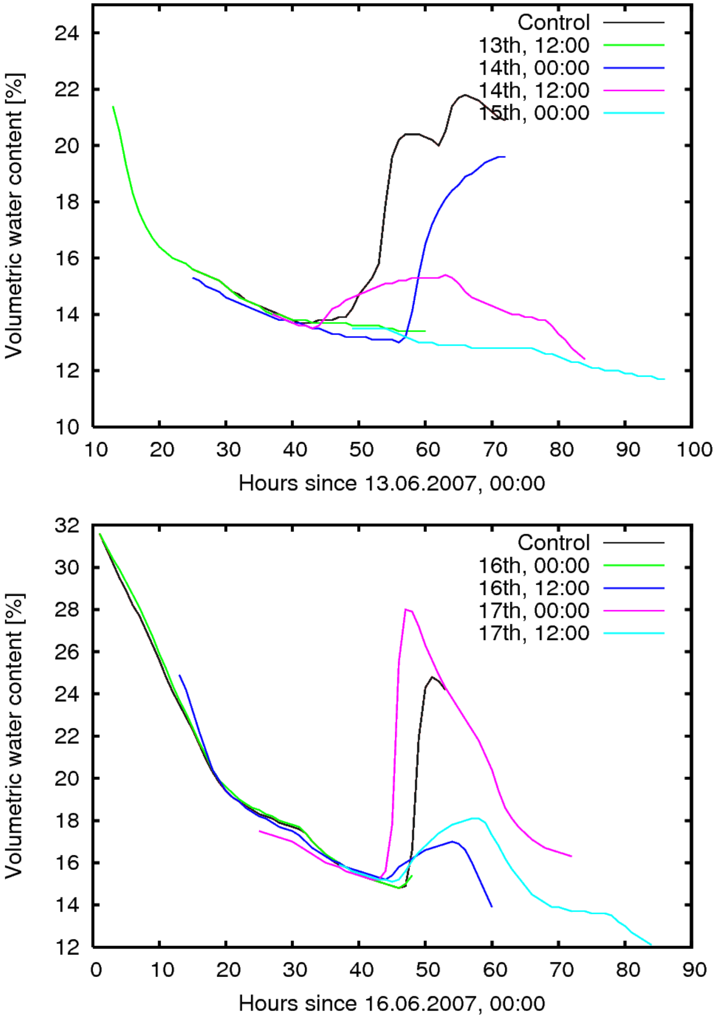

Figure 5.15: *Water content simulation based on COSMO-EM forecasts and a control run forced by observed precipitation data for a model of the Heselbach site at 3 cm to 9 cm depth. Forecast model runs started approximately 48, 36, 24 and 12 hours before precipitation events on Upper: 14.06.2007 and Lower: 18.06.2007.*

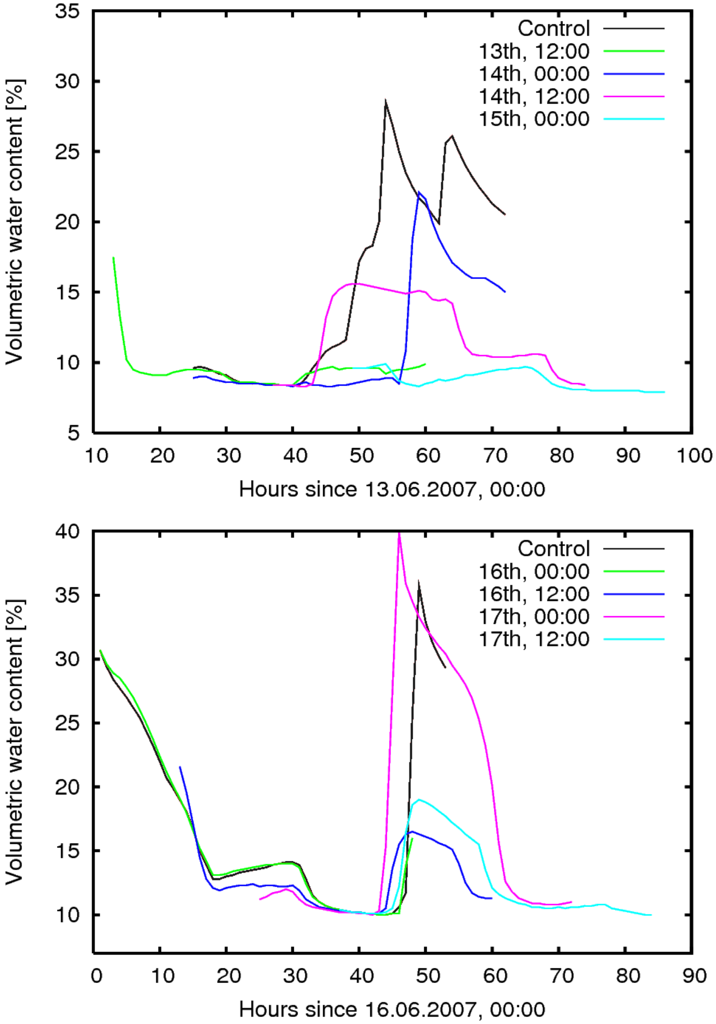

Figure 5.16: *Water content simulation based on COSMO-EM forecasts and a control run forced by observed precipation data for a model of the Heselbach site at* 1 *cm to* 3 *cm depth. Forecast model runs started approximately 48, 36, 24 and 12 hours before precipitation events on Upper: 14.06.2007 and Lower: 18.06.2007.*

5.8 Discussion and Conclusions

In this chapter, numerical modeling of water flow in the subsurface was tested as a means to predict water content evolution. The material parameters for the simulated dike model were obtained from laboratory measurements and a numerical inversion routine. The inversion iteratively minimizes the difference between modeled and prescribed water content distributions from measurements. A soil parameter set can thus be obtained in cases where no laboratory data is available.

The water flow in the near-surface soil is forced by the boundary conditions of precipitation and evapotranspiration. A comparison of two methods (Bowen ratio and Penman method) to compute evapotranspiration rates for two stations in northwest Karlsruhe showed very good agreement. This allows the conclusion that if no field data of evapotranspiration is available, nearby meteorological station data may provide suitable estimates. Large discrepancies in the precipitation rates for one measurement day were explained by a building adjacent to the dike station that shadows wind with NW directions. To obtain suitable initial conditions of water content, measured values from field surveys or a 3 to 6 months model spin-up can be used.

To evaluate the annual variability in mean soil water content, long-term simulations of precipitation and evapotranspiration data were used. In this study, a 5 year simulation characterized the BAW model dike as having a low variability in water content that is caused by the high hydraulic conductivity of the dike material. A simulation of the BAW experiment from 2005 allowed a comparison of simulated and measured water content. While the absolute values differed, the trends in water content evolution could be simulated. As the simulation operates in the Richards regime, a correct quantification of water processes near saturation can not be expected.

The prediction of water content evolution was further analyzed by using precipitation and evapotranspiration data forecasts for two precipitation events during the COPS field campaign. Each precipitation event was predicted by four forecasts starting 12 to 48 hours before the event. Overall, the timing of the precipitation events was mostly correct, but the predicted amount was underestimated for most forecasts. The prediction of water content largely depends on the quality of the precipitation forecasts. Each forecast may predict convective cells differing in initialization, extent and direction of movement, so that from a viewpoint of a discrete field site, quite different precipitation rates may occur. Especially for convective precipitation, the smaller extent of the cells and difficulties in predicting the correct area of initialization of these cells may lead to increased difficulties in forecasting correct precipitation fields (see e.g. Meissner et al., 2007; Wulfmeyer et al., 2008).

6 Reliability of resistivity quantification

Previous chapters have introduced ERT as a method to monitor water content and numerical modeling of water flow as a means to predict water content evolution. Integrating both approaches, the reliability of ERT to quantify water content was analyzed.

Even when the petrophysical relation between resistivity and water content is known, the resistivity models are non-unique and have likely been affected by the inversion process. The sensitivity of tomographic surveys plays a major role in the retrieval of subsurface characteristics, e.g. for surface-based ERT the sensitivity decreases with depth. Low sensitivity areas (but not only those) can often be plagued by inversion artifacts (see section 3.3). The inversion process and the choice of inversion parameters, e.g. the regularization parameters, determine how well the inverted model will reproduce the real distribution. However, some of the parameter choices can not reliably be based upon observation, but must be fitted or depend on experience.

To assess the quality of ERT-based water content quantification, the complete processing chain including the inversion process, the petrophysical relation and numerical simulations of the soil water movement, has to be evaluated. This chapter introduces a combined approach using soil hydraulic simulations and ensemble building of inverted models to estimate the uncertainty inherent in typical applications of ERT for water content quantification.

To evaluate the inversion process, a forward-inverse cycle approach is presented. Forward modeling routines have been introduced in section 3.3 and are here applied to synthetic data sets obtained from simulations of soil water movement. For two cases studies, the approach is used to discuss how slight variations in the soil structure influence the resistivity retrieval, and thereby the water content retrieval.

Secondly, an ensemble approach is presented which allows an overview of the possible range of inverted models, enabling general assertions about how well a given model can be characterized through the chosen inversion process.

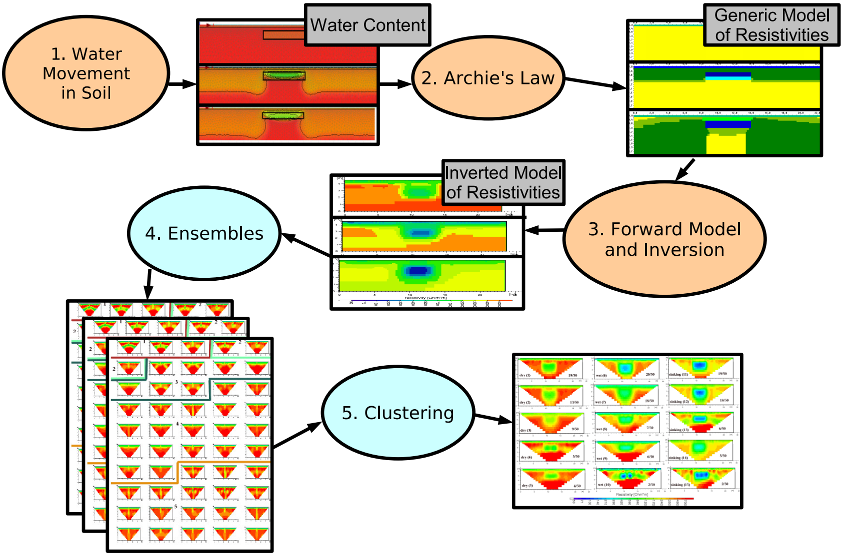

Figure 6.1: *Chart visualizing the steps involved in this study.*

6.1 Methods

The two methods implemented in this study are divided into five steps (Fig. 6.1). In the first part, the forward-inverse cycles (orange boxes in Figure 6.1), the ability of the inversion scheme to reproduce a given data set is analyzed. In the next steps (blue boxes), the ensemble approach is introduced.
In the following, each step of the model will be shortly introduced. Further discussion will illustrate how the steps can be applied using two synthetic data sets.

1. A simple model of a soil structure is build as a finite-element model for a numeric simulation of water movement. The movement of a water front, caused by rainfall infiltrating at the soil surface, is simulated over time. Characteristic time steps are identified and a simplified distribution of water content is arranged. The first time step should be the one for a

completely dry soil. In the following, the models for the various time steps are identified by their wetting state.

2. A generic model of resistivity mirroring the soil structure from (1.) is created.
    - For a model representing a dry state (no water content), resistivities are assigned based on typical values known from experience and literature.
    - For states of wetting, changes in water content can be calculated using the water content distribution from (1.). They can be transferred into resistivity changes by applying Archie's equation (1942).
    - A finite-element based forward modeling routine transfers the generic models into model responses (sets of apparent resistivities) that would have been recorded by field surveys. Random noise is added to simulate field conditions.
3. The apparent resistivities are inverted using a suitable inversion scheme. By way of comparison, the retrieved and the expected resistivity distributions can be evaluated.
4. For each data set, an ensemble of 50 different inverted models is created. A different model is obtained by varying the inversion parameters or the inversion scheme. The parameter set shall be chosen randomly from a parameter space that is constrained to meaningful parameter sets, but wide enough to allow unlikely, but possible models.
5. A clustering algorithm is used to group similar models of the ensemble. Cluster members can be averaged to simplify the analysis of the ensemble.

6.1.1 Application to synthetic data sets

The application of this methodology was governed by the available software codes for modeling and inversion. This section discusses how the steps were specifically realized for application on two synthetic data sets.

Step 1: Numerical simulation of water movement

A numerical simulation of water movement was used to ensure that realistic distributions of water content (and thus resistivity) were used. The hydrologic simulations were performed using the HYDRUS software (Simunek et al., 2006) as described in the previous chapter. By defining time-variable precipitation and evaporation rates as atmospheric boundary conditions, changes in the hydraulic head h_m and thus water movement are induced. Meteorological data from the permanent station Karlsruhe-Nordwest (Germany) were used as forcing. The Penman formula (2.7), calibrated for grass cover by Doorenbos and Pruitt (1977), was applied to these data to retrieve values for potential evapotranspiration (ETO). Combined with measured precipitation rates, these values wer used as daily averages for simulations of 210 days based on measurements in 2001.

The simulations were conducted with models representing a two-layered soil. In addition to the atmospheric boundary, a seepage boundary on the bottom allowed water to leave the domain. From the simulations, characteristic states of a water front infiltrating the domain were identified.

Step 2: Generic model of resistivities

The transfer from water saturation values S to electrical resistivity ρ is given by the equations of Archie (1942) as described in section 2.3.4 and chapter 3.

A generic model of resistivities was modeled with random noise of 3% to calculate the response (measurement data) an actual ERT survey would have retrieved.

Step 3: Inversion of apparent resistivities

The first part of the method is completed by inverting this simulated measurement data. The generic model and the forward-inverse modeled data set can then be compared and interpreted.

The inversion method of choice is the robust inversion scheme (see section 2.3.3).

Constraint on the data	Robust or Smooth
Constraint on the model	Robust or Smooth
Initial damping λ_i	0.01 to 1
Minimal damping λ_m	$0.05\lambda_i$ to $0.2\lambda_i$
Convergence Limit	1% to 9%
Maximal number of iterations	3, 5 or 15
Vertical to horizontal regularization	0.25 to 4
Increase of Damping with depth	1.0 to 2.0
Reduce effect of Side Blocks	None, Slight, Severe, Very Severe
Higher Damping for first layer	Yes or no

Table 6.1: *Parameter space of inversion parameters used for ensemble calculations.*

Step 4: Building Ensembles

Inversion problems for geoelectrical surveys usually are ill-posed, mixed determined problems. If the errors in data acquisition and in the inversion process would be known quantitatively, the optimum model and its error distribution could be determined exactly. Measurement errors often can only be estimated, and further discrepancies may be introduced during inversion, especially if an inversion code is used that does not rigorously optimize for a given error estimate. Additionally, inverted models can be plagued by possibly large inversion artifacts depending e.g. on resistivity contrasts. Consequently, it might not be sufficient to analyze only the optimum model (i.e. the model with the smallest data misfit), but to compute a range of possible models addressing the inherent variability of the inversion process. By randomly varying the inversion parameter set and creating an ensemble of possible inversion models, the whole parameter space and thus the possible model range is explored.

For the RES2DINV code used here, the range of parameters is listed in table 6.1. It encompasses the use of smoothness constrained and robust inversions as well as two mixed formulations with a robust constraint applied on the data only, and one with a robust constraint applied on the model only. Further varia-

tions mostly concern the regularization, e.g. the damping factor, where an initial damping factor λ_{start} and the maximum damping factor λ_{max} are adjusted. For most variations, the maximum damping factor λ_{max} is kept at $\lambda_{max} = 10 \cdot \lambda_{start}$. Additional variations are possible in the reduction of side block effects, the ratio of vertical to horizontal smoothness filtering and the use of the first iteration step model as a reference model for the further iterations instead of using the average of resistivities.
It should be noted that this choice of variations is specific for the software that was used here. However, the idea can easily be transferred to similar inversion approaches.
Almost all inversions resulted in inverted models with RMS errors smaller than 4% as can be expected from adding 3% artifical noise to the data set. Some single inversions, however, resulted in a larger RMS error. In section 6.2, both inversion models with RMS $\leq 4\%$ and $> 4\%$ will be included to keep the ensembles balanced.

Step 5: Clustering

Each ensemble is created as a cloud of different models and then are clustered using a *k*-means clustering algorithm. This clustering method starts with a collection of 'genes', here a gene is a row of all block resistivities of one model. The distance between two genes is calculated as a Pearson correlation

$$\frac{1}{n}\sum\left(\frac{x_i-\overline{x}}{\sigma_x}\right)\left(\frac{y_i-\overline{y}}{\sigma_y}\right) \tag{6.1}$$

where $\overline{x}$ is the average of values in gene x and σ_x is the standard deviation of these values. The k-means clustering starts with a user decision on the number of clusters to be created, then randomly assigns each gene to a cluster. For each cluster, the average model is created, then each gene is assigned to the cluster it has the smallest distance from. These last steps are repeated until an optimal solution is found. At least two runs creating the same optimal solution are needed to reach a reliable solution.

6.2 Synthetic case studies

All test cases studied here are based on a simple two layer medium representing the structure of a full-scale dike model described in detail in chapter 3. Although synthetic data sets are employed to distinctively focus on specific anomalies, the material parameters were obtained from real observation as described in the previous chapter.

Based on this two layer medium, two generic cases representing different idealized case studies were created: The first case study simulates a defective sealing, where an infiltration plume of water is generated in the sand layer. In the second case study, a rectangular, hydraulically resistive anomaly is placed in the sand underneath the organic overburden.

6.2.1 First Case: Defective Sealing

The first case is based on the idea of a crack in a dike sealing. Damaged sealings are critical, as even through small cracks, large amounts of water can infiltrate. In this hypothetical case, water infiltrates through a otherwise sealed off surface through one crack. For this study, the sealing is considered to be invisible to the geoelectrical survey.

Water Simulation

In HYDRUS, the sealing is modeled as a no-flow boundary, and the crack has an atmospheric boundary and is filled with sand material. The simulation results show water infiltrating through the crack into the sand where it diffuses into a sinking plume. The water content does not change outside of the plume (Fig. 6.2). Three characteristic states of the simulated results can be identified: dry state (Fig. 6.2a), infiltration state (the plume begins to form in the sand, Fig. 6.2b) and the diffusion state (Fig. 6.2c), where the center of the plume has propagated into the sand and the top layer is already drying. The transfer from water content to resistivities was done by assuming a dry state resistivity of $\rho = 400\ \Omega m$ for the overburden and $\rho = 5000\ \Omega m$ for the sand and applying Eq. 2.19 with saturation exponent $n = 2$ for the overburden and $n = 1.16$ for the sand as determined in section 3.3. During infiltration and diffusion, this results in a minimal resistivity in the plume of $\rho = 2000\ \Omega m$.

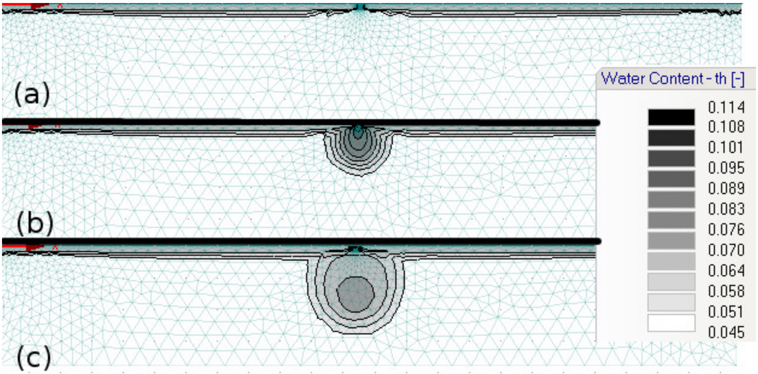

Figure 6.2: *Defective sealing, characteristic states of water percolation. (a) Dry State (b) Infiltration State (c) Diffusion State.*

Forward-Inverse Cycle

Figure 6.3 shows three standard inversion models for the three states of water percolation. In dry state, the crack is clearly visible. In infiltration state, the infiltrating plume is characterized through a distinct lower resistivity than the background, while in diffusion state the inversion did not sufficiently resolve the shape of the plume.

To analyze the dependence of the inversion results on the resistivity contrast between the plume and the host material, the plume resistivity was increased or lowered in steps of 250 Ωm around the minimal plume resistivity of 2000 Ωm. A total of nine models with plume resistivity ranging from 1000 to 3000 Ωm were explored, while the background resistivity stayed constant at 5000 Ωm.

Generally, the resistivity of an anomaly ρ^{-}_{anom} is

$$\rho^{-}_{anom} = \min\{\rho_i\} \tag{6.2}$$

for all model blocks i below the overburden. The misfit in the anomaly's resistivity $\Delta\rho_m$ is the difference between the resistivity of the anomaly in the generic $\rho^{-}_{anom,gen}$ and inverted model $\rho^{-}_{anom,inv}$:

$$\Delta\rho_m = \rho^{-}_{anom,gen} - \rho^{-}_{anom,inv} \tag{6.3}$$

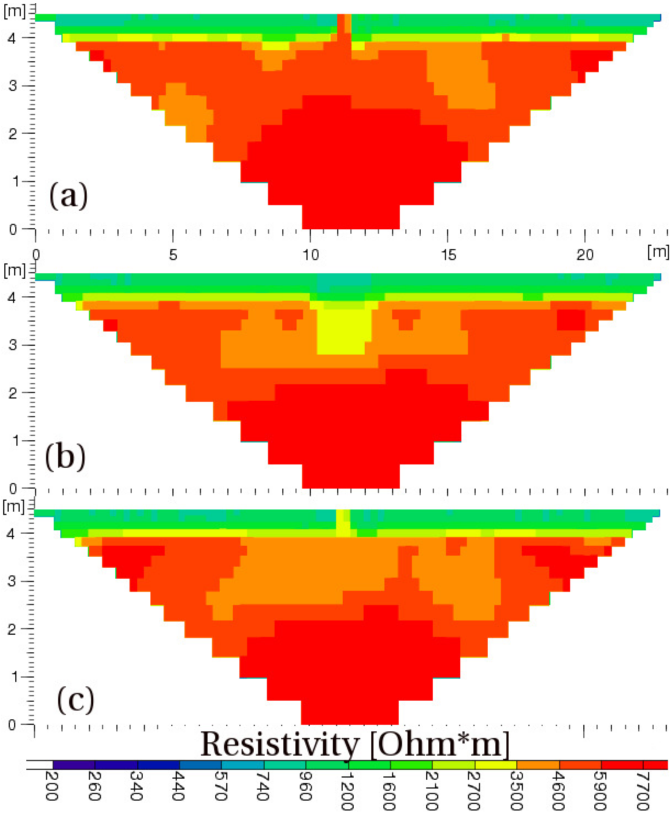

Figure 6.3: *Inverted models for the defective sealing. (a) Dry State (b) Infiltration State (c) Diffusion State.*

For this case study, ρ^{-}_{anom} corresponds to the resistivity in the center of the plume. Figure 6.4 shows the results of the forward-inverse cycle as $\Delta\rho_m$ vs the resistivity contrast. While the error in resistivity quantification is the smallest for the orginal contrast of 4:10, smaller and higher contrasts both result in increasingly larger $\Delta\rho_m$.

$\Delta\rho_m$ is slightly smaller in the infiltration state. In the diffusion state, the center

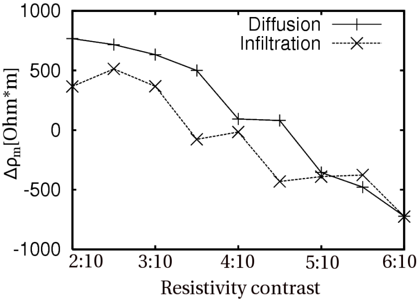

Figure 6.4: *Variations in the data for the case of the defective sealing, shown is the resistivity contrast as the ratio plume:host material (x-axis) vs* $\Delta\rho_m$ *of the the inverted model (y-axis).*

of the plume has sunk to greater depth, where the lower sensitivity of ERT may be the reason for a less accurate quantification.

Ensemble

The inversion ensemble for the case of the defective sealing and the diffusion state is shown in Figure 6.5. All models within the ensemble detected the overburden with the damaged sealing, but the model parts below this overburden show different features. In the first cluster, Ω-sloped artifacts appear to the side of the plume with equal resistivity as the plume itself. In the second cluster the artifacts appear as well, but have comparably higher resistivity, so that the plume appears as a distinct feature. In the third cluster, both plume and Ω-sloped artifacts are roughly in the same resistivity range, but have a higher resistivity than in cluster 1. The fourth cluster comprises strongly damped models where the plume is mostly visible. The last cluster shows models where the plume is clearly visible, with comparably better contrast, but mostly the vertical extent of the plume feature is overestimated.
To comprehend the ensemble results in a simple way, averaged models of each cluster are shown in Figure 6.6. As the clustering process already involves av-

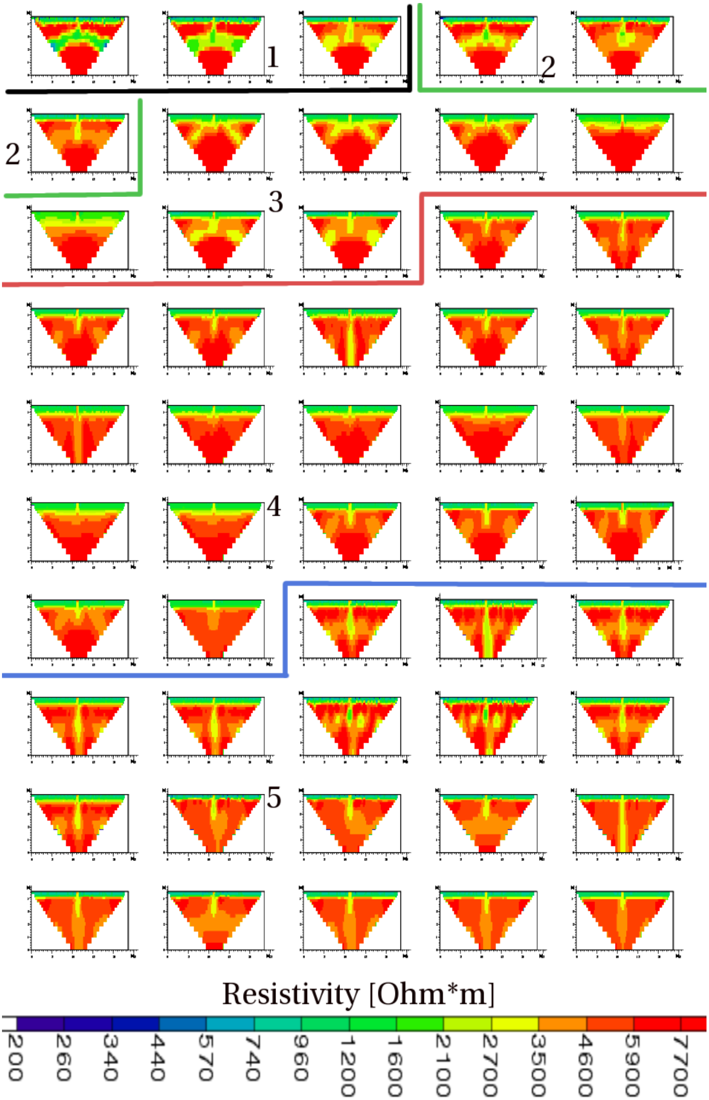

Figure 6.5: *Clustered ensemble with 50 possible models for the diffusion state of the defective sealing with an infiltration plume. The domains of the 5 clusters are indicated by numbers and dividing lines.*

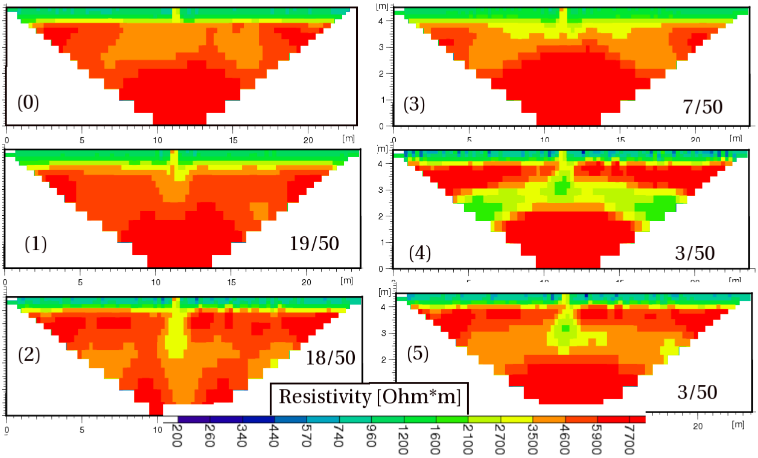

Figure 6.6: *Standard model (0) and averaged cluster models (1-5) for the defective sealing. Note that in contrast to Figure 6.5, the clusters are sorted in descending order by the number of ensemble members.*

eraging, this is a valid method. In Figure 6.6, the mean models for each of the clusters of the ensemble shown in Figure 6.5 are now listed according to the number of cluster members. It must be noted that the smallest cluster contains only 3 models, whereas the largest cluster contains almost half the models of the ensemble. The average RMS error of each cluster is below 4%.

The most prominent feature retrieved present in all models is the two-layered structure. This structure is present even in clusters where the damping is strong enough to nearly hide the plume anomaly. When comparing clusters 3-5 to the strongly damped inversion results in cluster 1, the typical Ω-sloped structure can be identified as an artifact at the lateral boundaries of the plume. Compared to the standard model (0), the cluster averages allow a much better identification of features, even though some interpretational experience or a priori knowledge is needed to distinguish between real anomalies (cluster 5) and artifacts (cluster 4).

Organic Overburden	With	Without			
Depth of the anomaly [m]	0.35	0.55	0.75	0.95	1.15
Stage of Percolation	Dry	Infiltration	Diffusion		
ERT array	WS	DD			

Table 6.2: *Parameter variation for different soil models, infiltration state and measurement geometry.*

6.2.2 Second Case: Hydraulically Resistive Anomaly

In the second case, the accuracy of resistivity quantification for a rectangular, hydraulically resistive anomaly placed below the organic overburden is studied. First, a model with an anomaly at 0.55 m depth and an organic overburden was created in HYDRUS. To represent the hydraulically resistive material of the anomaly, the same material as for the organic overburden is used. Then, multiple versions of this model were created with slightly different setups. Table 6.2 shows the possible differences between the models, which will be explained in the following paragraphs.

Water Simulation

In the simulation of water movement, a dry state, an infiltration state and a diffusion state were identified as characteristic states of an infiltrating water front. In the dry state (Fig. 6.7a), the soil is completely free of water. In the infiltration state (Fig. 6.7b), the water front is propagating into the volume. The hydraulically resistive anomaly causes water to impound on top, only slowly infiltrating into the anomaly. In the diffusion state (Fig. 6.7c), the infiltration front has reached the bottom boundary of the model, and the organic overburden and parts of the sand directly below are beginning to dry. The anomaly is filled with water and starts to infiltrate into the sand beneath.
Analysis of the quality of water content estimation through ERT was conducted for a variety of models and electrode configurations based on the three states of

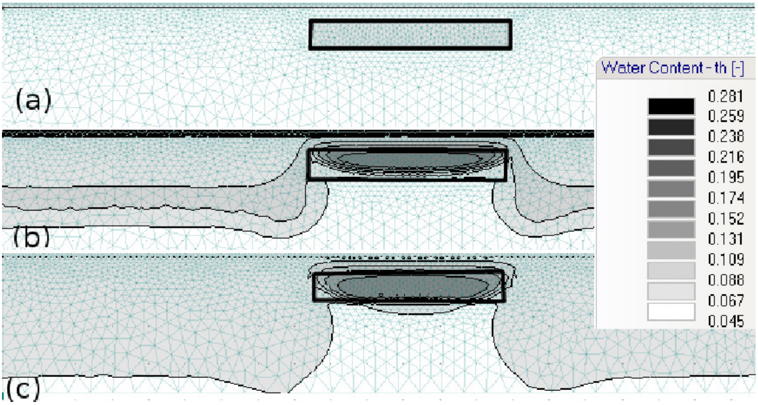

Figure 6.7: States of the simulation of water movement through a model with a hydraulically resistive anomaly (rectangular block marked with thick black outline). The layer boundary between organic overburden and sand is marked with a thin horizontal line. (a) Dry State (b) Infiltration State (c) Diffusion State.

water percolation in Figure 6.7. To study the influence of contrasting resistivities at the surface, models with and without an organic overburden were used for simulation. In addition, the depth of the anomaly was varied in steps of 0.2m with the upper boundary at 0.35 m to 1.15 m depth. To examine the effect of electrode configuration, two different electrode arrays (Wenner-Schlumberger and Dipole-Dipole) were used for each model (Table 6.2).

Forward-Inverse Cycle

Inspection of the inverted models (Fig. 6.8, right column) shows that the rectangular shape of the anomaly cannot be exactly retrieved. Determination of an average resistivity of the anomaly would be dependent on an arbitrary determination of anomaly borders. It is also not possible to determine the average resistivity at the actual position of the anomaly, since the perceived depth of the

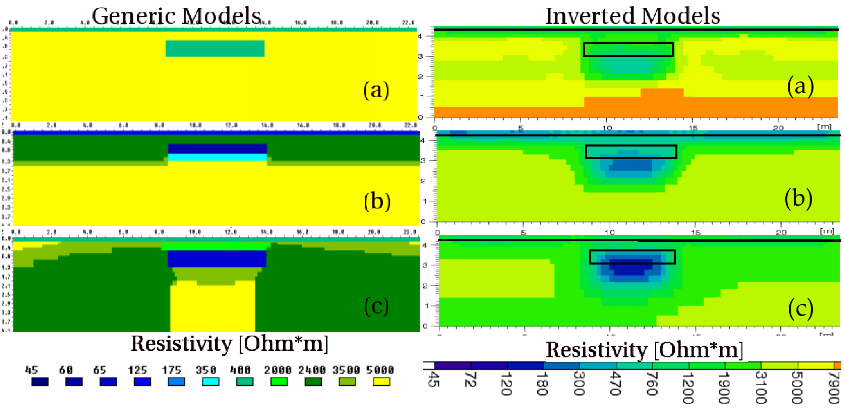

Figure 6.8: Generic and inverted models for the anomaly. (a) Dry State (b) Infiltration State (c) Diffusion State. The black rectangle in the right column marks the location of the anomaly in the left column, the thin horizontal line marks the layer boundary between organic overburden and sand.

anomaly is greater than the actual depth.

In the following, results for the different models shown in Table 6.2 will be compared regarding $\Delta\rho_m$ (Eq. 6.3), which now corresponds to the (minimal) resistivity of the anomaly. Figure 6.9 shows $\Delta\rho_m$ as a function of anomaly depth.

For the Wenner-Schlumberger array, $\Delta\rho_m$ increases with anomaly depth, reaching up to 2-3 times the expected value. A much better estimate is obtained if no organic overburden is present (grey curves). For these cases, better quantifications of ρ_{anom}^{-} are possible and $\Delta\rho_m$ increases only slightly with depth. In the diffusion state, significantly smaller errors occur compared to other states of water percolation, especially in the presence of an organic overburden.

As can be seen in Figure 6.8, the error in depth resolution is rather large. If an organic overburden is present, the thickness of this layer is overestimated, causing a shift in the vertical position of the anomaly of 0.3 to 0.4 m. It was also observed that at greater depths, the position stays approximately the same for

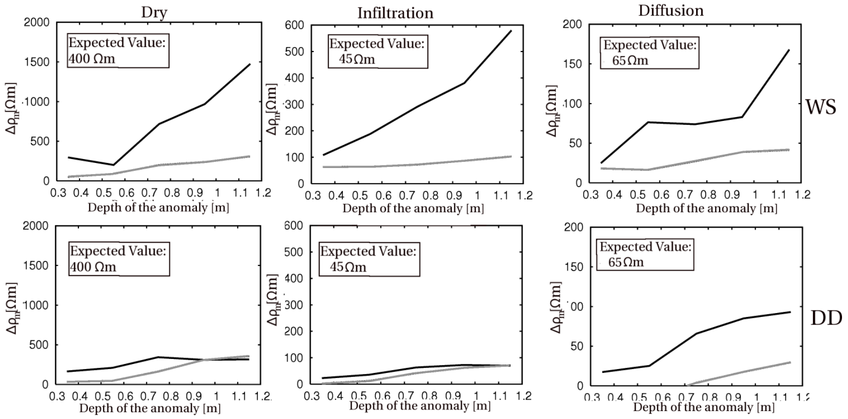

Figure 6.9: $\Delta\rho_m$ *for cases with organic overburden (black line) and without (grey line). Top row: Survey with Wenner-Schlumberger, bottom row: with Dipole-Dipole. The left column shows the dry state, the middle column the infiltration state and the right column the diffusion state.*

an anomaly expected at 0.75 m to 1.15 m depth. Again, in the case of a model without an organic overburden, the higher sensitivity due to higher resistivities near the surface makes better depth determination possible.

For models simulated with the Dipole-Dipole array, errors for models with organic overburden are significantly smaller than for the Wenner-Schlumberger array. However, the Dipole-Dipole array was shown to be very sensitive to noise and disturbances at the surface (like a stone pathway), to a point were measurements taken using this array could not be interpreted with the available inversion routines (see A).

As a measure of the quality of the inversion, a simple criterion containing the model misfit M as the sum of all errors has been applied:

$$M = \sum_{F_i} |\rho_{inv,i} - \rho_{gen,i}| \tag{6.4}$$

where F_i is the i-th model block of the inversion domain discretization.

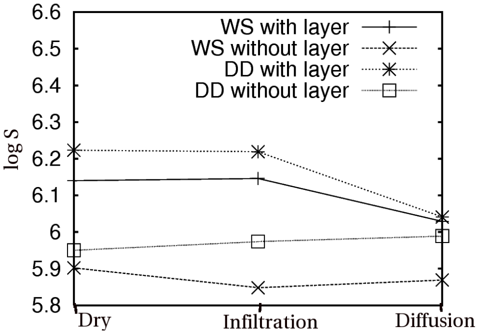

Figure 6.10: *Cumulative block misfits for the three stages of water perolation. Shown is the logarithm of the sum of all errors M for Wenner-Schlumberger and Dipole-Dipole arrays and with or without an organic overburden.*

Comparison of M for the different states of water percolation (Fig. 6.10) shows that the diffusion state gives significantly better results.

Figure 6.11 shows the spatial error distribution for each state. In the dry state, the biggest errors stem from an overestimated thickness of the overburden, which also entails further mispositioning of the anomaly. The anomaly itself is also vertically elongated, leading to considerable errors in the lower parts. In the diffusion state (Fig. 6.11b), the resistivity contrast between overburden and wet sand is much smaller, due to a) the sand having a reduced resistivity as it is more saturated with water and b) the overburden being dryer as in the previous states, resulting in a higher resistivity. As a consequence of this reduced resistivity contrast, the errors resulting from an incorrect overburden thickness are reduced as well.

Ensemble

For the case of the hydraulically resistive anomaly, the random set of parameters is applied to generic models of all three different states of water percolation. To assure comparability, the random parameter set stays the same for each of the

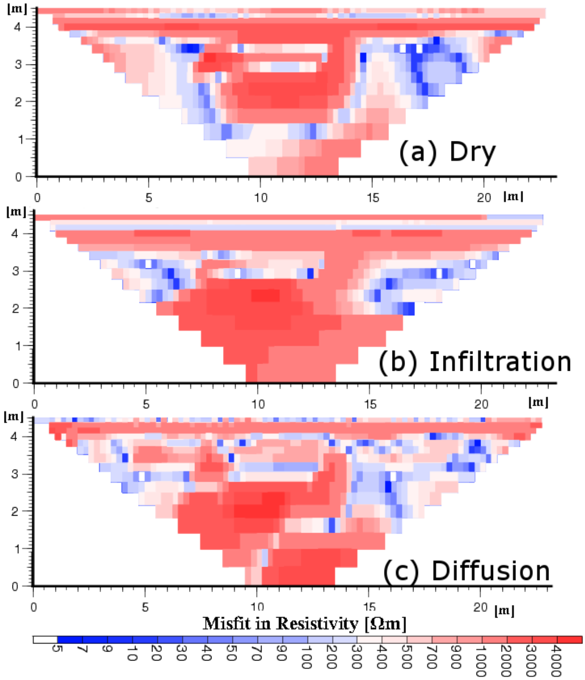

Figure 6.11: *Misfit in resistivity distribution by model blocks for anomaly at 0.95 m depth with organic overburden and Wenner-Schlumberger array.*

three models.
A model with an anomaly at 0.75 m depth was used, including an organic overburden and using the Wenner-Schlumberger array. For each state, an ensemble of 50 inverted models was created. For simplification, only mean cluster members are shown. Five clusters per ensemble were chosen, which are shown in Figure 6.12 with the respective number of ensemble members. The respective $\Delta\rho_m$ is listed in Table 6.3.

- Dry State: The rectangular shape of the anomaly is retrieved variably

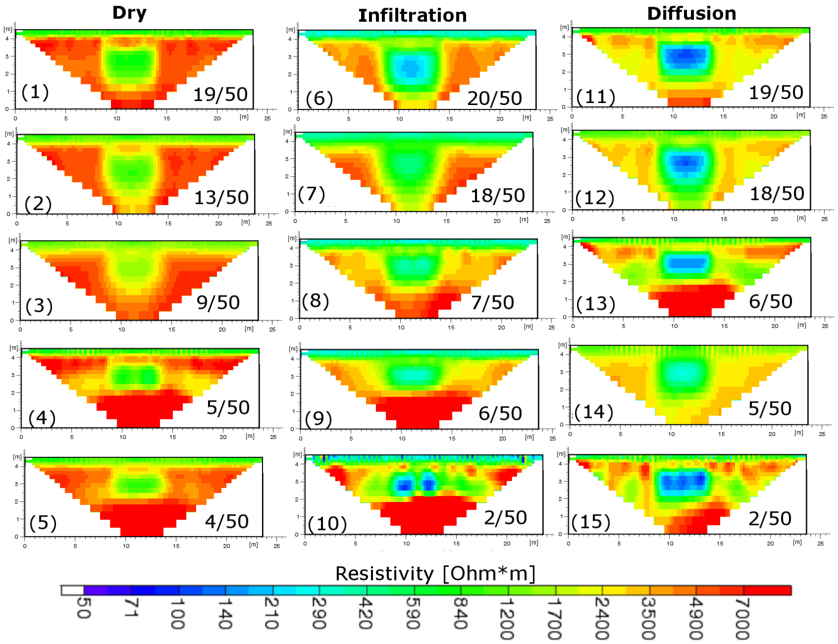

Figure 6.12: *Averaged cluster representatives for the resistive anomaly in the dry (left), infiltration (middle) and diffusion (right) state.*

Cluster DRY	Cluster INFILTRATION	Cluster DIFFUSION
1) 381	6) 156	11) 49
2) 613	7) 294	12) 41
3) 228	8) 314	13) 86
4) 1068	9) 73	14) 62
5) 608	10) 292	15) 228

Table 6.3: *Misfit for the cluster representative shown in Figure 6.12 (misfits in Ωm).*

well, but for the models 4 and 5, where the thickness of the anomaly is smaller, a strong overestimation of resistivities is present in the lower part of the model ($> 7000\ \Omega m$ instead of $5000\ \Omega m$). The resistivity of the anomaly ρ^{-}_{anom} is much too high for all five models. For models 1 and 2 that contain most of the ensemble members, the anomaly is vertically elongated.

- Infiltration State: In four models, the shape of the anomaly has been retrieved quite well, but for model 10, two zones of minimal resistivity have been detected rather than the rectangular shape. In all models, $\Delta\rho_m$ is very large compared to the expected resistivity of the anomaly $\rho = 65\ \Omega m$. Again, models 9 and 10 (same inversion parameters as model 4 and 5) overestimate the background resistivity at greater depth.

- Diffusion State: The resistivity of the anomaly is detected with lower resistivity as in infiltration state, closer to the expected resistivity of $45\ \Omega m$. Again, in model 13 and 15, the strong inversion artifact is present near the bottom coinciding with the shape of the anomaly being retrieved quite well. These artifacts are not present in model 11, 12 and 14, where the anomaly is vertically elongated. Model 15 presents a mixed case of a slightly elongated anomaly and an artifact of smaller extent than in model 13.

Table 6.3 shows, sorted for the cluster representatives, the misfits in the anomaly's resistivity. While it is apparent that the errors are large in each case, they are again considerably smaller for the diffusion state

6.3 Discussion and Conclusion

The ability of electrical resistivity tomography to accurately determine resistivity distributions was examined and a five-step framework to analyze and improve the ERT interpretation was proposed. The general idea comprises the modeling of soil water movement for synthetic soil data sets, and a transfer into a model of generic resistivities using a petrophysical relation. Using a forward-inverse modeling cycle, it can be evaluated how well the geophysical inversion scheme can reconstruct the given soil data set and its water content. An ensemble and clustering approach was introduced that was motivated by the finding that a single model deduced as the optimal model does not necessarily reproduce the expected resistivities accurately.

These five steps were applied to two case studies of simple soil models based on a two-layered structure reproducing field observations. The first case simulates the infiltration of water through a cracked surface sealing, and the second a hydraulically resistive anomaly in a sand layer.

Key results of the forward-inverse modeling in this study include:

- In the presence of large resistivity contrasts, e.g. a conductive organic overburden, the retrieval of accurate resistivity values beneath this layer using the regularization based inversion method applied in this study is not possible. However, if the volume is monitored at various stages of water percolation, the retrieval quality can differ. Especially in the diffusion state, much better accuracy was possible.

- The model misfit increases with depth, as the sensitivity of the inversion model to the data decreases.

- In the absence of an organic overburden, a much better quantification is possible because of a lower resistivity contrast.

- The numerical study showed that a Dipole-Dipole array provides more accurates inversions than the Wenner-Schlumberger array. However, in practical applications, it has to be ensured the signal-to-noise ratio is sufficiently large.

As a consequence, an ensemble approach was introduced that creates multiple different inverted models for one data set by randomly choosing the inversion parameters from the possible (and numerically plausible) parameter space. By using clustering methods, averaged models representing different clusters in the ensemble can be created and compared. Key results of the ensemble approach include:

- Clustering of ensemble members allows an evaluation of the different possible models that fit the data. Areas likely to be plagued by artifacts can be identified and the reliability of standard inverted models can be evaluated.

- However, the quantification of resistivities is not considerably improved by ensembles. For example, it became apparent that resistivities retrieved with smaller misfits in one region can coincide with larger artifacts in other regions.
- The clustering of ensembles allows an overview of the ensemble, without losing information about the ensemble.

The ideas of the approaches presented here can easily be adapted to different models and inversion methods. For the specific inversion process with regularization used in this study, it can be concluded that a reliable quantification of resistivity values is not possible. The use of additional information, e.g. within a framework aiming at directly inverting or calculating hydrological properties from collected data sets that not only contain resistivity measurements, but also data about the flow conditions, e.g. meteorological data, should be considered.

7 Conclusions and Outlook

Methods to monitor the soil water content of flood-protection dikes have been developed and evaluated. The viability of ERT for quantifying water content was demonstrated for dike models. First experiments on laboratory dikes indicated that water content changed can be monitored with ERT, but the small dimensions of the dike models had assumedly influenced the measurements. The main experiments took place on a full-scale dike model where water content could be controlled by sprinkling and flooding. During a flooding experiment, monitoring of water content evolution was successfully. It was shown that ERT can be used as a principal monitoring method, if it is applied in conjunction with another method to determine the initial water content. Both TDR and GPR methods have been used to obtain initial water content estimates, and by comparison of water content from TDR and resistivity values from ERT the parameter for the applied petrophysical relation was estimated. Results show good quantification of water content during rainfall and flooding events. ERT was able to determine the volumetric water content of 34% in the saturated area during a flooding experiment. Co-measured values from TDR and ERT were used to estimate a parameter in the petrophysical relationship connecting water content and resistivity. It was shown that inversion artifacts can be introduced as a consequence of resistivity contrasts, so a careful examination of inverted models is a crucial part of each investigation. The results obtained on the full-scale dike model were conditional on the completely homogeneous dike structure.

A comparison with other geophysical methods in combination with a translation to heterogeneous sites was introduced by involving data from other field campaigns on sites in the Black Forest and Burkina-Faso. The tested methods included ERT, GPR, TDR and FDR. For a low degree of heterogeneity, pointlike probes can measure representative values for the site, especially if the main interest lies in water content changes and not absolute values. If a more detailed monitoring of water content distribution is needed, as is the case for the monitoring of flood-protection dikes, a method that retrieves two- or three-dimensional profiles like ERT is appropriate. If the heterogenity of the site is high, but the water content has to be known on large scales, e.g. for meteorological forecasting, connecting pointlike measurements with water content variability is non-trivial, and an optimal monitoring should be based on repeated measurements, e.g. with GPR or ERT.

ERT has the potential to be used as a primary, permanently installed and automated measurement method for dike monitoring. To control the safety of the dike, a prediction of water content evolution can complete the measurement of current water content. Predicting water content evolution was evaluated by simulating water movement in a numerical model. This way, the expected changes in water content can be estimated. A long-term simulation based on a 5 years meteorological time series found small temporal variations in water content and allowed determination of the autocorrelation of water content over time.

The prediction of water content evolution was further examined using meteorological forecast data anteceding selected rainfall events on an experimental site during the COPS field campaign. The results showed that runs of forecast models started at different times often underestimate the rainfall amount, but that the timing of major precipitation events was predicted well for the two cases studies, so that the correct trend in water content change would have been predictable.

As a consequence of applications using ERT for measuring and numerical modeling, an integrated approach was introduced to evaluate the reliability of ERT for quantifying resistivities and consequently, water content. This approach has the advantage of a) modeling synthetic data sets as close as possible to natural processes and b) evaluating not each method seperately, but rather a combination of hydrological and resistivity modeling. A method was proposed that includes two approaches for evaluating and enhancing resistivity quantification that comprise all processing steps of measuring and inverting resistivity data and simulating water content change. The method was applied to two synthetic case studies. Results showed that the resistivities are often determined with large errors that are influenced by decreasing sensitivity with exploration depth and the amount of resistivity contrast present. A conclusion is that even if an optimum model can be found with respect to the inversion approach employed, the results might still not be sufficiently accurate. Consequently, an ensemble approach was introduced that randomly determined 50 different inversion models for a chosen inversion approach and ordered them into clusters of similar models. This allows a better interpretation of the qualitative features of the inversion models, but no necessary improvement of the quantification.

In further work, regarding the applicability of geophysical methods like ERT on real dikes of unknown structure and material, only approaches that combine information from multiple methods will succeed in quantifying water processes in the subsurface. These approaches might combine resistivity data from ERT with GPR measurements. But more importantly these approaches should also include modeling of the relevant processes, in this case the water percolation in the soil. The hydrological modeling will constrain the ERT inversion to avoid large changes in parts of the model where small changes in water content are expected. This way, artifacts can be avoided and the quantification of the real processes will be improved.

Bibliography

Ament, F. and Simmer, C.: Improved representation of land-surface heterogeneity in a non-hydrostatic numerical weather prediction model, Boundary-Layer Meteorology, 121, 153–174, 2006.

Archie, G. E.: The electrical resitivity log as an aid in determining some reservoir characteristics, American Institute of Mining and Metallurgical Engineers, pp. 55–62, 1942.

Arya, S. P.: Introduction to Micrometeorology, International Geophysics Series, Academic Press, New York and London, second edn., 2001.

Athanasiou, E. N., Tsourlos, P. I., Papazachos, C. B., and Tsokas, G. N.: Combined weighted inversion of electrical resistivity data arising from different array types, Journal of Applied Geophysics, 62, 124–140, 2007.

Baker, R. D., Lynn, B. H., Boone, A., Tao, W.-K., and Simpson, J.: The influence of soil moisture, coastline curvature, and land-breeze circulations on sea-breezed precipitation, Journal of Hydrometeorology, 2, 192–211, 2001.

Barker, R. and Moore, J.: The application of time-lapse electrical tomography in groundwater studies, The Leading Edge, pp. 1454–1458, 1998.

Batchelor, C. H.: The accuracy of evapotranspiration estimated with the FAO modified Penman equation, Irrigation Science, 51, 223–233, 1984.

Bear, J.: Dynamics of fluids in porous media, Elsevier Publishing, New York, 1972.

Bieberstein, A.: Leckageortung bei geotechnischen Dichtungen mittels elektrischem Potentialverfahren, Ph.D. thesis, Institute for Rock Mechanics and Soil Mechanics, University of Karlsruhe, 1999.

Binley, A., Henry-Poulter, S., and Shaw, B.: Examination of solute transport in an undisturbed soil column using electrical resistance tomography, Water Resources Research, 32, 763–769, 1996.

Binley, A., Cassiani, G., Middleton, R., and Winship, P.: Vadose zone model parameterisation using cross-borehole radar and resistivity imaging, Journal of Hydrology, 267, 147–159, 2002a.

Binley, A., Winship, P., West, L. J., Pokar, M., and Middleton, R.: Seasonal variation of moisture content in unsaturated sandstone inferred from borehole radar and resistivity profiles, Journal of Hydrology, 267, 160–172, 2002b.

Bloeschl, G. and Sivapalan, M.: Scale issues in hydrological modelling: a review, Hydrological Processes, 9, 251–290, 1995.

Bogena, H., Schulz, K., and Vereecken, H.: Towards a network of observatories in terrestrial environmental research, Advances in Geosciences, 9, 109–114, 2005.

Brandelik, A. and Huebner, C.: Moisture monitoring in waste disposal surface barriers, Environmental Monitoring and Assessment, 84, 61–70, 2003.

Braun, F. J. and Schaedler, G.: Comparison of soil hydraulic parameterizations for mesoscale meteorological models, Journal of Applied Meteorology, 44, 1116–1131, 2005.

Bridge, H. and Hyndman, D., eds.: Aquifer characterization, Society of Economic and Petroleum Geologists, 2004.

Bristow, C. S. and Jol, H. M., eds.: Ground penetrating radar in sediments, vol. 211 of *Special Publications*, Geological Society, London, 2004.

Brooks, R. H. and Corey, A. T.: Properties of porous media affecting fluid flow, J. Irrigation and Drainage Div., Proc. Am. Soc. Civil Eng., 92, 61–88, 1966.

Burman, R. and Pochop, L. O., eds.: Evaporation, evapotranspiration and climatic data, vol. 22 of *Developments in Atmospheric Science*, Elsevier Science, 1994.

Carle, S., Ramirez, A., Daily, W., Newmark, R., and Tompson, A.: High-Performance computation and geostatistical experiments for testing the capabilities of 3-D electrical resistance tomography, in: The 12th Annual Symposium on the Application of Geophysics to Environmental and Engineering Problems (SAGEEP), Oakland, CA, 1999.

Carr, J. R.: Numerical analysis for geological sciences, Prentice Hall, Engelwood Cliffs, NJ, 1995.

Cassiani, G. and Binley, A.: Modeling unsaturated flow in a layered formation under quasi-steady state conditions using geophysical data constraints, Advances in Water Resources, 28, 467–477, 2005.

Cassiani, G., Strobbia, C., and Gallotti, L.: Vertical radar profiles for the characterization of deep vadose zones, Vadose Zone Journal, 3, 1093–1105, 2004.

Charlesworth, P.: Soil water monitoring, national program for sustainable irrigation, Land and Water Australia, Canberra, 2005.

Cheng, W. Y. and Cotton, W. R.: Sensitivity of a cloud-resolving simulation of the genesis of a mesoscale convective system to horizontal heterogeneities in soil moisture initialization, Journal of Hydrometeorology, 5, 934–958, 2004.

Dahlin, T. and Zhou, B.: A numerical comparison of 2D resistivity imaging with 10 electrode array, Geophysical Prospecting, 52, 379–398, 2004.

Dai, A., Trenberth, K. E., and Karl, T. R.: Effects of clouds, soil moisture, precipitation and water vapor on diurnal temperature range, Journal of Climate, 12, 2451–2473, 1999.

Daily, W. and Ramirez, A.: Electrical resistivity tomography of vadose water movement, Water Resources Research, 28, 1429–1442, 1992.

Dannowski, G. and Yaramanci, U.: Estimation of water content and porosity using combined radar and geoelectrical measurements, European Journal of Environmental and Engineering Geophysics, 4, 71–85, 1999.

Davis, J. L. and Annan, A. P.: Ground penetrating radar for high-resolution mapping of soil and rock stratigraphy, Geophysical Prospecting, 37, 531–551, 1989.

Day-Lewis, F., Lane jr., J. W., and Gorelick, S. M.: Combined interpretation of radar, hydraulic and tracer data from a fractured-rock aquifer, Hydrogeological Journal, 13, doi:10.1007/s10040-004-0372-y, 2004.

Day-Lewis, F. D., Singha, K., and Binley, A. M.: Applying petrophysical models to radar travel time and electrical resistivity tomograms: Resolution-dependent limitations, Journal of Geophysical Research, 110, B08 206, doi:10.1029/2004JB003569, 2005.

de la Vega, M., Osella, A., and Lascano, E.: Joint inversion of Wenner and dipole-dipole data to study a gasoline-contaminated soil, Journal of Applied Geophysics, 54, 97–109, 2003.

deGroot Hedlin, C. and Constable, S.: Occam's inversion to generate smooth, two-dimensional models from magnetotelluric data, Geophysics, 55, 1613–1624, 1990.

Desai, A., Davis, K. J., Senff, C. J., Ismail, S., Browell, E. V., Stauffer, D. R., and Reen, B. P.: A case study on the effects of heterogeneous soil moisture on mesoscale Boundary-Layer structure in the southern Great Plains, U.S.A. Part I: Simple prognostic model, Boundary-Layer Meteorology, 119, 195–238, 2006.

Doorenbos, J. and Pruitt, W. O.: Guidelines for predicting crop water requirements, FAO Irrigation and Drainage, 24, 1977.

French, H. K., Hardbattle, C., Binley, A., Winship, P., and Jakobsen, L.: Monitoring snowmelt induced unsaturated flow and transport using electrical resistivity tomography, Journal of Hydrology, pp. 273–284, 2002.

Garambois, S., Sénéchal, P., and Perroud, H.: On the use of combined geophysical methods to assess water content and water conductivity of near-surface formations, Journal of Hydrology, 259, 32–58, 2002.

Godio, A. and Naldi, M.: Two-dimensional Electrical Imaging for Detection of Hydrocarbon Contaminants, Near Surface Geophysics, 1, 131–137, 2003.

Greco, R.: Soil water content inverse profiling from single TDR waveforms, Journal of Hydrology, 317, 325–339, 2006.

Hauck, C. and Vonder Muehll, D.: Inversion and interpretation of two-dimensional geoelectrical measurements for detecting permafrost in mountainous regions, Permafrost and Periglacial Processes, 14, 305–318, doi:10.1002/ppp.462, 2003.

Hennig, T., Weller, A., and Canh, T.: The effect of dike geometry on different resistivity configurations, Journal of Applied Geophysics, 57, 278–292, 2005.

Hubbard, S. S., Rubin, Y., and Majer, E.: Spatial correlation structure estimation using geophysical and hydrogeological data, Water Resources Research, 35, 1809–1825, 1999.

Huisman, J. A., Hubbard, S. S., Redman, J. D., and Annan, A. P.: Measuring soil water content with ground penetrating radar: a review, Vadose Zone Journal, 2, 476–491, 2003.

Igel, J. S., Anschuetz, H. R., Schmalholz, J., Wilhelm, H., Breh, W., Hoetzel, H., and Huebner, C.: Methods for determining soil moisture with the ground penetrating radar, in: Proceedings of the 4th International Conference on Electromagnetic Wave Interaction with Water and Moist Substances, Weimar, pp. 484–491, 2001.

Ippisch, O.: Coupled transport in natural porous media, Ph.D. thesis, Combined Faculties for the Natural Sciences and for Mathematics of the Rupertus Carola University of Heidelberg, Germany, 2001.

Isaaks, E. H.: Applied Geostatistics, Oxford University Press, 1990.

Kemna, A., Vanderborght, J., Kulessa, B., and Vereecken, H.: Imaging and characterisation of subsurface solute transport using electrical resistivity tomography (ERT) and equivalent transport models, Journal of Hydrology, 267, 125–146, 2002.

Kerr, Y. H.: Soil moisture from space: where are we?, Hydrogeological Journal, 15, 117–200, 2007.

Kerr, Y. H., Waldteufel, P., Wigneron, J.-P., Martinuzzi, J.-M., Font, J., and Berger, M.: Soil moisture retrieval from space: The soil moisture and ocean salinity (smos) mission, IEEE transactions on Geoscience and Remote Sensing, 39, 1729–1735, 2001.

Koeniger, F., Nueesch, R., Rabl-Lasar, W., Roth, J., Ruppert, R., and Schuhmann, R.: Alternative surface covering of landfill using the TAUPE sealing monitoring system, in: Proceedings of ISEMA 2005, 6th International Conference on Electromagnetic Wave Interaction with Water and Moist Substances, Weimar, Germany, 2005.

Kool, J. B. and Parker, J. C.: Development and evaluation of closed-form expressions for hysteretic soil hydraulic properties, Water Resources Research, 23, 105–117, 1987.

Kowalsky, M. B., Finsterle, S., Peterson, J., Hubbard, S., Rubin, Y., Majer, E., Ward, A., and Gee, G.: Estimation of field-scale soil hydraulic and dielectric parameters through joint inversion of GPR and hydrological data, Water Resources research, 41, W11 425, doi:10.1029/2005WR004237, 2005.

Krauss, L., Hauck, C., Kalthoff, N., and Kottmeier, C.: Atmosphere-ground interaction in the context of convective precipitation using a soil moisture and energy balance network during COPS, in: Eos Transactions AGU, H33C-1450, Fall Meet. Suppl., 2007.

LaBrecque, D., Sharpe, R., and Casale, D.: Combined electrical and magnetic resistivity tomography : synthetic model study and inverse modeling, Journal of Environmental and Engineering Geophysics, 8, 251–262, 2003.

LaBrecque, D. J. and Yang, X.: Difference inversion of ERT data: a fast inversion method for 3-D in situ monitoring, Journal of Environmental & Engineering Geophysics, 6, 83–89, 2001.

LaBrecque, D. J., Heath, G., Sharpe, R., and Versteeg, R.: Autonomous monitoring of fluid movement using 3-D electrical resistivity tomography, Journal of Environmental and Engineering Geophysics, 9, 53–62, 2004.

Lambot, S., Slob, E. C., Vanclooster, M., and Vereecken, H.: Closed loop GPR data inversion for soil hydraulic and electric property determination, Geophysical research Letters, 33, L21 405, doi:10.1029/2006GL027906, 2006.

Leidenberger, P., Oswald, B., and Roth, K.: Efficient reconstruction of dispersive dielectric profiles using time domain reflectometry (TDR), Hydrology and Earth System Sciences, pp. 209–232, 2006.

Lenhard, R. J., Parker, J. C., and Kaluarachchi, J. J.: Comparing simulated and experimental hysteretic two-phase transient fluid flow phenomena, Water Resources Research, 27, 2113–2124, 1991.

Linde, N., Binley, A., Tryggvason, A., Pedersen, L. B., and Revil, A.: Improved hydrogeophysical characterization using joint inversion of cross-hole electrical resistance and ground-penetrating radar traveltime data, Water Resources Research, 42, W12 404, 2006.

Loke, M. H.: RES2DMOD version 2.2: rapid 2-D resistivity forward modeling using the finite-difference and finite-element methods, Tech. rep., GeoTomo LLC, Penang, Malaysia, 1999.

Loke, M. H.: Topographic modelling in electrical imaging inversion, in: Proceedings, 62nd Conference and Technical Exhibition, EAGE, 2000.

Loke, M. H. and Barker, R. D.: Least-squares deconvolution of apparent resistivity, Geophysics, 60, 1682–1690, 1995.

Loke, M. H. and Barker, R. D.: Rapid least-squares inversion of apparent resistivity pseudosections using a quasi-Newton method, Geophysical Prospecting, 44, 131–152, 1996.

Loke, M. H. and Dahlin, T.: A comparison of the Gauss-Newton and quasi-Newton methods in resistivity imaging inversion, Journal of Applied Geophysics, 49, 149–162, 2002.

Loke, M. H., Acworth, I., and Dahlin, T.: A comparison of smooth and blocky inversion methods in 2D electrical imaging surveys, Exploration Geophysics, 34, 182–187, 2003.

Meissner, C., Kalthoff, N., Kunz, M., and Adrian, G.: Initiation of shallow convection in the Black Forest mountains, Atmospheric Research, 86, 42–60, doi: 10.1016/j.atmosres.2007.03.003, 2007.

Mualem, Y.: A new model for predicting the hydraulic conductivity of unsaturated porous media, Water Resources Research, 12, 513–522, 1976.

Müller, O.: Sicherheitsueberpruefung von Deichen und Daemmen, Wasser & Boden, 51/6, 15–18, 1999.

Nguyen, F., Garambois, S., Chardon, D., Hermitte, D., Bellier, O., and Jongmans, D.: Subsurface electrical imaging of anisotropic formations affected by a slow active reverse fault, Provence, France, Journal of Applied Geophysics, 62, 338–353, 2007.

Nielsen, D. R. and Luckner, L. M.: Theoretical aspects to estimate reasonable initial parameters and range limits in identification procedures for soil hydraulic properties, in: Proc. Intl. Workshop on Indirect Methods for Estimating the Hydraulic Properties of Unsaturated Soils, edited by van Genuchten, M. T., Leij, F. J., and Lund, L. J., pp. 147–160, University of Riverside, California, 1992.

Nielsen, D. R., Biggar, J. W., and Erh, K. T.: Spatial variability of field-measured soil-water properties, Hilgardia, 42, 215–259, 1973.

Oldenborger, G. A., Routh, P. S., and Knoll, M. D.: Sensitivity of electrical resistivity tomography data to electrode position errors, Geophysical Journal International, 163, 1–9, doi:10.1111/j.1365-246X.2005.02714.x, 2005.

Pinder, G. F. and Gray, W. G.: Finite element simulation in surface and subsurface hydrology, Academic Press, New York, 1977.

Polubarinova-Kochina, P. Y.: Theory of ground water movement, Princeton University Press, Princeton, New Jersey, 1962.

Preko, K.: Volumetric soil water content determination with ground penetrating radar (GPR), Ph.D. thesis, Geophysical Institute, University of Karlsruhe, 2008.

Redelsperger, J.-L., Thorncroft, C. D., Diedhiou, A., Lebel, T., Parker, D. J., and Polcher, J.: African Monsoon Multidisciplinary Analysis: an international research project and field campaign, Bulletin of the American Meteorological Society, 87, 1739–1746, 2006.

Rings, J., Woersching, H., and Hauck, C.: Comparing time-domain reflectometry and electrical resistivity tomography on a dike model, in: Proceedings, 11th European Meeting of Environmental and Engineering Geophysicists ”Near Surface 2005”, EAGE, 2005.

Robinson, D. A., Jones, S. B., Wraith, J. M., Or, D., and Friedman, S. P.: A review of advances in dielectric and electrical conductivity measurement in soils using time domain reflectometry, Vadose Zone Journal, 2, 444–475, 2003.

Robock, A., Vinnikov, K. Y., Srinivasan, G., Entin, J. K., Hollinger, S. E., Speranskaya, N. A., Liu, S., and Namkhai, A.: The global soil moisture data bank, Bulletin of the American Meteorological Society, 81, 1281–1299, 2000.

Rodell, M., Houser, P. R., Berg, A. A., and Famiglietti, J. S.: Evaluation of 10 methods for initializing a land surface model, Journal of Hydrometeorology, 6, 146–155, 2005.

Roth, K.: Soil Physics. Lecture notes., Institute of Environmental Physics, University of Heidelberg, 2006.

Roth, K., Schulin, R., Fluehler, H., and Attinger, W.: Calibration of time domain reflectometry for water content measurements using a composite dielectric approach, Water Resources Research, 267, 2267–2273, 1990.

Rubin, Y. and Hubbard, S. S.: Hydrogeophysics, Water Science and Technology Library, Springer-Verlag Berlin, Heidelberg, New York, 2005.

Sandberg, S. K., Slater, L. D., and Versteeg, R.: An integrated geophysical investigation of the hydrogeology of an anistropic unconfined aquifer, Journal of Hydrology, 267, 227–243, 2002.

Sandmeier, K.-J.: REFLEXW - Processing and interpretation software for GPR, seismic and borehole data, Sandmeier Scientific Software, version 4.5, 2007.

Schaedler, G.: Triggering of atmospheric circulations by moisture inhomogeneities of the Earth’s surface, Boundary-Layer Meteorology, 51, 1–29, 1990.

Schaer, C. and Jendritzky, G.: Hot news from summer 2003, Nature, 432, 559–560, 2004.

Scheuermann, A.: Instationäre Durchfeuchtung quasi-homogener Erddeiche, Dissertation, Institute for Rock Mechanics and Soil Mechanics, University of Karlsruhe, 2005.

Scheuermann, A., Schlaeger, S., Huebner, C., Brandelik, A., and Brauns, J.: Monitoring of the spatial soil water distribution on a full-scale dike model, in: Proceedings of the 4th International Conference on Electromagnetic Wave Interaction with Water and Moist Substances, Weimar, pp. 343–350, 2001.

Schlaeger, S.: Inversion von TDR-Messungen zur Rekonstruktion raeumlich verteilter bodenhydraulischer Parameter, Ph.D. thesis, Veroeffentlichungen des Institutes fuer Bodenmechanik und Felsmechanik der Universitaet Fridericiana in Karlsruhe, 2002.

Schlaeger, S.: A fast TDR-inversion technique for the reconstruction of spatial soil moisture content, Hydrology and Earth System Sciences, 9, 481–492, sRef-ID: 1607-7938/hess/2005-9-481, 2005.

Schlaeger, S., Huebner, C., and Becker, R.: Simple soil moisture probe for low-cost measurement applications, in: Proceedings of the 6th conference on electrocmagnetic wave interaction with water and moist substances, ISEMA, Weimar, 2005.

Schneider, J. M., Fisher, D. K., Elliott, R. L., Brown, G. O., and Bahrmann, C. P.: Spatiotemporal variations in soil water: first results from the ARM SGP CART network, Journal of Hydrometeorology, 4, 106–120, 2003.

Schulz, J.-P.: Introducing the Lokal-Modell LME at the German Weather Service, COSMO Newsletter, 5, 158–159, 2005.

Scott, P. S., Farquhar, G. J., and Kouwen, N.: Hysteresis effects on net infiltration, Advances in Infiltration, 11, 163–170, 1983.

Seuffert, G., Gross, P., and Simmer, C.: The influence of hydrologic modelling on the predicted local weather: two-way coupling of a mesoscale weather prediction model and a land surface hydrologic model, Journal of Hydrometeorology, 3, 505–523, 2002.

Simunek, J. and van Genuchten, M. T.: Estimating unsaturated soil hydraulic properties from tension disc infiltrometer data by numerical inversion, Water Resources Research, 32, 2683–2696, 1996.

Simunek, J., van Genuchten, M. T., and Sejna, M.: The HYDRUS software package for simulating the two- and three-dimensional movement of water, heat, and multiple solutes in variably-saturated media, technical manual, University of California Riverside, Riverside, CA, 2006.

Singha, K. and Gorelick, S. M.: Hydrogeophysical tracking of three-dimensional tracer migration: The concept and application of apparent petrophysical relations, Water Resources Research, 42, W06 422, doi:10.1029/2005WR004568, 2006.

Singha, K., Day-Lewis, F. D., and Lane, jr., J. W.: Geoelectrical evidence of bicontinuum transport in groundwater, Geophysical Research Letters, 34, L12 401, doi:10.1029/2007GL030019, 2007.

Sjoedahl, P., Dahlin, T., and Johansson, S.: Using resistivity measurements for dam safety evaluation at Enemossen tailings dam, in: Proceedings, 10th European Meeting of Environmental and Engineering Geophysics, Utrecht, EAGE, a017, 2004.

Sjoedahl, P., Dahlin, T., and Zhou, B.: 2.5D resistivity modeling of embankment dams to assess influence from geometry and material properties, Geophysics, 71, G107–G114, 2006.

Slater, L., Binley, A., Daily, W., and Johnson, R.: Cross-hole electrical imaging of a controlled saline tracer injection, Journal of Applied Geophysics, 44, 85–102, 2000.

Slater, L., Binley, A., Versteeg, R., Cassiani, G., Birken, R., and Sandberg, S.: A 3D ERT study of solute transport in a large experimental tank, Journal of Applied Geophysics, 49, 211–229, 2002.

Sogalla, M., Krueger, A., and Kerschgens, M.: Mesoscale modelling of interactions between rainfall and the land surfaces in West Africa, Meteorol. Atmos. Phys., doi: 10.1007/s00703-005-0109-z, 2005.

Sperl, C.: Determination of soil water content in an agro-ecosystem using the ground wave of ground penetrating radar, Ph.D. thesis, University of Munich, 1999.

Stacheder, M., Koehler, K., and Fundinger, R.: New Time-domain reflectometry sensors for water content determination in porous media, Sensors Update, 7, 301–316, doi: 10.1002/1616-8984(200001)7:1⟨301::AID-SEUP301⟩3.0.CO;2-X, 2001.

Stacheder, M., Huebner, C., Schlaeger, S., and Brandelik, A.: Combined TDR and low frequency permittivity measurements for continous snow density determination, chap. 16, pp. 367–382, Springer-Verlag Berlin, Heidelberg, New York, 2005.

Staehli, M., Stacheder, M., Gustafsson, D., Schlaeger, S., Schneebeli, M., and Brandelik, A.: A new in-situ sensor for large-scale snow cover monitoring, Annals of Glaciology, 38, 273–278, 2004.

Stephens, D. B.: Vadose zone hydrology, CRC Press, 1996.

Steppeler, J., Doms, G., Schuettler, U., Bitzer, H. W., Gassmann, A., Damrath, U., and Gregoric, G.: Meso-gamma scale forecasts using the nonhydrostatic model LM, Meteor. Atm. Phys, 82, 75–96, 2003.

Stummer, P., Maurer, H., and Green, A. G.: Experimental design: electrical resistivity data sets that provide optimum subsurface information, Geophysics, 69, 120–139, 2004.

Suzuki, K. and Higashi, S.: Groundwater flow after heavy rain in landside-slope area from 2D-inversion of resistivity monitoring data, Geophysics, 66, 733–743, 2001.

Teuling, A. J. and Troch, P. A.: Improved understanding of soil moisture variability dynamics, Geophysical Research Letters, 32, L05 404, doi:10.1029/2004GL021935, 2005.

Topp, G. C., Davis, J., and Annan, A. P.: Electromagnetic determination of soil water content. Measurements in coaxial transmission lines, Water Resources Research, 16, 574–582, 1980.

Trinks, I., Wachsmuth, D., and Stuempel, H.: Monitoring water flow in the unsaturated zone using georadar, First Break, 19, 679–684, 2001.

Turesson, A.: Water content and porosity estimated from ground-penetrating radar and resistivity, Journal of Applied Geophysics, 58, 99–111, doi:10.1016/j.jappgeo.2005.04.004, 2006.

Uginchus, A. A.: Seepage through earth dams, Israel Program for Scientific Translations, 1960.

Ulrich, C. and Slater, L. D.: Induced polarization measurements on unsaturated, unconsolidated sands, Geophysics, 69, 762–771, 2004.

van Genuchten, M. T.: A closed-form equation for predicting the hydraulic conductivity of unsaturated soils, Soil Science Society of America Journal, 44, 892–898, 1980.

Vanderborght, J., Kemna, A., Hardelauf, H., and Vereecken, H.: Potential of electrical resistivity tomography to infer aquifer transport characteristics from tracer studies: A synthetic case study, Water Resources Research, 41, W06 013, doi:10.1029/2004WR003774, 2005.

Vereecken, H., Kasteel, R., Vanderborght, J., and Harter, T.: Upscaling hydraulic properties and soil water flow processes in heterogeneous soils: a review, Vadose Zone Journal, 6, 1–28, 2007.

Vogel, H.-J. and Roth, K.: Moving through scales of flow and transport in soil, Journal of Hydrology, 272, 95–106, 2003.

Weihermueller, L., Huisman, J., Lambot, S., Herbst, M., and Vereecken, H.: Mapping the spatial variation of soil water content at the field scale with different ground penetrating radar techniques, Journal of Hydrology, 340, 205–216, 2007.

Weller, A., Canh, T., Breede, K., and Vu, N. T.: Multi-electrode measurements at Thai Binh dikes (Vietnam), Near Surface Geophysics, 4, 135–143, 2006.

Woersching, H., Becker, R., Schlaeger, S., and Bieberstein, A.: Feuchtemessung mit Spatial-TDR in großmaßstäblichen Modelldeichen aus Lehm, in: Innovative Feuchtemessung in Forschung und Praxis, vol. 2, pp. 215–221, 2006.

Wolke, R. and Schwetlick, H.: Iteratively reweighted least squares algorithms, covergence analysis and numerical comparisons, Statistical Computations, 9, 907–921, 1988.

Wollschlaeger, U. and Roth, K.: Estimation of temporal changes of volumetric soil water content from ground-penetrating radar reflections, Subsurface Sensing Technologies and Applications, 60, 207–218, doi:10.1007/s11220-005-0007-y, 2005.

Wulfmeyer, V., Behrendt, A., Bauer, H.-S., Kottmeier, C., Corsmeier, U., Blyth, A., Craig, G., Schumann, U., Hagen, M., Crewell, S., di Girolamo, P., Flamant, C., Miller, M., Montani, A., Mobbs, S., Richard, E., Rotach, M., Arpagaus, M., Russchenberg, H., Schluessel, P., Koenig, M., Gaertner, V., Steinacker, R., Dorninger, M., Turner, D., Weckwerth, T., Hense, A., and Simmer, C.: The Convective and Orographically-induced Precipitation Study: a research and development project of the world weather research program for improving quantitative precipitation forecasting in low-mountain regions, Bulletin of the American Meteorological Society, in press, 2008.

Zhou, B. and Dahlin, T.: Properties and effects of measurement errors on 2D resistivity imaging surveying, Near Surface Geophysics, 1, 105–117, 2003.

List of Figures

List of Tables

A Further Experiments

While the experiments on a full-scale dike model were the main experiments described in this study (see chapters 3 and 4), the first experiments that determined the viability of ERT to quantify water content were carried out on laboratory dikes (section A.1). The changes in water content determined by Spatial TDR were compared to changes in resistivity obtained by ERT. Two dikes built homogeneously of two different materials were monitored this way during flooding events.

The second section (A.2) shows additional results from the second experimental phase (see section 4.3.1) at the full-scale dike model at the Federal Waterways Engineering and Research Institute.

A.1 Laboratory Dikes

Two laboratory dikes in a laboratory hall at the University of Karlsruhe had been built up homogeneously with a dike base length of 8 m, a crest height of 1.4 m and a width of 2.2 m. Both were instrumented with twelve vertically installed Spatial TDR cables (section 2.4.2) 0.5 m apart. During several long flooding experiments, the infiltration processes and the water outflow on the landside slope were monitored as part of a project of the Institute for Rock Mechanics and Soil Mechanics (Woersching et al., 2006).

A.1.1 Laboratory Dike 1 - February 2005

The laboratory-scale model dike was built of a material with much lower hydraulic conductivity compared to the BAW full-scale dike model. Before ERT was installed, several experiments had already taken place, so that the dike had been wetted several times. For the experiment described here, an ERT line of 23 electrodes with a spacing of 0.2 m was installed down the landside slope. The

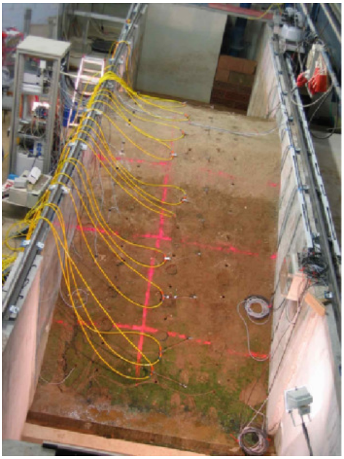

Figure A.1: *View from top on the laboratory-scale model dike with an ERT measuring installed over the length of the dike for a dry measurement.*

experiment comprised burdening the dike with a water level varying between 1.1 m and 1.3 m. The dike was monitored for three weeks, and ERT measurements were taken on five days. As Table A.1.1 shows, the outflow rate stayed constant throughout most of the experiment, so quasi-stationary flow conditions had established fast and no large differences in water content could be expected.

Results

By comparing changes in water content obtained from ERT and Spatial TDR (Fig. A.2), the viability of ERT to quantify water content was analyzed. The number of ERT measurements was not sufficient to estimate the saturation exponent as in chapter 3, so it was assumed to be 2. On the right hand side of Fig. A.2, the water content ratio is shown as measured with STDR, averaged onto the ERT model blocks. While ERT detects a strong increase in water content, Spatial TDR shows hardly any change within the dike, besides a strong

Date	Time	Water Outflow Rate[l/min]
10.02.	13:05	—
11.02.	11:25	0.54
14.02.	10:00	0.53
15.02.	09:45+10:45	0.56
16.02.	11:00	0.58
23.02.	10:30	0.45
01.03.	10:15	0.37

Table A.1: *Overview of measurements taken on laboratory dike 1.*

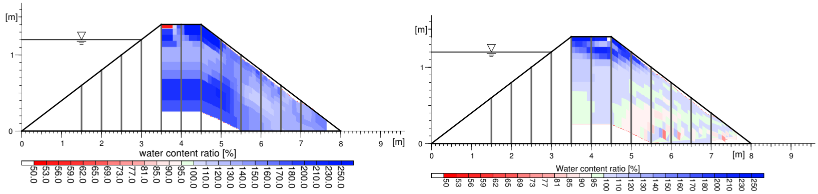

Figure A.2: *Water content ratio for laboratory dike 1, 23.02.2005: left: From ERT, right: From Spatial TDR*

increase in water content near the dike crest. As the water content was already rather high in the beginning, and only the crest was dry when the experiment started, this seems plausible. The dike was instrumented with several measurement techniques, so it seems likely that one of them, or the narrow width of the dike and its walls, may have disturbed the ERT measurement, creating an artifact in the low sensitivity regions of the tomogram. A high increase in water content near the crest is visible, but overall ERT and Spatial TDR do not agree well on this dike.

A.1.2 Laboratory Dike 2 - April 2005

The second dike was built next to the first dike (Fig. A.3). Compared with the first dike, it was built with a finer (loamer) material with an even lower hydraulic conductivity. In the flooding experiment described here, it took 16 days for the infiltrating water to reach the landside slope.

This was the first flooding of this particular dike, so the initial state was dry. However, the material used to build the dike might not have been completely dry because part of the material had been stored outside. In this experiment, the water level was raised to 0.5 m on April 2nd 2005, then raised to 1 m three days later. On April 18th, the first wetting became visible on the landside (Fig. A.3). Another four days later, water began to flow out of the slope, and the flooding experiment was ended, reaching a water level of 0 m on April 24th. As the dike was built in several equally thick layers, it became apparent that this may have created some preferred flow paths, as the first wetting on the landside slope was only present in two horizons. An overview of ERT measurements using Wenner-Schlumberger measurements is given by Table A.1.2.

Results

To obtain the change in water content, the saturation exponent was determined similar to chapter 3 ($n \approx 2.09$). The changes from 13th to the 15th and 18th can be seen in Fig. A.4. While the wetting has not yet reached the surface on the 15th, the measured change on the 18th shows the wetting on the landside as seen in Fig. A.3.

Figure A.5 compares results of the water content ratio between the 22nd and the 13th as measured with ERT and Spatial TDR. While there seems to be an artifact in the low sensitivity areas of the tomogram that is probably caused by heterogeneities in the dike or by influence from the walls or other measurement installations, the water content change near the slope and crest agree rather well for both methods. Both methods indicate a dry spot near the top of the slope, while an increase of 150% and more is retrieved near the foot of the slope. This demonstrates that ERT can be used for detecting water content change (Rings et al., 2005)

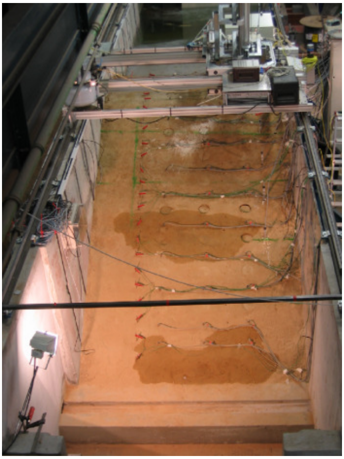

Figure A.3: *View from top on the laboratory-scale model dike 2, with beginning wetting of the landside slope.*

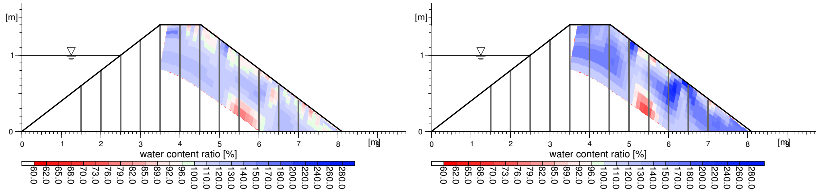

Figure A.4: *Water content ratio for laboratory dike 2: left: Interval 13th to 15th, right: Interval 13th to 18th*

A.2 Experiment BAW 2007

In April 2007, a second experiment was conducted on the full-scale model dike located at the Federal Waterways and Engineering Research Institute (BAW) in Karlsruhe. Over the course of two weeks, a long, intense rainfall was simulated and examined with ERT, GPR and Spatial TDR, with an additional flooding

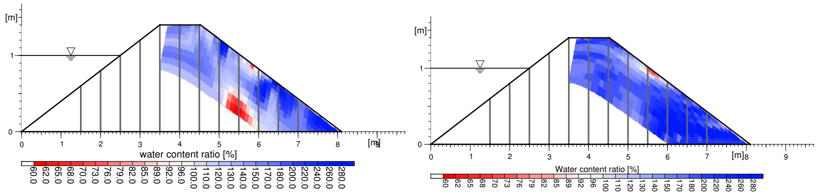

Figure A.5: *Water content ratio for laboratory dike 2, Interval 13th to 22th: left: From ERT, right: From Spatial TDR*

Date	Time
05.04.	09:20
11.04.	09:00
11.04.	11:30
13.04.	10:00+17:00
14.04.	10:30
15.04.	10:00
18.04.	15:45
19.04.	09:30+10:15+19:30
20.04.	09:30+19:30
21.04.	11:00+17:00
22.04.	11:00

Table A.2: *Overview of measurements taken on laboratory dike 2.*

experiment at the end of the two weeks. In addition to the results presented in section 4.3.1, a different electrode array was tested and measurement were taken with a vertically installed temperature chain.

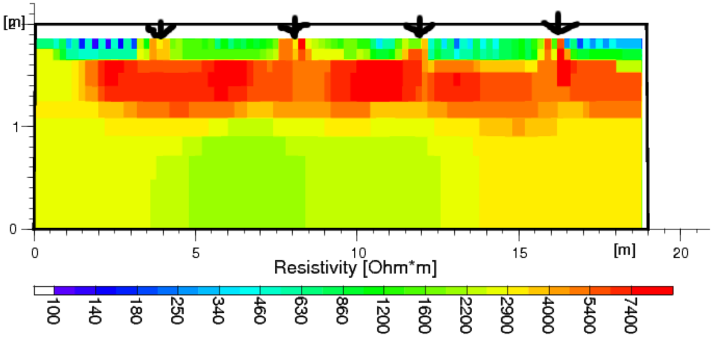

Figure A.6: *Measurement with Dipole-Dipole array along the dike crest on April 11th 2007. The stone pathways have been marked by arrows.*

A.2.1 Electrode array

The choice of the electrode array depends on the expected soil structure. A Wenner-Schlumberger was chosen for most measurements as a good compromise between measurement speed, resolution and signal-to-noise ratio. The Dipole-Dipole array was tested for some measurements, but although it should theoretically have a higher sensitivity, it was very sensitive to noise and disturbances, especially on the measurement line along the dike crest.

Stone paths (Fig. A.6) leading down the waterside 4 m apart had a grave influence on the Dipole-Dipole array measurement, creating large artifacts beneath the surface layer, which makes this array unsuitable for this dike. To ensure comparability, the Wenner-Schlumberger array was used for all measurements discussed in section 4.3.1.

A.2.2 Temperature Chain

A temperature measurement chain has been installed vertically into the dike, on the landside slope, near the crest. It consists of ten digital temperature elements built into a cable 30 cm apart from each other. The first element was just below the surface in the soil and the last element at 2.7 m depth near the dike base. A minilogger in a rain-proof casing automatically collected data and could be read out and programmed via an infrared interface.

Figure A.2.2 shows the temperature evolution at various depths. The upper panel shows the complete measurement series for the sensors at 0 m, 0.3 m, 0.9 m, 1.8 m and 2.7 m depth. The daily variations are clearly visible near the surface (0 m, red curve) but they are almost vanished at 0.3 m depth. During a phase of strong sprinkling from April 12th to 16th, the daily variations in the dike reached greater depths, and are noticeable up to a depth of 1.8 m. Also, the mean temperature at greater depth (but not near the base), increases due to the water.

The flooding event in the lower panel is shown with higher temporal resolution for the sensors at greater depth. The start of the flooding on April 20th 2007 at 17:00 becomes visible at the deepest sensor almost immediately. The water level was raised until 20:00, then again on the 21st starting at 09:40. Whenever infiltrating water reaches a sensor, it is clearly visible through a corresponding decrease in temperature. A measurement of water temperature in the flooding basin near the surface showed a water temperature of 13.6 $^\circ C$ at 11:00 on April 21st and of 16.3 $^\circ C$ at 13:30 April 22nd. It can be assumed that incoming radiation, supported by the black layer underneath the dike and basin, heated the water. However, the decrease in temperature to below 12 $^\circ C$ at the lowest sensor leads to the assumption that the infiltrating water initially had a lower temperature. After the dike was flooded, the larger heat conductivity of the water saturated soil allowed increasing temperatures throughout the dike. Even after the water level was decreased again, the temperature has increased by 2 $^\circ C$ at the lowest sensor.

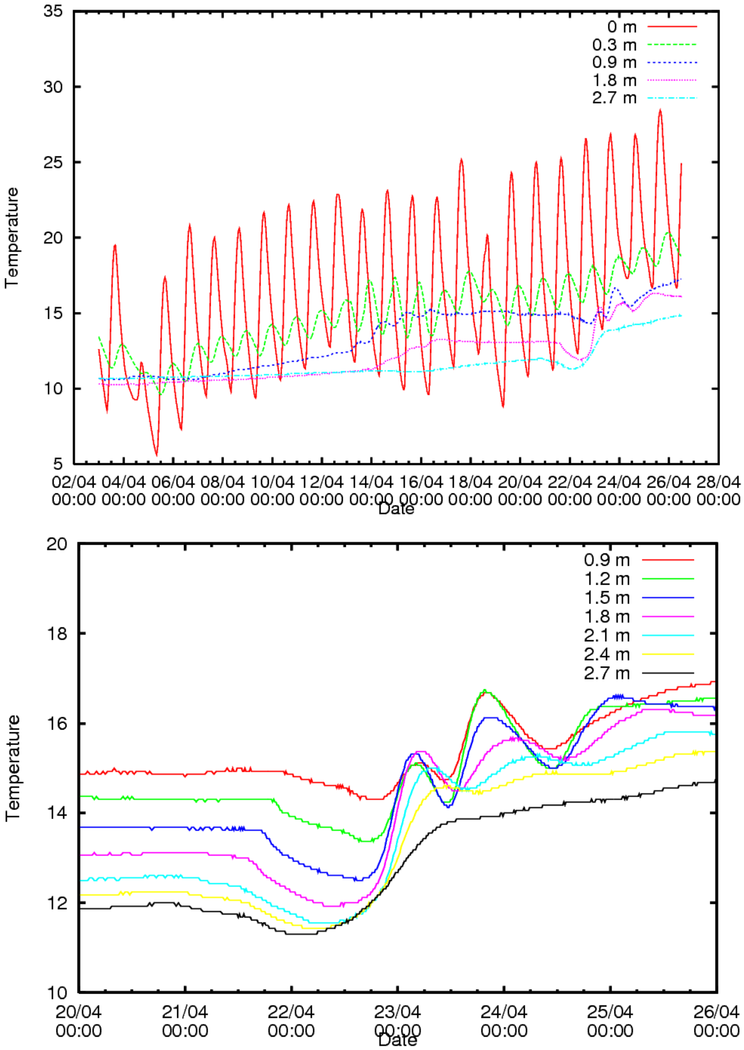

Figure A.7: *Soil temperature for (a) Upper: the experiment BAW 2007 and (b) Lower: only the flooding for various temperature sensors on a measurement chain installed vertically into the dike near the crest.*

Acknowledgments

I thank the Deutsche Forschungsgemeinschaft for supporting my project in the Research Training Group Natural Disasters and the editors and reviewers of the Journal articles for their valuable input.
I thank my advisor Prof. Christoph Kottmeier, for his supervision and encouragment.
I thank my second reviewer Prof. Kurt Roth for his continued support and advice.
I thank Dr.-Ing. Andreas Bieberstein, Dr.-Ing. Alexander Scheuermann and Holger Wörsching for supporting this project and for providing access to the dike facilities. I also thank the BAW for being able to experiment on the model dike.
I thank Dr. Christian Hauck for great amounts of help, advice and support.
I thank all the people in the Institute for Meteorology and Climate Research, the co-authors of the papers, the Research Training Group Natural Disasters, the Soil Moisture Group, who all contributed to this work. To name only a few, I especially thank Mathias Bach, Norbert Kalthoff, Martin Kohler, Franz Königer, Liane Krauß, Michael Kunz, Kwasi Preko, Rainer Schuhmann and Markus Stacheder.
I thank Sander Huisman for reading and improving the manuscript.
If you are reading these acknowledgments, there is a pretty good chance you have contributed to this thesis. So, in case you are not listed, be sure to know I thank you.
Most importantly, I thank my family and friends, especially my father and most of all, Mana.

Wissenschaftliche Berichte des Instituts für Meteorologie und Klimforschung der Universität Karlsruhe

Bisher erschienen:

Nr. 1: Fiedler,F., Prenosil, T.:
Das MESOKLIP-Experiment.
(Mesoskaliges Klimaprogramm im Oberrheintal).
August 1980

Nr. 2: Tangermann-Dlugi, G.:
Numerische Simulationen atmosphärischer Grenzschichtströmungen über langgestreckten mesoskaligen Hügelketten bei neutraler thermischer Schichtung.
August 1982

Nr. 3: Witte, N.:
Ein numerisches Modell des Wärmehaushalts fließender Gewässer unter Berücksichtigung thermischer Eingriffe.
Dezember 1982

Nr. 4: Fiedler, F. und Höschele, K. (Hrsg.):
Prof. Dr. Max Diem zum 70. Geburtstag.
Februar 1983 (vergriffen)

Nr. 5: Adrian, G.:
Ein Initialisierungsverfahren für numerische mesoskalige Strömungsmodelle.
Juli 1985

Nr. 6: Dorwarth, G.:
Numerische Berechnung des Druckwiderstandes typischer Geländeformen.
Januar 1986

Nr. 7: Vogel, B., Adrian, G., Fiedler, F.:
MESOKLIP-Analysen der meteorologischen Beobachtungen von mesoskaligen Phänomenen im Oberrheingraben.
November 1987

Nr. 8: Hugelmann, C.-P.:
Differenzenverfahren zur Behandlung der Advektion.
Februar 1988

Nr. 9: Hafner, T.:
Experimentelle Untersuchungen zum Druckwiderstand der Alpen.
April 1988

Nr. 10: Corsmeier, U.:
Analyse turbulenter Bewegungsvorgänge in der maritimen atmosphärischen Grenzschicht.
Mai 1988

Nr. 11: Walk, O. and Wieringa, J.(eds):
Tsumeb Studies of the Tropical Boundary-Layer Climate.
Juli 1988

Nr. 12: Degrazia, G. A.:
Anwendung von Ähnlichkeitsverfahren auf die turbulente Diffusion in der konvektiven und stabilen Grenzschicht.
Januar 1989

Nr. 13: Schädler, G.:
Numerische Simulationen zur Wechselwirkung zwischen Landoberflächen und atmophärischer Grenzschicht.
November 1990

Nr. 14: Heldt, K.:
Untersuchungen zur Überströmung eines mikroskaligen Hindernisses in der Atmosphäre.
Juli 1991

Nr. 15: Vogel, H.:
Verteilungen reaktiver Luftbeimengungen im Lee einer Stadt -
Numerische Untersuchungen der relevanten Prozesse.
Juli 1991

Nr. 16: Höschele, K.(ed.):
Planning Applications of Urban and Building Climatology -
Proceedings of the IFHP / CIB-Symposium Berlin, October 14 - 15, 1991.
März 1992

Nr. 17: Frank, H.P.:
Grenzschichtstruktur in Fronten.
März 1992

Nr. 18: Müller, A.:
Parallelisierung numerischer Verfahren zur Beschreibung von Ausbreitungs- und chemischen Umwandlungsprozessen in der atmosphärischen Grenzschicht.
Februar 1996

Nr. 19: Lenz, C.-J.:
Energieumsetzungen an der Erdoberfläche in gegliedertem Gelände.
Juni 1996

Nr. 20: Schwartz, A.:
Numerische Simulationen zur Massenbilanz chemisch reaktiver Substanzen im mesoskaligen Bereich.
November 1996

Nr. 21: Beheng, K.D.:
Professor Dr. Franz Fiedler zum 60. Geburtstag.
Januar 1998

Nr. 22: Niemann, V.:
Numerische Simulation turbulenter Scherströmungen mit einem Kaskadenmodell.
April 1998

Nr. 23: Koßmann, M.:
Einfluß orographisch induzierter Transportprozesse auf die Struktur der atmosphärischen Grenzschicht und die Verteilung von Spurengasen.
April 1998

Nr. 24: Baldauf, M.:
Die effektive Rauhigkeit über komplexem Gelände - Ein Störungstheoretischer Ansatz.
Juni 1998

Nr. 25: Noppel, H.:
Untersuchung des vertikalen Wärmetransports durch die Hangwindzirkulation auf regionaler Skala.
Dezember 1999

Nr. 26: Kuntze, K.:
Vertikaler Austausch und chemische Umwandlung von Spurenstoffen über topographisch gegliedertem Gelände.
Oktober 2001

Nr. 27: Wilms-Grabe, W.:
Vierdimensionale Datenassimilation als Methode zur Kopplung zweier verschiedenskaliger meteorologischer Modellsysteme.
Oktober 2001

Nr. 28: Grabe, F.:
Simulation der Wechselwirkung zwischen Atmosphäre, Vegetation und Erdoberfläche bei Verwendung unterschiedlicher Parametrisierungsansätze.
Januar 2002

Nr. 29: Riemer, N.:
Numerische Simulationen zur Wirkung des Aerosols auf die troposphärische Chemie und die Sichtweite.
Mai 2002

Nr. 30: Braun, F. J.:
Mesoskalige Modellierung der Bodenhydrologie.
Dezember 2002

Nr. 31: Kunz, M.:
Simulation von Starkniederschlägen mit langer Andauer über Mittelgebirgen.
März 2003

Nr. 32: Bäumer, D.:
Transport und chemische Umwandlung von Luftschadstoffen im Nahbereich von Autobahnen - numerische Simulationen.
Juni 2003

Nr. 33: Barthlott, C.:
Kohärente Wirbelstrukturen in der atmosphärischen Grenzschicht.
Juni 2003

Nr. 34: Wieser, A.:
Messung turbulenter Spurengasflüsse vom Flugzeug aus.
Januar 2005

Nr. 35: Blahak, U.:
Analyse des Extinktionseffektes bei Niederschlagsmessungen mit einem C-Band Radar anhand von Simulation und Messung.
Februar 2005

Nr. 36: Bertram, I.:
Bestimmung der Wasser- und Eismasse hochreichender konvektiver Wolken anhand von Radardaten, Modellergebnissen und konzeptioneller Betrachtungen.
Mai 2005

Nr. 37: Schmoeckel, J.:
Orographischer Einfluss auf die Strömung abgeleitet aus Sturmschäden im Schwarzwald während des Orkans „Lothar“.
Mai 2006

Nr. 38: Schmitt, C.:
Interannual Variability in Antarctic Sea Ice Motion.
Interannuelle Variabilität antarktischer Meereis-Drift.
Mai 2006

Nr. 39: Hasel, M.:
Strukturmerkmale und Modelldarstellung der Konvektion über Mittelgebirgen
Juli 2006

Ab Band 40 erscheinen die Wissenschaftlichen Berichte des Instituts für Meteorologie und Klimaforschung im Universitätsverlag Karlsruhe online unter der Internetadresse: http://www.uvka.de/
Auf Wunsch sind beim Universitätsverlag Karlsruhe auch gedruckte Exemplare erhältlich („print on demand“).

Nr. 40: Lux, R.:
Modellsimulationen zur Strömungsverstärkung von orographischen Grundstrukturen bei Sturmsituationen.
Mai 2007

Nr. 41: Straub, W.:
Der Einfluss von Gebirgswellen auf die Initiierung und Entwicklung konvektiver Wolken.
März 2008

Nr. 42: Meißner, C.:
High-resolution sensitivity studies with the regional climate model COSMO-CLM.
Dezember 2008

Nr. 43: Höpfner, M.:
Charakterisierung polarer stratosphärischer Wolken mittels hochauflösender Infrarotspektroskopie.
Oktober 2008

Nr. 44: Rings, J.:
Monitoring the water content evolution of dikes.
Januar 2009

ISSN: 0179-5619
ISBN: 978-3-86644-321-1

www.uvka.de